



Technical Report HL-96-16
June 1996

A Two-Dimensional Free-Surface Flow Model for Trapezoidal High-Velocity Channels

by *Richard L. Stockstill*

Approved For Public Release; Distribution Is Unlimited

DTIC QUALITY INSPECTED 3

19960723 031

Prepared for Headquarters, U.S. Army Corps of Engineers

The contents of this report are not to be used for advertising, publication, or promotional purposes. Citation of trade names does not constitute an official endorsement or approval of the use of such commercial products.



PRINTED ON RECYCLED PAPER

A Two-Dimensional Free-Surface Flow Model for Trapezoidal High-Velocity Channels

by Richard L. Stockstill

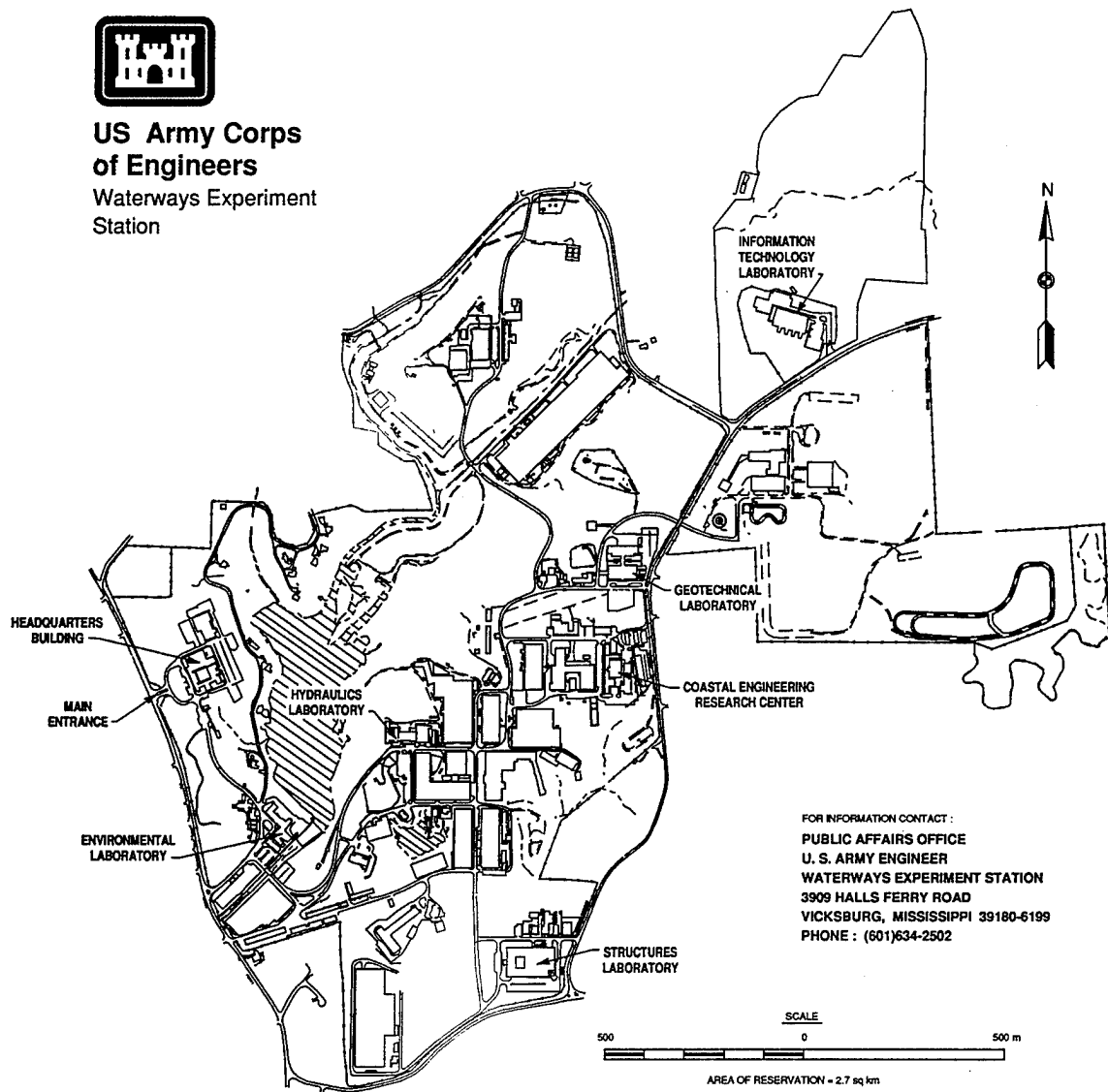
U.S. Army Corps of Engineers
Waterways Experiment Station
3909 Halls Ferry Road
Vicksburg, MS 39180-6199

Final report

Approved for public release; distribution is unlimited



**US Army Corps
of Engineers**
Waterways Experiment
Station



Waterways Experiment Station Cataloging-in-Publication Data

Stockstill, Richard L.

A two-dimensional free-surface flow model for trapezoidal high-velocity channels / by Richard L. Stockstill ; prepared for U.S. Army Corps of Engineers.

198 p. : ill. ; 28 cm. -- (Technical report ; HL-96-16)

Includes bibliographical references.

1. Channels (Hydraulic engineering) -- Design and construction -- Mathematical models.
2. Flood control channels -- Mathematical models. I. United States. Army. Corps of Engineers. II. U.S. Army Engineer Waterways Experiment Station. III. Hydraulics Laboratory (U.S. Army Engineer Waterways Experiment Station) IV. Title. V. Series: Technical report (U.S. Army Engineer Waterways Experiment Station) ; HL-96-16. TA7 W34 no.HL-96-16

TABLE OF CONTENTS

LIST OF FIGURES	vi
LIST OF TABLES	ix
NOTATION	x
PREFACE	xv
CHAPTER 1: INTRODUCTION	1
Background	1
Hydraulic Design of High-Velocity Channels	4
One-Dimensional Analysis	8
Two-Dimensional Analysis	9
Objectives	12
Outline of Dissertation	14
CHAPTER 2: PREVIOUS RESEARCH	15
Moving Boundary Flow Problems	15
Laterally-Averaged Models	16
Depth-Averaged Models	17
Wetting and Drying Method	18
Transformation Method	19
Moving Finite Element Method	21
CHAPTER 3: EQUATIONS FOR MOVING BOUNDARY FLOW	26
Shallow Water Equations	26
Moving Reference Frame Effects	31
CHAPTER 4: FINITE ELEMENT MODEL	36
Finite Element Formulation	37
Petrov-Galerkin Test Function	48
Temporal Derivatives	53
Boundary Conditions	53
Open Boundaries	54
Side Boundaries	54
Movement of Interior Nodes	59

Initial Conditions	61
Solution Procedure	62
CHAPTER 5: MODEL VALIDATION	68
Analytic Equations	68
Test Conditions	70
Test Results	73
CHAPTER 6: MODEL TESTING	78
Trapezoidal-to-Rectangular Transition	80
Test Conditions	82
Test Results	90
Parameter Sensitivity Tests	99
Test 1: Manning's n Value	100
Test 2: Turbulent Kinematic Viscosity Coefficient	102
Test 3: Flow Depth at the Moving Boundary	102
Trapezoidal Channel with a Horizontal Curve	106
Test Conditions	110
Test Results	116
Rectangular-to-Trapezoidal Transition	122
Test Conditions	122
Test Results	130
Multiple Flow Obstructions	140
Test Conditions	140
Test Results	146
Discussion of Model Results	155
CHAPTER 7: SUMMARY AND CONCLUSIONS	158
Summary	158
Conclusions	159
Recommendations for Additional Research	161
BIBLIOGRAPHY	163

APPENDIX A: NEWTON-RAPHSON JACOBIAN TERMS

FOR MOVING FINITE ELEMENTS 171

SF 298

LIST OF FIGURES

<i>Number</i>	<i>Page</i>
1.1 Flow conditions in the Rio Hondo River, California	2
1.2 Schematic plan views of standing wave patterns in supercritical flow	5
1.3 Cross-sections showing superelevation in a channel bend	6
2.1 Half section sketch showing imaginary fixed vertical barrier	18
3.1 Flow variables	27
4.1 Definition sketch of the direction of allowable nodal movement, $\hat{\theta}$	42
4.2 Transformation from global coordinates to local coordinates	43
4.3 Schematic of element folding from excessive nodal displacement	60
5.1 V-shaped channel boundary and initial conditions	72
5.2 Numerical model computational mesh for V-shaped channel	74
5.3 Analytical and model computed flow depths for V-shaped channel	75
5.4 Analytical and model computed longitudinal velocity for V-shaped channel	75
6.1 Plan and elevation view of tilting flume	80
6.2 Plan view and sections of trapezoidal-to-rectangular transition	82
6.3 Dry bed view of trapezoidal-to-rectangular transition	83
6.4 Flow conditions in trapezoidal-to-rectangular transition	84
6.5 Numerical model computational meshes for trapezoidal-to-rectangular transition	86
6.6 Time history of depth for trapezoidal-to-rectangular transition at centerline of sta 50	91
6.7 Definition sketch of depths plotted on depth contours	91
6.8 Depth contours for trapezoidal-to-rectangular transition	93
6.9 Computed water-surface mesh for trapezoidal-to-rectangular transition	94
6.10 Water-surface profiles for trapezoidal-to-rectangular transition, $n = 0.009$, $C_b = 0.1$, $\hat{h} = 0.01$ ft	95

6.11	Plan view schematic of actual and shallow water model standing wave patterns	96
6.12	Computed and observed wavelengths for trapezoidal-to-rectangular transition	97
6.13	Computed and observed depth-averaged longitudinal velocities for trapezoidal-to-rectangular transition	99
6.14	Water-surface profiles for trapezoidal-to-rectangular transition, $n = 0.010$, $C_b = 0.1$, $\hat{h} = 0.01$ ft	101
6.15	Water-surface profiles for trapezoidal-to-rectangular transition, $n = 0.009$, $C_b = 1.0$, $\hat{h} = 0.01$ ft	103
6.16	Water-surface profiles for trapezoidal-to-rectangular transition, $n = 0.009$, $C_b = 0.1$, $\hat{h} = 0.005$ ft	105
6.17	Plan view and sections of trapezoidal horizontal curve	107
6.18	Dry bed view of trapezoidal horizontal curve	108
6.19	Flow conditions in trapezoidal horizontal curve	111
6.20	Numerical model computational meshes for trapezoidal horizontal curve	113
6.21	Computed and observed side boundaries for trapezoidal horizontal curve	117
6.22	Depth contours for trapezoidal horizontal curve	118
6.23	Cross section view of flow depth for trapezoidal horizontal curve	119
6.24	Computed and observed depth-averaged velocities for trapezoidal horizontal curve	121
6.25	Plan view and sections of rectangular-to-trapezoidal transition	123
6.26	Dry bed view of rectangular-to-trapezoidal transition	124
6.27	Flow conditions in rectangular-to-trapezoidal transition	125
6.28	Numerical model computational meshes for rectangular-to-trapezoidal transition	127
6.29	Depth contours for rectangular-to-trapezoidal transition	131

6.30	Computed water-surface mesh	
	for rectangular-to-trapezoidal transition	132
6.31	Computed and observed side boundaries	
	for rectangular-to-trapezoidal transition	133
6.32	Water-surface profiles for rectangular-to-trapezoidal transition	134
6.33	Schematic of flow and geometric variables	137
6.34	Computed and observed depth-averaged velocities	
	for rectangular-to-trapezoidal transition	139
6.35	Plan view of multiple flow obstructions in the trapezoidal channel	141
6.36	Dry bed view of trapezoidal channel with flow obstructions	142
6.37	Numerical model computational meshes for trapezoidal channel	
	with flow obstructions	143
6.38	Flow conditions in trapezoidal channel with flow obstructions	147
6.39	Depth contours for trapezoidal channel with flow obstructions	148
6.40	Water-surface profiles	
	for trapezoidal channel with flow obstructions	150
6.41	Computed and observed side boundaries	
	for trapezoidal channel with flow obstructions	151
6.42	Computed water-surface mesh	
	for trapezoidal channel with flow obstructions	152
6.43	Computed and observed depth-averaged velocities	
	for trapezoidal channel with flow obstructions	154

LIST OF TABLES

<i>Number</i>	<i>Page</i>
4.1 Number of boundary conditions required	55
5.1 V-shaped channel, model parameters	73
5.2 V-shaped channel, analytical and model computed specific energy	76
6.1 Trapezoidal-to-rectangular transition, boundary conditions	87
6.2 Trapezoidal-to-rectangular transition, model parameters	88
6.3 Curved channel, trapezoidal cross section, boundary conditions	115
6.4 Curved channel, trapezoidal cross section, model parameters	115
6.5 Rectangular-to-trapezoidal transition, boundary conditions	128
6.6 Rectangular-to-trapezoidal transition, model parameters	129
6.7 Multiple flow obstructions, boundary conditions	145
6.8 Multiple flow obstructions, model parameters	145

NOTATION

A^*	Jacobian of F_x^*
\hat{A}	characteristic matrix
B^*	Jacobian of F_y^*
\hat{B}	characteristic matrix
C	Chezy coefficient
Cr	Courant number
C_0	dimensional constant, $C_0 = Cn/h^{1/6}$
C_1	constant
C_2	constant
C_b	coefficient that varies between 0.1 and 1.0
c	gravity wave celerity, $c = (gh)^{1/2}$
c_R	actual wave celerity, $c_R = (gL_w/2\pi \tanh(2\pi h/L_w))^{1/2}$
D_{50}	grain size of which 50 percent of the sample is finer
D_{90}	grain size of which 90 percent of the sample is finer
D_{100}	grain size of which 100 percent of the sample is finer
d	flow depth measured perpendicular to the channel bed
E	specific energy
Fr	cross-sectional average Froude number
Fr_ℓ	local Froude number
F_x	vector of fluxes in the x direction
F_x^*	x-direction vector of fluxes relative to a moving coordinate system
F_y	vector of fluxes in the y direction
F_y^*	y-direction vector of fluxes relative to a moving coordinate system
f	Darcy-Weisbach friction factor
G	product of node velocity gradient and flow variable vector
g	acceleration due to gravity
H	vector of source terms
h	flow depth
h_{eff}	effective depth

\hat{h}	flow depth at a moving boundary
\mathbf{I}	identity matrix
L	differential equation operator
L_w	wave length
\mathbf{L}	vector of unknowns, $\mathbf{L} = (h, p, q)^T$ for interior nodes $\mathbf{L} = (s, p, q)^T$ for moving boundary nodes
ℓ	element mesh parameter, grid spacing
ℓ_{\min}	minimum grid spacing
n	Manning's roughness coefficient
n_x	x-direction component of $\hat{\mathbf{n}}$
n_y	y-direction component of $\hat{\mathbf{n}}$
$\hat{\mathbf{n}}$	unit vector outward normal to the boundary, $\hat{\mathbf{n}} = (n_x, n_y)$
P	pressure
\mathbf{P}	right eigenvector of \mathbf{A}
\mathbf{P}^{-1}	left eigenvector of \mathbf{A}^*
p	volumetric discharge per unit width in the x direction, $p = uh$
p'	volumetric discharge per unit width in the x' direction, $p' = u'd$
p^*	volumetric discharge per unit width in the x direction relative to a moving coordinate system
\mathbf{Q}	vector of flow variables, $\mathbf{Q} = (h, p, q)^T$
q	volumetric discharge per unit width in the y direction, $q = vh$
q^*	volumetric discharge per unit width in the y direction relative to a moving coordinate system
\mathbf{R}	solution vector of a system of nonlinear equations
Re	Reynolds number
Re_ℓ	mesh Reynolds number
r	radial distance in cylindrical coordinates
\mathbf{s}	node displacement vector, $\mathbf{s} = s \hat{\theta}$
$ s $	magnitude of the displacement vector

\mathbf{T}	right eigenvector of \mathbf{B}^*
\mathbf{T}^{-1}	left eigenvector of \mathbf{B}^*
t	time
U	a general function
u	x-direction component of depth-averaged velocity
u'	depth-averaged velocity in the x' direction
u_g	x-direction component of node velocity
u_r	x-direction component of reference frame velocity or radial component of velocity in cylindrical coordinates
u_z	vertical component of velocity
u_0	constant advection speed
u_ω	ω -direction component of velocity in cylindrical coordinates
v	y-direction component of depth-averaged velocity
\bar{V}	cross-sectional averaged velocity
\mathbf{V}^e	elemental velocity
\mathbf{V}_g	node velocity, $\mathbf{V}_g = (u_g, v_g)$
\mathbf{V}_r	reference frame velocity, $\mathbf{V}_r = (u_r, v_r)$
v_g	y-direction component of node velocity
v_r	y-direction component of reference frame velocity
W_i	weighting functions
\mathbf{X}	spatial coordinates of a fixed reference frame
x	spatial coordinate
x'	spatial coordinate parallel to the bed
y	spatial coordinate, orthogonal to x
z	vertical spatial coordinate
z_b	channel invert elevation relative to channel center line invert elevation
z_s	water surface elevation relative to datum
z_0	channel invert elevation relative to datum
α	temporal differencing coefficient

β	Petrov-Galerkin weighting coefficient
Γ	area boundary
γ	eigenvalue or characteristic
$\Delta \mathbf{L}$	solution of a linear system of equations
Δx	x-direction element dimension
Δy	y-direction element dimension
Δt	time step
δ_R	actual angle of standing wave
δ_{SW}	angle of standing wave given by shallow water equations
η	local spatial coordinate, orthogonal to ξ
$\hat{\theta}$	unit vector in the direction of allowable nodal movement
θ_x	x-direction component of $\hat{\theta}$
θ_y	y-direction component of $\hat{\theta}$
Λ_x	matrix of eigenvalues of \mathbf{A}^*
Λ_y	matrix of eigenvalues of \mathbf{B}^*
λ	eigenvalue or characteristic
ν	molecular kinematic viscosity
ν_t	turbulent kinematic viscosity
ξ	local spatial coordinate, orthogonal to η
Σ	summation operator
σ_{xx}	x-direction Reynolds stress per unit area acting on the face normal to the x axis
σ_{xy}	x-direction Reynolds stress per unit area acting on the face normal to the y axis
σ_{yx}	y-direction Reynolds stress per unit area acting on the face normal to the x axis
σ_{yy}	y-direction Reynolds stress per unit area acting on the face normal to the y axis
τ	time in a moving coordinate system
ϕ_i	Galerkin part of the test functions
ϕ_j	finite element basis functions
χ	spatial coordinates which move relative to a fixed reference frame

Ψ	test function
Ψ_i	Petrov-Galerkin test functions
Ω	spatial domain
ω	angular direction in cylindrical coordinates
ρ	fluid density
ϕ_i	non-Galerkin part of the test functions
ζ	angle of channel slope relative to horizontal
O	order of
\sim	indicates discrete value of the quantity
∇	gradient operator
∂	partial derivative operator
f	nonhomogeneous component of a partial differential equation
\int	area integral operator
\oint	line integral operator

Superscripts

k	Newton-Raphson iteration number
m	time step number
T	transpose of a matrix or a vector
-1	inverse of a matrix

Subscripts

i	weight function or test function identification number
j	node identification number
R	denotes quantity in the real system

PREFACE

This report is a product of research conducted from 1990 to 1995 by Dr. Richard L. Stockstill of the Spillways and Channels Branch (SCB), Hydraulic Structures Division (HSD), Hydraulics Laboratory (HL), U.S. Army Engineer Waterways Experiment Station (WES). The research was conducted under the general supervision of Mr. R. A. Sager, Acting Director, HL; Mr. R. F. Athow, Acting Assistant Director, HL; Dr. P. G. Combs, Chief, HSD; and Mr. B. P. Fletcher, Chief, SCB.

This report is a dissertation in partial fulfillment of the requirements for the degree of Doctor of Philosophy from the University of Washington (UW), Seattle.

Several people were involved in the research documented in this report. The author is thankful to Prof. Ronald E. Nece, for passing on part of the vast knowledge he has acquired through his forty plus years of experience in applying the principles of hydrodynamics to the solution of hydraulic engineering problems. Appreciation is also extended to the Reading Committee members, Profs. Stephen J. Burges and Harry H. Yeh. These gentlemen, all of the Department of Civil Engineering, UW, provided a thorough review of this dissertation in a timely manner. Their comments and suggestions significantly improved this document. Finally, recognition is given to Dr. R. C. (Charlie) Berger, Waterways and Estuaries Division, HL, and Affiliate Professor, UW, for teaching the author the finite element method and the process of systematic construction of a numerical model.

At the time of publication of this report, Director of WES was Dr. Robert W. Whalin. Commander was COL Bruce K. Howard, EN.

The contents of this report are not to be used for advertising, publication, or promotional purposes. Citation of trade names does not constitute an official endorsement or approval for the use of such commercial products.

CHAPTER 1

INTRODUCTION

Background

The growth of many cities in the United States has resulted in urban development in many natural floodplains. This development often increases runoff from rainfall which in turn increases river flow rates. These increased volumetric flow rates have resulted in floods which have caused millions of dollars in property damages and loss of life.

Engineers are often asked to propose methods to reduce flood damages and prevent loss of life on developed floodplains. Construction of flood control channels is a popular method to increase the capacity of the natural channel and reduce flooding. These channels are typically concrete lined or constructed as composite channels with the invert concrete and the side slopes grouted stone. If the natural topographic relief is sufficient, these lined channels usually are designed with hydraulically steep slopes to convey supercritical flow over most of the improved reach. Froude numbers in these man-made channels commonly range from 1.2 to 2.0.

Hydraulic engineers many times use the term "high-velocity channels" when referring to a lined flood control channel designed to discharge supercritical flow. The designer of these high-velocity channels in developed areas is faced with many questions which are not easily answered. The main concern is the depth of flow in the channel for the design discharge. The depth must be known to determine sidewall heights and minimum bridge soffit elevations. Determining the depth of flow is complicated by side inflows and boundary features such as contractions, expansions,

curves, and obstructions to the flow such as bridge piers, and vehicle access ramps. These boundary features in a supercritical channel cause flow disturbances which can result in a significant increase in the local flow depth. Figure 1.1 shows the flow conditions in a high-velocity channel. The oblique standing waves in the foreground are generated at the tails of piers located just upstream of the reach shown in the photograph. An accurate prediction of the water surface shape (i.e. variations in local depth) is essential in the successful design of a high-velocity channel.



Figure 1.1. Flow conditions in Rio Hondo River, California (looking downstream).

The cross sectional shape of high-velocity channels is generally either rectangular or trapezoidal, the choice of which is dictated by optimization of hydraulic and economic concerns. The economic tradeoff of rectangular versus trapezoidal channels is that rectangular channels require less real estate; however, construction of rectangular channels is more costly than trapezoidal channels. The structural cost of vertical sidewalls is often greater than the cost of acquiring the additional real estate required to convey the flood flow in a trapezoidal channel. Trapezoidal channels can be constructed by using levees on both sides of the channel and then paving the channel side slopes and invert. Channel cross section shapes are selected based on adequate hydraulic capacity in conjunction with the minimum cost of construction and maintenance. The total cost includes costs of right of way, the cost of construction and modification of structures such as bridges, and maintenance costs associated with the removal of sediment and/or debris.

The flow in trapezoidal high-velocity channels differs markedly from flow in rectangular channels. Straight reaches of rectangular channels produce a fairly uniform distribution of velocity at a cross section, although the actual distribution is influenced by the channel boundary and free surface drag and therefore depends on the channel's width-to-depth aspect ratio (Rouse 1961). However, the velocity variations across a section of straight trapezoidal channel are large. Flow along the side slopes near the water's edge is severely retarded by bed drag as the flow depth decreases. The local Froude number near the side boundary approaches zero. The local flow regime at a cross section of a trapezoidal high-velocity channel can be supercritical at

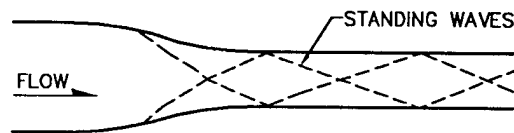
the center and subcritical near the water's edge. The flow over a portion of the side slope may be at or near critical. This mixture of subcritical and supercritical flow regimes can lead to flow instabilities and associated fluctuations in depth and velocity.

Hydraulic Design of High-Velocity Channels

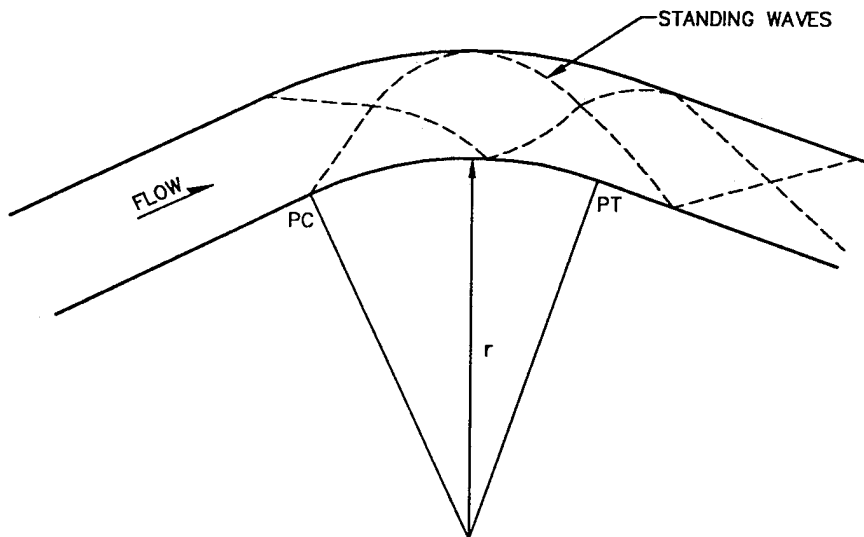
Supercritical flow in channels is characterized by standing waves created by even small changes in the sidewall alignment (figure 1.2a). Oblique standing waves are created at the beginning of channel bends (PC, figure 1.2b) where the depth along the outer wall increases as the wall exerts a force on the fluid. This depth increase is also realized at the beginning of a channel contraction. The flow along the inside wall at the point of curvature, PC, responds as at a channel expansion resulting in a depth reduction. However, away from the walls the flow remains unchanged until the forces generated at the boundaries are present in the form of pressure differences. The standing wave pattern downstream of the initial wave intersection point is not a straight line, because the flow at this point is moving along a curved path. Reflections of these waves continue over long distances downstream of the curve. The water surface setup or superelevation in rectangular channel bends (figure 1.3a) is significantly greater in supercritical flow than in subcritical flow and the superelevation in trapezoidal channels results in runup on the side slope at the outside of the bend and drawdown on the inside side slope (figure 1.3b).

Before the classic papers composing the 1951 symposium on high-velocity flow were published by the American Society of Civil Engineers (Ippen 1951, Knapp 1951, Ippen and Dawson 1951, and Rouse et al. 1951) each component of a

supercritical channel design was tested in a physical hydraulic model. The symposium papers provided fundamental descriptions of the mechanics of supercritical flow in man-made channels. These descriptions provided design guidance for engineers who designed high-velocity channels.

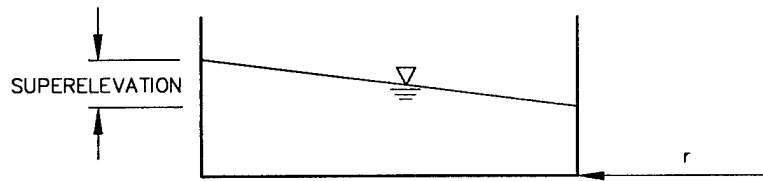


a. Rectangular channel contraction

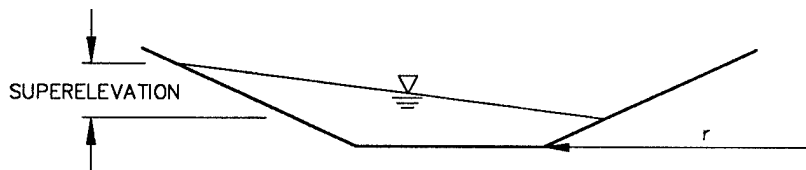


b. Rectangular channel bend

Figure 1.2. Schematic plan views of standing wave patterns in supercritical flow.



a. Rectangular channel



b. Trapezoidal channel

Figure 1.3. Cross-sections showing superelevation in a channel bend (r is the inside bend radius).

Ippen (1951) details the treatment of oblique standing waves for supercritical flow at small changes in the vertical sidewall boundary alignment. Ippen gives the oblique wave angle and the resulting wave height. Water surface disturbances are analyzed by either assuming constant specific energy or by considering the energy loss across the disturbance. The first assumption is appropriate for gradual water surface changes while analyses of large standing wave fronts must consider energy losses. In his analysis Ippen makes the assumptions that the flow is steady, the pressure distribution is hydrostatic, the velocity does not vary in the vertical, and the channel is frictionless or that the friction slope is parallel to the channel slope.

Ippen and Dawson (1951) demonstrate the applicability of the findings of Ippen (1951) to design problems of channel contractions. This is accomplished by comparing analytical solutions to laboratory data. These comparisons reveal that phase errors exist between the theoretical and observed depth profiles along a contraction. The theoretical waves are located upstream of the observed waves. Ippen and Dawson attribute this discrepancy to the hydrostatic pressure distribution assumption used in the analytical model. However, they note that the analytical solution is generally adequate for channel design purposes. They also provide design guidance for ways to reduce waves downstream of a contraction.

Knapp (1951) gives a general description of supercritical flow in rectangular and trapezoidal channels. Knapp provides a means of estimating the superelevation and standing waves within a curve and points out that waves generated in a curve are continued downstream. Knapp's assumptions include those given by Ippen with the addition that the velocity is constant across the cross-section. Knapp states that in trapezoidal channels the depth is not constant and that the wave celerity therefore varies throughout the cross section making his findings much less applicable to trapezoidal channels. He cautions channel designers that the additive effects of curves separated by short distances are not treated in his analyses since his method neglects the nonuniform velocity distribution across the beginning section of the downstream curve. The skewed velocity distribution entering the downstream curve is generated by flow through the upstream curve.

Considerations are given by Rouse et al. (1951) for the design of channel

expansions in the presence of supercritical flow. Their assumptions include hydrostatic pressure distribution, negligible friction losses, a flat channel (no slope), and vertical sidewalls. Rouse et al. provide graphical means for estimating the surface configuration of the negative wave generated at abrupt expansions and provide guidance for the design of efficient channel expansions which eliminate disturbances at the downstream end of the transition.

One-Dimensional Analysis

Typically, in engineering applications, open channel flow is analyzed using empirical one-dimensional hydraulic equations where the velocity and the water surface elevation are assumed constant over a cross section. Fluid frictional losses in uniform flow in straight prismatic channel sections are represented with either the Manning or Chezy equation. Empirical expressions have been developed to estimate the head losses (Henderson 1966) and superelevation of the water surface in channel curves (Woodward and Posey 1941). Flow obstructions such as bridge piers have been studied and parameters such as pier loss coefficients (USAE Los Angeles District 1939) have been quantified for simple geometric configurations. Hydraulic research has resulted in design criteria for channel width transitions (Brater and King 1976, US Bureau of Reclamation 1967, Ippen and Dawson 1951). The general location of a hydraulic jump in a straight prismatic rectangular channel is determined by backwater computations from a downstream control point and forward step computations from an upstream control point until the momentum equation of the hydraulic jump is satisfied.

A more complete analysis must be conducted for complex geometries having

variable cross sections or obstacles in the flow. This often involves using a physical hydraulic model. The time and cost requirements of physical models are necessitating the continued development and use of numerical flow models for analyzing flow patterns in complex channels.

Two-Dimensional Analysis

One-dimensional analyses are not adequate to describe flow patterns in which the depth-averaged velocity varies across the cross section, particularly in the analysis of supercritical flow. Moreover, the one-dimensional analysis fails to describe the additive effect of disturbances created at various points along a channel reach such as two curves separated by a short distance. One-dimensional modeling of channel features such as bridge piers and transitions requires knowledge of applicable loss coefficients. While significant research has been directed toward quantifying these coefficients, general energy loss relations have not been documented for complicated geometries such as at bridges having complex pier configurations, at skewed bridges, or at bridges crossing channel bends. A more complete description of the flow is provided by a depth-averaged two-dimensional analysis where the horizontal velocities and the water surface elevation vary in both the longitudinal and transverse directions. Two-dimensional modeling of flow around bridge piers and through transitions does not require empirical loss coefficients but rather only requires adequate boundary descriptions.

Depth-averaged two-dimensional flow analysis is conducted using the shallow water equations. The shallow water equations, sometimes referred to as the de Saint-

Venant equations, have been used to describe two-dimensional steady and transient free-surface flows. The principle assumption in this system of non-linear hyperbolic partial differential equations is that vertical accelerations are negligible, which is equivalent to assuming that the pressure distribution is hydrostatic. This assumption is adequate when the water surface curvature is small compared to the depth of channel flow. The channel slope is often considered geometrically mild such that $\sin \alpha \approx \tan \alpha \approx \alpha$, where α is the channel slope. This assumption is excellent for $\alpha < 5$ degrees and so is applicable to man-made channels passing through alluvial valleys having maximum slopes of about 0.015 (≈ 0.9 degrees). This geometrically mild slope assumption which complements the hydrostatic assumption is distinguished from a hydraulically mild slope which conveys uniform flow in the subcritical regime. That is, the shallow water equations assume the slope is geometrically mild although it may be hydraulically steep. The shallow water equations are capable of modeling both subcritical and supercritical flows. The depth-averaged two-dimensional flow equations used in this dissertation are presented in Chapter 3.

Analytical solutions of these equations are not available for two-dimensional problems unless simplifying assumptions are made. Generally, steady fluid flow is assumed and often the depth and cross sectional velocity distributions are prescribed as boundary conditions. Because there are no general analytical solutions available for the shallow water equations for general boundary geometry and transient channel inputs, the equations are solved numerically. Until recently, the majority of fluid dynamics and hydraulic problems have been numerically modeled using the finite

difference method. In particular the MacCormack, Lax, Gabutti, and Beam and Warming schemes have been applied to the shallow water equations in modeling supercritical flow in rectangular channels in which fluid flow shocks are created (Jimenez and Chaudhry 1988; Fennema and Chaudhry 1989, 1990; Elliot and Chaudhry 1992; Molls 1992; and Younus and Chaudhry 1994). These schemes are explained in texts such as Anderson et al. (1984). The finite element method is employed because of its ability to describe the boundaries of complex geometries accurately and its straight forward manner of satisfying boundary conditions (Katopodes 1984a and 1984b, Olsen 1974).

In the solution of two-dimensional open channel flow equations the local cross-section and depths are unknown quantities. Numerical solution of the flow variables treats the flow field as a number of discrete flow regions. If the channel sidewalls are vertical, the plan view domain is well defined such that one can easily discretize the domain. A computational grid can be constructed to represent the channel. However, if the channel has sloping sidewalls, the plan view of the flow domain, as delineated by the water surface/bank interface (i.e. the "waterline"), is not known a priori. The width of the flow field is unknown because it depends on the water surface elevation.

Simultaneous satisfaction of all variables in the steady form of the shallow water equations for specific geometry and flow rate over a particular portion of a channel requires use of iterative procedures because the equations are nonlinear. The success of an iteration technique depends on the quality of the initial estimate. An adequate initial estimate of the flow variables is difficult to establish for flow fields

which contain features such as standing waves and hydraulic jumps. The numerical model can use a time marching procedure to address transient processes or to calculate a steady state flow condition as a time asymptotic limit of a time dependent problem. Therefore, although steady flow solutions are addressed in this study, side boundary locations consistent with initial conditions which are not the steady state solution are assumed. Given these assumed initial conditions and side boundary locations, solution of the transient shallow water equations is proceeded in time until the steady state solution is obtained. This process is known as "time stepping" to steady state and can be viewed as an iteration procedure in time. At each time step, Newton-Raphson iterations are used to solve the nonlinear equations. As the computed flow field evolves from the specified assumed initial flow conditions and initial free surface/channel boundary location to the steady state, the side boundaries are adjusted. This constitutes a moving boundary problem.

Objectives

The primary focus of this study is the development of a method for analyzing flow in trapezoidal high-velocity channels where the flow can be subcritical or supercritical and may undergo transition from one regime to the other. This analysis is primarily concerned with water surface elevation predictions because the determination of the water surface characteristics is essential in the successful design and evaluation of flood control channels. Flow simulations are conducted using a depth-averaged two-dimensional finite element model with moving boundaries. When applied to supercritical flow, the numerical magnitude of the nonlinear terms in the

governing equations are large. Therefore, a proper moving boundary algorithm for supercritical flow must be designed to circumvent computational instabilities. To avoid computational instabilities a novel means for solving the boundary displacement and the flow variables simultaneously for the moving boundary problem is developed. Tests of the computational model consisting of comparisons with laboratory flume data demonstrate that supercritical flow in channels having sloping sidewalls can be modeled satisfactorily using the shallow water equations.

Specifically, this dissertation includes the following:

- (a) Extension of the shallow water equations to include a moving reference frame.

These depth-averaged two-dimensional flow equations describe the effects of moving boundaries.

- (b) Development of a numerical model of these moving boundary shallow water equations. This numerical model emphasizes numerical stability for advection dominated flow containing shocks such as oblique standing waves, characteristic of supercritical flow.

- (c) Demonstration that the model reproduces an analytic solution of the shallow water equations of steady ideal flow in a bend of a V-shaped channel.

- (d) Model tests comparing simulation results with measurements obtained in laboratory flumes. The tests include supercritical flow in four geometric configurations:

- (i) a trapezoidal-to-rectangular transition,
- (ii) a trapezoidal channel having a horizontal curve,

- (iii) a rectangular-to-trapezoidal transition, and
- (iv) a trapezoidal channel having flow obstructions geometrically similar to bridge piers.

Outline of Dissertation

A description of flow and design features of trapezoidal high-velocity channels has been given above. Chapter 2 reviews the methods that other researchers have proposed for modeling moving boundary flow problems. In Chapter 3 the depth-averaged two-dimensional conservation equations are developed to include the effects of a moving reference frame. The equations are established in this form to enable the formulation of a moving finite element model for advection dominated flow fields (Chapter 4). Chapter 5 compares computed numerical model results with an analytic solution. Additional model testing is described in Chapter 6. Chapter 7 presents the conclusions and an outline of additional research for model extensions.

CHAPTER 2

PREVIOUS RESEARCH

This chapter presents a review of previous research in numerical modeling of moving boundary problems. This review is divided into three main parts beginning with a brief listing of physical problems involving moving boundaries. Next, some examples of efforts directed toward solving laterally-averaged two-dimensional problems are given. The final portion of this chapter discusses various methods used to model depth-averaged two-dimensional flow problems having moving boundaries. These modeling schemes can be divided into three categories: the wetting and drying method; the transformation method; and the method selected for this study, the moving finite element method.

Moving Boundary Flow Problems

Physical phenomena involving moving boundary flow problems include the solid-liquid interface associated with the melting and solidification of metals, glass, and semiconductor crystals (Yoo and Rubinsky 1986, McLay 1988) and slide coating in the manufacture of photographic products (Kistler and Scriven 1984, Christodoulou and Scriven 1989). A review of the early efforts at modeling these problems is given by Lynch and Gray (1980).

In the hydraulic arena, the water surface of open channel flow is a free boundary and if the sidewalls are sloping, the side boundaries are located where the free surface intersects the sloping sidewalls. Transient three-dimensional analysis of open channel flow in trapezoidal channels must consider boundary movement in the horizontal and vertical directions. Unsteady two-dimensional modeling of these flow

fields reduces the moving boundary to a free-surface calculation in laterally-averaged models or to a problem of finding the waterline in depth-averaged models.

Laterally-Averaged Models

Free-surface models have been developed for flow over spillways (Ikegawa and Washizu 1973, Diersch and Martin 1978, and Bettess and Bettess 1983), flow under sluice gates (McCorquodale and Li 1971), unconfined ground water flow (Neuman and Witherspoon 1971, Finn and Varoglu 1976, and France 1980), sloshing flow and solitary wave propagation/runup (Betts and Hall 1978, Ramaswamy and Kawahara 1987, Okamoto et al. 1992, and Takizawa et al. 1992), flow at a hydraulic jump (Chippada et al. 1994), and dam break simulation (Wang and Wang 1994). This list is by no means complete, but these examples are a good representation of the research effort that has been directed toward these areas.

Bettess and Bettess (1983) summarize that finite element modeling of free-surface flow typically uses one of the following approaches:

- (a) Fix the element mesh and then vary the element properties to simulate the actual boundary. This method has been used to simulate the saturated and unsaturated zones of seepage through porous media where the kinetic energy of the flow is small (Anderson and Woessner 1992).
- (b) Invert the problem such that the grid coordinates are the dependent variables and then assuming ideal fluid flow, use the stream function and velocity potential as the independent variables (Finn and Varoglu 1976). This method is not applicable to flow subject to boundary resistance.

- (c) Construct a finite element mesh from the channel bed to an assumed free surface and then move the mesh in accordance with iterative solutions of the free surface, until convergence is achieved (Ikegawa and Washizu 1973, Betts 1978, and Washizu et al. 1976).

Each of these approaches can be applied to problems where the location of the boundary is unknown a priori. However, modeling supercritical flow while including boundary frictional effects excludes the use of methods (a) and (b). The ideas associated with method (c) are similar to many of those used to solve the depth-averaged equations applied to subcritical flow fields. These iterative methods of mesh adjustment for the shallow water equations are described in the next section.

Depth-Averaged Models

A common method of modeling open channel flow with sloping sidewalls uses a fixed grid with an imaginary fixed vertical barrier near the boundary, as shown in figure 2.1, rather than a moving boundary. However, this does not produce the correct incident wave reflection due to frictional differences (Lynch and Gray, 1978). That is, the bed drag that would occur in the absence of the imaginary fixed barrier is not reproduced. Frictional losses near the waterline in the real system are not modeled using an imaginary fixed barrier.

This method could be applied to high-velocity channels; however, in the supercritical flow regime, the steady state waterline may have significant spatial variation along the channel. This, in conjunction with the possibility that the depth at the imaginary barrier may become zero as the solution is time stepped to steady state,

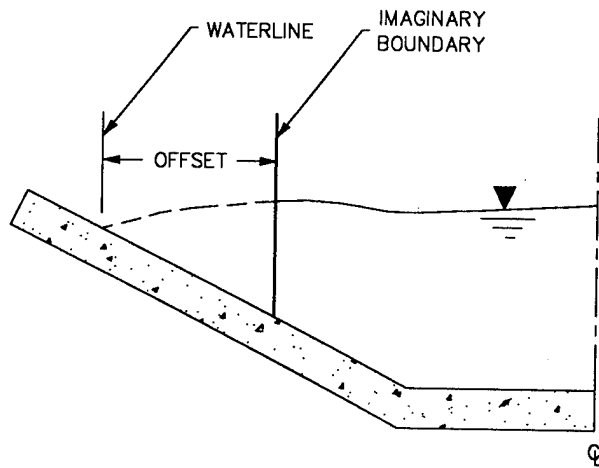


Figure 2.1. Half section sketch showing imaginary fixed vertical barrier.

requires that the imaginary barrier be offset far from the expected final waterline. Also, since the celerity of gravity waves is a function of flow depth, the plan view shapes of standing waves in the real system are not properly modeled using a fixed vertical barrier.

Depth-averaged moving boundary flow problems have been solved using one of three methods. The three methods are the wetting and drying method, the transformation method, and the method of moving finite elements.

Wetting and Drying Method

The most commonly used method employs a fixed spatial grid with the grid extended to cover the boundary motion. Subsequently, the grid is adjusted iteratively to cover the domain width as a function of the computed depth.

This method typically is implemented using wet and dry nodes. If the nodes in a grid cell are dry, then the cell is "turned off". The cell is no longer considered in

the flow domain. This method has been applied to the two-dimensional shallow water equations using both the finite difference (Reid and Bodine 1968, Leendertse 1970) and finite element methods (Holz and Withum 1977). Lynch and Gray (1980), discuss the early attempts at modeling moving boundary problems in this manner. More recent finite element solutions of the shallow water equations using wetting and drying are given by Kawahara and Umetsu (1986) and Leclerc et al. (1990).

Accurate solutions of the shallow water equations are difficult to obtain using the wetting and drying method because this method does not conserve mass or momentum. Each time a cell is added or subtracted to the domain there is an instantaneous change in the momentum near the boundary and in the total volume of fluid in the flow field. Holz and Nitsche (1980) propose a scheme to insure mass conservation; however, their model does not conserve momentum which requires the dynamics on all partly wetted elements be considered. The primary concerns of using the wetting and drying concept to model flow in trapezoidal high-velocity channels are that the method can produce a jagged grid rather than the smooth boundary which actually occurs, rapid changes in boundary location followed by periods of no boundary movement, and stability problems in advection dominated flow (discussed in Chapter 4). In supercritical flow, the jagged boundary itself will create shocks and steady state convergence may not be obtainable without using a very fine grid near the boundaries.

Transformation Method

A second method of simulation consists of a transformation procedure whereby

the grid is transformed back in time to its initial configuration. Lan et al. (1992) apply this method to the one-dimensional shallow water equations to compute the water surface elevation and transverse velocity of water sloshing from side to side in a canal having a parabolic bathymetry in which the transverse direction is aligned with the x axis. The advantage of this method is that established numerical methods for fixed-grid problems can be used and that the boundary movement has no limitation. However, the interpolation of the bathymetry relies on a prescribed spatial relation. The bathymetry of the one-dimensional example given by Lan et al. is easily described in functional form because the bed elevation in the direction of flow which is across the channel is a parabola varying only in the x direction. Complex boundary configurations are difficult to describe in functional Euclidian geometrical form.

The flow conditions in high-velocity channels are determined predominately by the geometric configuration of the channel boundaries. Therefore, modeling high-velocity channels requires accurate depictions of the bottom and sidewall geometry. The transformation scheme seems feasible for problems with simple relations between bottom geometry and horizontal position. However, it does not seem advantageous for two-dimensional modeling of high-velocity channels because of the difficulty in prescribing the channel boundaries in a three-dimensional functional form. Three-dimensional descriptions of complex trapezoidal high-velocity channel configurations functionally must describe channel side slopes, location of side slope toes, and sidewall/side slope interception in wedge type rectangular-to-trapezoidal (and trapezoidal-to-rectangular) transitions. Also, plan view variations such as horizontal

curves and transitions are difficult to describe in a functional form.

Moving Finite Element Method

The third general method of modeling moving boundary problems, using finite elements, involves adapting the grid to adjust the size and number of elements near the side of the domain, coincident with the solution depth. This is a form of the moving finite element method. Papers concerning the general subject of moving finite elements have been written by Lynch (1982) with application to phase change problems and by Miller and Miller (1981) and Miller (1981) in accurately solving the Burgers' equation (see Finite Element Formulation section in Chapter 4) by concentrating the grid density near flow shocks. A thorough description of the techniques involved in implementing the method of moving finite elements is given by Baines (1994).

There are two common means of accounting for flow problems in which the flow varies in time. Each of these moving grid techniques involves a transformation between two grids whereby nodal points are moved into new positions. These moving finite element methods are applicable to problems that are time stepped from assumed initial conditions to the steady state solution. Both of these methods differ from their fixed domain counterparts with respect to temporal derivatives. One method describes temporal derivatives relative to a fixed coordinate system. Using this method, the variation in time of the finite element basis (or interpolation) functions must be accounted for. This manner of describing temporal derivatives has been employed for simulations of estuary-sized problems using the shallow water equations by Lynch and

Gray (1978) and using the shallow water wave equations by Lynch and Gray (1980) and Siden and Lynch (1988). Lynch and O'Neil (1981) solve the two-phase Stefan problem and Neuman and Witherspoon (1971) compute the free surface of unconfined groundwater flow accounting for temporal derivatives in this manner.

The alternative method expresses the governing equations in a coordinate system which moves with respect to the original fixed reference frame. Examples of this application are given by Ramaswamy and Kawahara (1987) using the arbitrary Lagrangian-Eulerian (ALE) description of the fluid domain applied to a width-averaged model, MacKinnon and Carey (1993) modeling thermal ablation and consolidation in porous media, and Akanbi and Katopodes (1988) simulating the propagation of flood waves on initially dry land.

Lynch (1982) shows that these two methods produce identical weighted residual forms of the partial differential equation to be solved. Following the explanation given by Lynch (1982), a partial differential equation

$$\frac{\partial U}{\partial t} + LU = f \quad (2.1)$$

is examined for which a solution of $U = U(\mathbf{x}, t)$ is sought for a deforming grid. Here, t is time and the operator L contains the unknown function U and its spatial derivatives. The weighted residual form on a fixed grid is

$$\int_{\Omega} w_i \left(\frac{\partial \tilde{U}}{\partial t} + L\tilde{U} - f \right) d\Omega = 0 \quad \text{for all } i \quad (2.2)$$

where the integral is over the spatial domain Ω , $\tilde{U} = \tilde{U}(\mathbf{x}, t)$ is the approximate numerical solution of U , and W_i are the weighting functions. The numerical solution of U (\tilde{U}) is obtained via interpolation as

$$\tilde{U} = \sum_j \phi_j U_j \quad (2.3)$$

where ϕ_j are the basis functions and j is the node location.

The temporal derivative of \tilde{U} is

$$\frac{\partial \tilde{U}}{\partial t} = \sum_j \left(\frac{\partial U_j}{\partial t} \phi_j + U_j \frac{\partial \phi_j}{\partial t} \right). \quad (2.4)$$

Lynch shows that

$$\frac{\partial \phi_j}{\partial t} = -\mathbf{V}^e \cdot \nabla \phi_j \quad (2.5)$$

where \mathbf{V}^e is termed by Lynch as the "elemental velocity". Substitution of 2.5 into 2.4 yields

$$\frac{\partial \tilde{U}}{\partial t} = \sum_j \frac{\partial U_j}{\partial t} \phi_j - \mathbf{V}^e \cdot \nabla \tilde{U}. \quad (2.6)$$

Then the weighted residual form is

$$\int_{\Omega} W_i \left(\sum_j \frac{\partial U_j}{\partial t} \phi_j - \mathbf{V}^e \cdot \nabla \tilde{U} + L\tilde{U} - f \right) d\Omega = 0. \quad (2.7)$$

Lynch points out that the term $\mathbf{V}^e \cdot \nabla \tilde{U}$ "corrects the time derivatives to account for element deformation". Employment of this technique in which the temporal

derivatives are described relative to a fixed coordinate system produces a basis function that is time dependent (equation 2.5).

An alternative approach using coordinate transformations utilizes spatial coordinates χ which move relative to a fixed reference frame whose spatial coordinates are \mathbf{X} . The coordinate transformation can be stated as

$$\mathbf{X} = \mathbf{X}(\chi, t) \quad (2.8)$$

and the time derivative of a dependent variable U is given as

$$\left. \frac{\partial U}{\partial t} \right|_{\chi} = \left. \frac{\partial U}{\partial t} \right|_{\mathbf{X}} + \left. \frac{\partial \mathbf{X}}{\partial t} \right|_{\chi} \cdot \nabla U \quad (2.9)$$

where ∇ refers to the fixed reference frame coordinates, \mathbf{X} , with constant t .

Substitution into the partial differential equation, 2.1, yields

$$\left. \frac{\partial U}{\partial t} \right|_{\chi} - \left. \frac{\partial \mathbf{X}}{\partial t} \right|_{\chi} \cdot \nabla U + LU = f. \quad (2.10)$$

If the moving coordinate system, χ , is identified with the local coordinate system which is also used for the finite element basis functions, then the numerical representations of the temporal derivatives in 2.9 are

$$\left. \frac{\partial \tilde{U}}{\partial t} \right|_{\chi} = \sum_j \frac{\partial U_j}{\partial t} \phi_j \quad (2.11)$$

and

$$\left. \frac{\partial \mathbf{X}}{\partial t} \right|_x = \sum_j \frac{\partial \mathbf{X}_j}{\partial t} \phi_j = \mathbf{V}^e . \quad (2.12)$$

The weighted residual form of 2.10 is

$$\int_{\Omega} W_i \left(\sum_j \frac{\partial U_j}{\partial t} \phi_j - \mathbf{V}^e \cdot \nabla \tilde{U} + L \tilde{U} - f \right) d\Omega = 0 \quad (2.13)$$

which is identical to 2.7, yet because the spatial coordinate system which moves relative to a fixed reference frame is also the local coordinate system used to define the finite element basis functions, the basis functions are time invariant.

The equality of 2.7 and 2.13 illustrates that these two methods of describing moving finite elements produce the same weighted residual formulation. One can choose to express temporal derivatives relative to a fixed coordinate system and then account for the variation in time of the basis functions or express the governing equations in a coordinate system that moves with respect to the original reference frame. The latter method is used in this dissertation. The reasoning associated with this choice of methods is provided in the Moving Reference Frame Effects section of Chapter 3.

CHAPTER 3

EQUATIONS FOR MOVING BOUNDARY FLOW

The equations used to model open channel flow are presented in this chapter. First the depth-averaged two-dimensional conservation equations are given. These equations are then extended to include the effects of a moving reference frame. The equations are cast in this form to describe shallow water flow whose planform domain varies in time.

Shallow Water Equations

Water flow in open channels is often described using the depth-averaged equations of mass and momentum conservation, commonly referred to as the shallow water equations. The shallow water equations model horizontal motion of incompressible, Newtonian fluid flow where the vertical accelerations are negligible. The dependent variables of the two-dimensional fluid motion are defined by the flow depth (h), the x -direction component of depth-averaged velocity (u), and the y -direction component of depth-averaged velocity (v). These variables are functions of the independent variables x and y , the two space directions, and time (t). The variables are depicted schematically in figure 3.1.

Neglecting free-surface stresses and the Coriolis forces as these are insignificant in high-velocity channels, the shallow water equations in conservative form are given as (Liggett 1975, Abbott 1979, and Praagman 1979)

$$\frac{\partial h}{\partial t} + \frac{\partial(uh)}{\partial x} + \frac{\partial(vh)}{\partial y} = 0 \quad (3.1)$$

for the conservation of mass. The conservation of momentum in the x direction and y

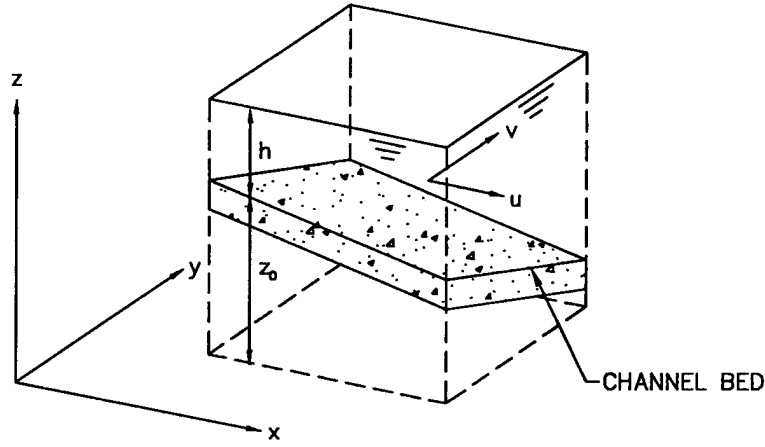


Figure 3.1. Flow variables.

direction are given respectively as

$$\begin{aligned} \frac{\partial(uh)}{\partial t} + \frac{\partial}{\partial x} \left(u^2 h + \frac{1}{2} g h^2 - \frac{h}{\rho} \sigma_{xx} \right) + \frac{\partial}{\partial y} \left(uvh - \frac{h}{\rho} \sigma_{xy} \right) \\ = - gh \frac{\partial z_0}{\partial x} - \frac{g n^2 u \sqrt{u^2 + v^2}}{C_0^2 h^{1/3}} \end{aligned} \quad (3.2)$$

and

$$\begin{aligned} \frac{\partial(vh)}{\partial t} + \frac{\partial}{\partial x} \left(uvh - \frac{h}{\rho} \sigma_{yx} \right) + \frac{\partial}{\partial y} \left(v^2 h + \frac{1}{2} g h^2 - \frac{h}{\rho} \sigma_{yy} \right) \\ = - gh \frac{\partial z_0}{\partial y} - \frac{g n^2 v \sqrt{u^2 + v^2}}{C_0^2 h^{1/3}} \end{aligned} \quad (3.3)$$

where

z_0 = channel invert (bed) elevation

g = acceleration due to gravity

n = Manning's roughness coefficient

ρ = fluid density

$C_0 = Cn/h^{1/6}$ is a dimensional constant (1 for SI units, 1.486 for English units) where C is the Chezy coefficient

and σ_{xx} , σ_{xy} , σ_{yx} , and σ_{yy} are the Reynolds stresses per unit area where the first subscript indicates the direction of the stress and the second indicates the axis direction normal to the face upon which the stress acts. The depth-averaged velocities u and v are temporally averaged values. The Reynolds stresses may be determined using the Boussinesq approach relating stress to the gradient in the mean currents

$$\sigma_{xx} = 2\rho v_t \frac{\partial u}{\partial x} \quad (3.4)$$

$$\sigma_{xy} = \sigma_{yx} = \rho v_t \left(\frac{\partial u}{\partial y} + \frac{\partial v}{\partial x} \right) \quad (3.5)$$

and

$$\sigma_{yy} = 2\rho v_t \frac{\partial v}{\partial y} \quad (3.6)$$

where v_t is the turbulent kinematic viscosity. The turbulent kinematic viscosity can be approximated empirically as a function of depth and velocity as discussed in Chapter

4.

The depth-averaged equations, 3.2 and 3.3, are derived by integration of the equations of motion over water depth. Depth integration of the momentum equations results in momentum transfer terms which can be cast in forms similar to stress terms (Praagman 1979). The resulting terms are commonly referred to as effective stresses resulting from the vertical variation of horizontal velocity (Kuipers and Vreugdenhil 1973).

These effective stresses resulting from the vertical variation of horizontal velocity are not directly included in 3.2 and 3.3. Exclusion of these terms implies the assumption that vertical variations in the horizontal velocities are negligible. Some analysts account for these effective stresses resulting from depth integration using momentum correction factors. The momentum correction factor applied to straight channels can vary from 1.2 for a parabolic vertical distribution of horizontal velocity to 1.05 for many turbulent flows (Liggett 1975). However, because in general their values are not known, empirical relations are often used to quantify the effective stresses. Coefficients used in these relations are based on flow measurements (equation 4.5) and so incorporate both the effects of the Reynolds stresses and the effective stresses attributable to depth integration.

Related velocity and depth products in the shallow water equations are redefined in terms of unit discharges

$$p \equiv uh \quad (3.7)$$

and

$$q \equiv vh \quad (3.8)$$

where p is the volumetric discharge per unit width in the x direction and q is the volumetric discharge per unit width in the y direction.

The variables p and q are substituted into the shallow water equations.

Because mass is conserved, these functions are smoother than u and v throughout regions in the flow field where the spatial gradients of h , u , and v are large such as at an oblique standing wave or at a hydraulic jump. Modeling of flows containing such gradients (shocks) using the shallow water equations requires that the depth-averaged equations be cast in this form (Abbott 1979). The governing equations are rewritten in terms of p and q and are expressed in vector form as

$$\frac{\partial \mathbf{Q}}{\partial t} + \frac{\partial \mathbf{F}_x}{\partial x} + \frac{\partial \mathbf{F}_y}{\partial y} + \mathbf{H} = \mathbf{0} \quad (3.9)$$

where

$$\mathbf{Q} = \begin{pmatrix} h \\ p \\ q \end{pmatrix} \quad (3.10)$$

$$\mathbf{F}_x = \begin{pmatrix} p \\ \frac{p^2}{h} + \frac{1}{2}gh^2 - \frac{h}{\rho}\sigma_{xx} \\ \frac{pq}{h} - \frac{h}{\rho}\sigma_{yx} \end{pmatrix} \quad (3.11)$$

$$\mathbf{F}_y = \begin{pmatrix} q \\ \frac{pq}{h} - \frac{h}{\rho}\sigma_{xy} \\ \frac{q^2}{h} + \frac{1}{2}gh^2 - \frac{h}{\rho}\sigma_{yy} \end{pmatrix} \quad (3.12)$$

and

$$\mathbf{H} = \begin{pmatrix} 0 \\ gh\frac{\partial z_0}{\partial x} + g\frac{n^2p\sqrt{p^2+q^2}}{C_0^2h^{7/3}} \\ gh\frac{\partial z_0}{\partial y} + g\frac{n^2q\sqrt{p^2+q^2}}{C_0^2h^{7/3}} \end{pmatrix} \quad (3.13)$$

Moving Reference Frame Effects

It was shown in Chapter 2 that the moving finite element method is an appropriate method for modeling supercritical flow in trapezoidal channels. The wetting and drying method does not conserve mass or momentum and may result in unrealistic jagged waterlines and can introduce nonphysical flow shocks. Although the transformation method is convenient because it uses existing fixed grid technology, it requires functional descriptions of the channel bed which are difficult or impractical to define for general high-velocity channels. The complex boundaries of high-velocity channels with contractions, expansions, slope breaks, sidewall slope transitions, curves, and bridge piers would be very difficult to describe with a functional geometrical

relation.

It was shown in Chapter 2 that two moving finite element methods, one using a fixed grid with a temporally varying basis function and the other expressing the governing equations in terms of a coordinate system that moves relative to the original fixed reference frame, produce the same weighted residual form of the governing equations (2.7 and 2.13). The latter method is used here because it is more physically intuitive and modification of the finite element basis function would be difficult due to the particular Petrov-Galerkin test function employed. The governing equations are modified to account for the moving reference frame effects rather than modifying the finite element basis function. A Petrov-Galerkin test function that is composed of a Galerkin part and a non-Galerkin component (see Petrov-Galerkin Test Function section in Chapter 4) is used here. Since the test function is defined in terms of the basis function, modification of the basis function to account for a moving reference frame is likely to be difficult and was not attempted.

The shallow water equations describe horizontal motion of incompressible (Newtonian) fluid flow relative to a fixed coordinate system. The approach used here in solving the moving boundary problem transforms the governing equations derived for a fixed coordinate system to a moving coordinate system by introducing a coordinate transformation (MacKinnon and Carey 1993, Akanbi and Katopodes 1988). The shallow water equations for a fixed coordinate system are expressed in terms of a moving reference frame by defining a new set of independent variables (ξ, η, τ) as a moving coordinate system which is related to the fixed reference frame (x, y, t) such

that

$$x = x(\xi, \eta, \tau) \quad (3.14)$$

$$y = y(\xi, \eta, \tau) \quad (3.15)$$

and

$$t = \tau . \quad (3.16)$$

The time derivative of the flow variables, \mathbf{Q} , taken in the moving reference frame is

$$\frac{\partial \mathbf{Q}}{\partial \tau} = \frac{\partial t}{\partial \tau} \frac{\partial \mathbf{Q}}{\partial t} + \frac{\partial x}{\partial \tau} \frac{\partial \mathbf{Q}}{\partial x} + \frac{\partial y}{\partial \tau} \frac{\partial \mathbf{Q}}{\partial y} \quad (3.17)$$

where $\partial \mathbf{Q} / \partial t$ is the time derivative in the fixed coordinate system and $\partial x / \partial \tau$ and $\partial y / \partial \tau$ are the moving reference frame velocities in the x and y directions, respectively. The reference frame velocity is expressed as

$$\mathbf{V}_r = \left(\frac{\partial x}{\partial \tau}, \frac{\partial y}{\partial \tau} \right) = (u_r, v_r) . \quad (3.18)$$

Therefore, since $\partial t / \partial \tau = 1$,

$$\frac{\partial \mathbf{Q}}{\partial t} = \frac{\partial \mathbf{Q}}{\partial \tau} - u_r \frac{\partial \mathbf{Q}}{\partial x} - v_r \frac{\partial \mathbf{Q}}{\partial y} . \quad (3.19)$$

Using the chain rule of differentiation,

$$u_r \frac{\partial \mathbf{Q}}{\partial x} = \frac{\partial(u_r \mathbf{Q})}{\partial x} - \frac{\partial u_r}{\partial x} \mathbf{Q} \quad (3.20)$$

and

$$v_r \frac{\partial \mathbf{Q}}{\partial y} = \frac{\partial(v_r \mathbf{Q})}{\partial y} - \frac{\partial v_r}{\partial y} \mathbf{Q} . \quad (3.21)$$

Then,

$$\frac{\partial \mathbf{Q}}{\partial t} = \frac{\partial \mathbf{Q}}{\partial \tau} - \frac{\partial(u_r \mathbf{Q})}{\partial x} - \frac{\partial(v_r \mathbf{Q})}{\partial y} + \left(\frac{\partial u_r}{\partial x} + \frac{\partial v_r}{\partial y} \right) \mathbf{Q} . \quad (3.22)$$

The shallow water equations written for a moving reference frame are obtained by substitution of 3.22 into 3.9

$$\begin{aligned} \frac{\partial \mathbf{Q}}{\partial \tau} - \frac{\partial(u_r \mathbf{Q})}{\partial x} - \frac{\partial(v_r \mathbf{Q})}{\partial y} + \left(\frac{\partial u_r}{\partial x} + \frac{\partial v_r}{\partial y} \right) \mathbf{Q} \\ + \frac{\partial \mathbf{F}_x}{\partial x} + \frac{\partial \mathbf{F}_y}{\partial y} + \mathbf{H} = \mathbf{0} . \end{aligned} \quad (3.23)$$

Rearranging yields

$$\begin{aligned} \frac{\partial \mathbf{Q}}{\partial \tau} + \frac{\partial}{\partial x} (\mathbf{F}_x - u_r \mathbf{Q}) + \frac{\partial}{\partial y} (\mathbf{F}_y - v_r \mathbf{Q}) \\ + \mathbf{H} + \left(\frac{\partial u_r}{\partial x} + \frac{\partial v_r}{\partial y} \right) \mathbf{Q} = \mathbf{0} . \end{aligned} \quad (3.24)$$

The vectors F_x^* and F_y^* are defined as

$$F_x^* \equiv F_x - u_r Q = \begin{Bmatrix} p - u_r h \\ \frac{p^2}{h} - u_r p + \frac{1}{2} g h^2 - \frac{h}{\rho} \sigma_{xx} \\ \frac{pq}{h} - u_r q - \frac{h}{\rho} \sigma_{yx} \end{Bmatrix} \quad (3.25)$$

and

$$F_y^* \equiv F_y - v_r Q = \begin{Bmatrix} q - v_r h \\ \frac{pq}{h} - v_r p - \frac{h}{\rho} \sigma_{xy} \\ \frac{q^2}{h} - v_r q + \frac{1}{2} g h^2 - \frac{h}{\rho} \sigma_{yy} \end{Bmatrix} \quad (3.26)$$

The shallow water equations can be expressed in terms of a moving reference frame as

$$\frac{\partial Q}{\partial \tau} + \frac{\partial F_x^*}{\partial x} + \frac{\partial F_y^*}{\partial y} + H + \left(\frac{\partial u_r}{\partial x} + \frac{\partial v_r}{\partial y} \right) Q = 0. \quad (3.27)$$

These equations can be used to describe shallow water flow whose domain may vary in time. Provided that adequate boundary conditions are imposed and initial conditions specified, these extended shallow water equations are appropriate for modeling flow in channels with sloping sidewalls.

CHAPTER 4

FINITE ELEMENT MODEL

The depth-averaged two-dimensional equations, 3.27, expressed in terms of a moving reference frame were developed in the previous chapter. These equations, which are appropriate for modeling depth-averaged moving boundary flow problems, form a system of mixed nonlinear elliptic and parabolic partial differential equations. Although these equations are of mixed type, in applications the Reynolds stresses are relatively small and the system behaves much as hyperbolic partial differential equations. The Reynolds stresses are important however in modeling flow fields containing eddies associated with streamlines separating from boundaries. Such flow fields are present in high-velocity channels in the vicinity of flow obstructions such as bridge piers.

These equations in general cannot be solved analytically. Therefore a numerical solution is required. The finite element method is chosen for the numerical representation of the governing equations because complex geometric details of high-velocity channels are easily represented by such elements and boundary conditions are readily imposed.

This chapter begins by expressing the partial differential equations in variational form. The reference frame velocities are then transformed to discrete finite element grid velocities (i.e. nodal velocities). Then the finite element form of the governing equations is presented. Next, to simplify boundary condition specifications and reduce functional continuity requirements, a weak form of the equations is developed. The Petrov-Galerkin test function which provides numerical stability is

then given. Following this the finite difference equation used to approximate the temporal derivatives is presented and then the appropriate number and type of boundary conditions are examined. The movement of interior nodes used to reduce the formation of ill shaped elements during boundary nodal displacement is then discussed followed by methods of selecting initial conditions. The last topic of discussion is the solution procedure which is presented in schematic form. Within the solution procedure, the Newton-Raphson iterative technique is used to solve the nonlinear finite element equations.

Finite Element Formulation

A variational formulation of the governing equations involves finding a solution of the dependent variables, \mathbf{Q} , using the test function, Ψ , over the domain, Ω . The variational form of the shallow water equations related to a moving reference frame is

$$\int_{\Omega} \Psi \left[\frac{\partial \mathbf{Q}}{\partial \tau} + \frac{\partial \mathbf{F}_x^*}{\partial x} + \frac{\partial \mathbf{F}_y^*}{\partial y} + \mathbf{H} + \left(\frac{\partial u_r}{\partial x} + \frac{\partial v_r}{\partial y} \right) \mathbf{Q} \right] d\Omega = 0 . \quad (4.1)$$

The finite element approach used is a Petrov-Galerkin formulation which incorporates a combination of the Galerkin test function and a non-Galerkin component to control numerical oscillations due to advection. Advection dominated flow refers to flow conditions in which the Reynolds number defined as

$$\text{Re} = \frac{h\sqrt{u^2 + v^2}}{\nu} \quad (4.2)$$

is large. Here, ν is the molecular kinematic viscosity of the fluid. This definition of advection dominated flow is somewhat ambiguous. A clearer definition from a numerical modeling standpoint is that advection dominated refers to flow fields which are modeled in such a manner that the mesh Reynolds number (also called the Peclet number) is large. The mesh Reynolds number, defined as

$$\text{Re}_\ell = \frac{\ell\sqrt{u^2 + v^2}}{\nu_t} \quad (4.3)$$

can be viewed as a ratio of advection to diffusion where ℓ is the element mesh parameter (the characteristic length of the grid cells).

Burgers' equation, which contains an advection and a diffusion term, serves as an analog of the governing equations. The linearized Burgers' equation can be expressed as

$$\frac{\partial u}{\partial t} + u_0 \frac{\partial u}{\partial x} = \nu_t \frac{\partial^2 u}{\partial x^2} \quad (4.4)$$

where u_0 is a constant advection speed. Stability analysis of the linearized Burgers' equation shows that Galerkin finite element schemes using linear interpolation (or finite difference methods using central differences) are stable for mesh Reynolds numbers less than or equal to 2 (Anderson et al. 1984). Therefore, in the work presented here the term advection dominated is applied to modeled flow having a

mesh Reynolds number greater than 2.

An order of magnitude analysis of the flows simulated and numerical grids used here provides an estimate of the magnitude of the mesh Reynolds number. In open channel flow where the turbulence is mainly generated by bed drag, it is reasonable to relate the horizontal diffusion of momentum to the bed stress. Therefore, the turbulent kinematic viscosity here is described empirically (Rodi 1980, and Chapman and Kuo 1985) as

$$\nu_t = C_b \sqrt{f} h \sqrt{u^2 + v^2} . \quad (4.5)$$

Here f is the Darcy-Weisbach friction factor and C_b is a coefficient which varies between 0.1 and 1.0. It has been shown that values of the turbulent kinematic viscosity coefficient, C_b , in the range of 0.1 to 0.2 are appropriate for modeling high-velocity channel flows (Berger 1993 and Stockstill and Berger 1994). In design practice an engineer should conduct simulations with various values of C_b and Manning's n using this range to establish an envelope of possible resulting flow conditions. This turbulence model which indicates variation of turbulent kinematic viscosity with local depth and velocity, is however used in the present study to determine a constant turbulent kinematic viscosity for the entire flow field based on depth and velocity for uniform flow. This simple turbulence model is deemed adequate for the purposes of this dissertation to model high-velocity channels where the primary concern is obtaining an accurate solution of the flow depth whereby the sidewall heights can be appropriately designed to contain flood flows.

Substituting 4.5 into 4.3 results in an expression of the mesh Reynolds number in terms of variables for which an order of magnitude (or range of order) is known.

$$\text{Re}_\ell = \frac{\ell}{C_b \sqrt{f} h} \quad (4.6)$$

The mesh characteristic length and the flow depth are of the same order of magnitude,

$$\frac{\ell}{h} = O(10^0)$$

where $O(\)$ is the "order of". The value of C_b varies as

$$O(10^{-1}) \leq C_b \leq O(10^0) .$$

The Darcy-Weisbach friction factor for the hydraulically smooth boundaries of concrete-lined high-velocity channels is $O(10^{-2})$. The mesh Reynolds number is seen to vary from $O(10^1)$ for a C_b value of $O(10^0)$ to $O(10^2)$ for C_b of $O(10^{-1})$. For the problems addressed here, the mesh Reynolds number is always greater than 2, the model must use a numerical scheme which is stable in advection dominated flow.

In the finite element form, the reference velocity is taken to be the velocity of the grid, $\mathbf{V}_r = \mathbf{V}_g = (u_g, v_g)$. Therefore, $\mathbf{F}_x^* = \mathbf{F}_x - \mathbf{Q}u_g$ and $\mathbf{F}_y^* = \mathbf{F}_y - \mathbf{Q}v_g$. Then the finite element form of 3.27 is

$$\sum_e \left\{ \int_{\Omega_e} \psi_i \left[\frac{\partial \tilde{Q}}{\partial \tau} + \frac{\partial \tilde{F}_x^*}{\partial x} + \frac{\partial \tilde{F}_y^*}{\partial y} + \tilde{H} + \left(\frac{\partial \tilde{u}_s}{\partial x} + \frac{\partial \tilde{v}_s}{\partial y} \right) \tilde{Q} \right] d\Omega_e \right\} = 0, \text{ for each } i. \quad (4.7)$$

The symbol "~" indicates the discrete value of the quantity, e indicates a particular element, and i indicates a particular test function. The grid velocity is determined in terms of the nodal displacement rate. The displacement vector of a node is

$$\mathbf{s} = |\mathbf{s}| \hat{\boldsymbol{\theta}} = (|\mathbf{s}| \theta_x, |\mathbf{s}| \theta_y) \quad (4.8)$$

where $|\mathbf{s}|$ is the magnitude of the displacement vector and $\hat{\boldsymbol{\theta}}$ is the unit vector in the direction of allowable nodal movement. Specification of the direction of allowable nodal movement is arbitrary at this point in the model development. Because the lateral width of the flow field is sought, specifying the direction of movement as a function of the side slopes is a logical choice. Therefore, boundary nodes located on the channel side slopes are restricted to moving in the direction of maximum channel side slope (see figure 4.1). That is, $\hat{\boldsymbol{\theta}}$ is a unit vector in the x-y plane directed toward the maximum side slope. Given that \mathbf{s} is the nodal displacement vector, then the grid velocity is $\mathbf{V}_g = d\mathbf{s}/d\tau$.

The moving coordinate system is identified with the local coordinate system which is also used for the basis functions. The geometry and flow variables are subsequently interpolated using the Lagrange basis functions

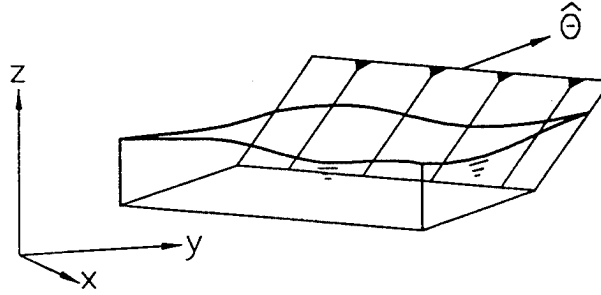


Figure 4.1. Definition sketch of the direction of allowable nodal movement, $\hat{\theta}$.

$$\tilde{Q} = \sum_j \phi_j \tilde{Q}_j \quad (4.9)$$

and

$$\tilde{s} = \sum_j \phi_j \tilde{s}_j \quad (4.10)$$

where ϕ is the basis function and j is the node location. Bilinear triangular and quadrilateral elements are used with nodes at the element corners. Figure 4.2 shows the two bilinear elements used in terms of local coordinates ξ and η .

The test function used (to be elaborated on later in this chapter) is

$$\psi_i = \phi_i \mathbf{I} + \varphi_i \quad (4.11)$$

where ϕ_i is the Galerkin part of the test function (identical to the basis function), φ_i is the non-Galerkin part, and \mathbf{I} is the identity matrix.

To facilitate the specification of boundary conditions, a weak form (see page 44) of 4.7 is developed. The practical weak form which is equivalent to that given in

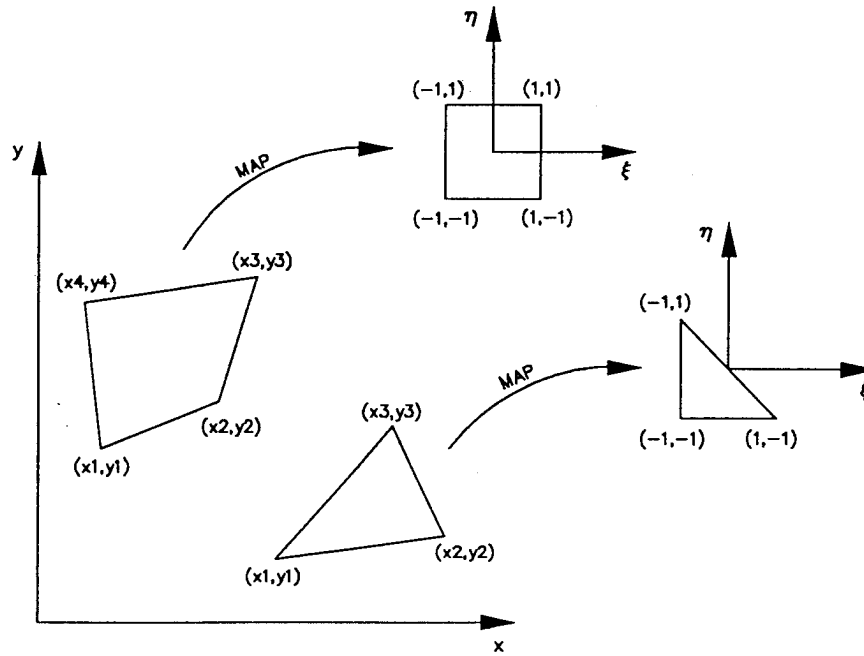


Figure 4.2. Transformation from global coordinates to local (bilinear element) coordinates.

4.7 is found using an integration by parts procedure. The weak form includes boundary integrals that are actually natural boundary conditions for the shallow water equations. Using Gauss's Theorem, integration by parts of the terms

$$\phi_i \frac{\partial F_x^*}{\partial x}$$

and

$$\phi_i \frac{\partial F_y^*}{\partial y}$$

are given as

$$\int_{\Omega_e} \phi_i \frac{\partial \mathbf{F}_x^*}{\partial x} d\Omega_e = - \int_{\Omega_e} \mathbf{F}_x^* \frac{\partial \phi_i}{\partial x} d\Omega_e + \oint_{\Gamma} \phi_i \mathbf{F}_x^* n_x d\Gamma \quad (4.12)$$

and

$$\int_{\Omega_e} \phi_i \frac{\partial \mathbf{F}_y^*}{\partial y} d\Omega_e = - \int_{\Omega_e} \mathbf{F}_y^* \frac{\partial \phi_i}{\partial y} d\Omega_e + \oint_{\Gamma} \phi_i \mathbf{F}_y^* n_y d\Gamma \quad (4.13)$$

where $(n_x, n_y) = \hat{\mathbf{n}}$ is the unit vector outward normal to the boundary Γ .

Incorporating the results of the integration by parts procedure into 4.7 yields the weak form of the equations which is

$$\begin{aligned} \sum_e \left\{ \int_{\Omega_e} \left[\psi_i \frac{\partial \mathbf{Q}}{\partial \tau} - \mathbf{F}_x^* \frac{\partial \phi_i}{\partial x} - \mathbf{F}_y^* \frac{\partial \phi_i}{\partial y} + \phi_i \left(\frac{\partial \mathbf{F}_x^*}{\partial x} + \frac{\partial \mathbf{F}_y^*}{\partial y} \right) \right. \right. \\ \left. \left. + \psi_i \left(\mathbf{H} + \left(\frac{\partial u_g}{\partial x} + \frac{\partial v_g}{\partial y} \right) \mathbf{Q} \right) \right] d\Omega_e \right. \\ \left. + \oint_{\Gamma} \phi_i (\mathbf{F}_x^* n_x + \mathbf{F}_y^* n_y) d\Gamma \right\} = 0, \text{ for each } i \end{aligned} \quad (4.14)$$

where "~" is omitted for clarity; the variables are understood to be discrete values.

This form of the equations is named weak because the functional continuity requirements of the vectors \mathbf{F}_x^* and \mathbf{F}_y^* in the terms $\phi \partial \mathbf{F}_x^* / \partial x$ and $\phi \partial \mathbf{F}_y^* / \partial y$ have been "weakened". The weak form only requires that the basis functions be continuous

whereas the original form requires a basis function with continuous first derivatives.

Also, the weak formulation essentially relaxes the boundary condition enforcement such that natural boundary conditions are enforced in an average sense. Treatment of natural boundary conditions is discussed in the Boundary Conditions section of this chapter.

Equation 4.14 can be simplified first by realizing that $\mathbf{F}_x^* = \mathbf{F}_x^*(\mathbf{Q}, s)$ and $\mathbf{F}_y^* = \mathbf{F}_y^*(\mathbf{Q}, s)$ and expanding the momentum matrix terms as

$$\frac{\partial \mathbf{F}_x^*}{\partial x} = \frac{\partial \mathbf{F}_x^*}{\partial \mathbf{Q}} \frac{\partial \mathbf{Q}}{\partial x} + \frac{\partial \mathbf{F}_x^*}{\partial s} \frac{\partial s}{\partial x} \quad (4.15)$$

and

$$\frac{\partial \mathbf{F}_y^*}{\partial y} = \frac{\partial \mathbf{F}_y^*}{\partial \mathbf{Q}} \frac{\partial \mathbf{Q}}{\partial y} + \frac{\partial \mathbf{F}_y^*}{\partial s} \frac{\partial s}{\partial y} \quad (4.16)$$

Next, the convection matrices \mathbf{A}^* and \mathbf{B}^* are defined as

$$\mathbf{A}^* \equiv \frac{\partial \mathbf{F}_x^*(\mathbf{Q})}{\partial \mathbf{Q}} = \begin{bmatrix} -u_g & 1 & 0 \\ (c^2 - u^2) & (2u - u_g) & 0 \\ -(uv) & v & (u - u_g) \end{bmatrix} \quad (4.17)$$

and

$$\mathbf{B}^* \equiv \frac{\partial \mathbf{F}_y^*(\mathbf{Q})}{\partial \mathbf{Q}} = \begin{bmatrix} -v_g & 0 & 1 \\ -(uv) & (v-v_g) & u \\ (c^2-v^2) & 0 & (2v-v_g) \end{bmatrix} \quad (4.18)$$

where $c = (gh)^{1/2}$ is the celerity of a small gravity wave in shallow water resulting from a disturbance in the local depth. The convection matrices are used to define the characteristic based test function. A discussion including the development of the test function used here is provided in the next section.

Evaluation of the derivatives with respect to s gives

$$\frac{\partial \mathbf{F}_x^*}{\partial s} = \frac{\partial}{\partial s} \left\{ \begin{array}{c} p - u_g h \\ \frac{p^2}{h} - u_g p + \frac{1}{2} g h^2 - h \sigma_{xx} \\ \frac{pq}{h} - u_g q - h \sigma_{yx} \end{array} \right\} = -\frac{\partial u_g}{\partial s} \mathbf{Q} \quad (4.19)$$

and

$$\frac{\partial \mathbf{F}_y^*}{\partial s} = \frac{\partial}{\partial s} \left\{ \begin{array}{c} q - v_g h \\ \frac{pq}{h} - v_g p - h \sigma_{xy} \\ \frac{q^2}{h} - v_g q + \frac{1}{2} g h^2 - h \sigma_{yy} \end{array} \right\} = -\frac{\partial v_g}{\partial s} \mathbf{Q} . \quad (4.20)$$

Therefore, the momentum matrices are

$$\frac{\partial \mathbf{F}_x^*}{\partial x} = \mathbf{A}^* \frac{\partial \mathbf{Q}}{\partial x} - \frac{\partial u_g}{\partial x} \mathbf{Q} \quad (4.21)$$

and

$$\frac{\partial \mathbf{F}_y^*}{\partial y} = \mathbf{B}^* \frac{\partial \mathbf{Q}}{\partial y} - \frac{\partial v_g}{\partial y} \mathbf{Q} . \quad (4.22)$$

The resulting weak form which is found by substituting 4.21 and 4.22 into 4.14 is given as

$$\begin{aligned} \int_{\Omega} \left\{ \Psi \frac{\partial \mathbf{Q}}{\partial \tau} - \mathbf{F}_x^* \frac{\partial \phi}{\partial x} - \mathbf{F}_y^* \frac{\partial \phi}{\partial y} + \phi \left[\mathbf{A}^* \frac{\partial \mathbf{Q}}{\partial x} + \mathbf{B}^* \frac{\partial \mathbf{Q}}{\partial y} - \left(\frac{\partial u_g}{\partial x} + \frac{\partial v_g}{\partial y} \right) \mathbf{Q} \right] \right. \\ \left. + \Psi \mathbf{H} + \phi \left(\frac{\partial u_g}{\partial x} + \frac{\partial v_g}{\partial y} \right) \mathbf{Q} + \phi \left(\frac{\partial u_g}{\partial x} + \frac{\partial v_g}{\partial y} \right) \mathbf{Q} \right\} d\Omega \\ + \oint_{\Gamma} \phi (\mathbf{F}_x^* n_x + \mathbf{F}_y^* n_y) d\Gamma = 0. \end{aligned} \quad (4.23)$$

The final simplification is made by introducing a notation change. A new vector is defined as

$$\mathbf{G} \equiv \left(\frac{\partial u_g}{\partial x} + \frac{\partial v_g}{\partial y} \right) \mathbf{Q} . \quad (4.24)$$

Reduction of 4.23 produces the finite element description of the shallow water equations modified to account for moving reference frame effects

$$\begin{aligned}
\sum_e \left\{ \int_{\Omega_e} \left[\psi_i \left(\frac{\partial \mathbf{Q}}{\partial \tau} + \mathbf{H} \right) - \mathbf{F}_x^* \frac{\partial \phi_i}{\partial x} - \mathbf{F}_y^* \frac{\partial \phi_i}{\partial y} + \phi_i \mathbf{G} \right. \right. \\
\left. \left. + \phi_i \left(\mathbf{A}^* \frac{\partial \mathbf{Q}}{\partial x} + \mathbf{B}^* \frac{\partial \mathbf{Q}}{\partial y} \right) \right] d\Omega_e \right. \\
\left. + \oint_{\Gamma} \phi_i (\mathbf{F}_x^* n_x + \mathbf{F}_y^* n_y) d\Gamma \right\} = 0, \text{ for each } i.
\end{aligned} \tag{4.25}$$

If the grid boundary nodes do not move, that is if $u_g = v_g = 0$, then $\mathbf{G} = 0$, $\mathbf{F}_x^* = \mathbf{F}_x$, $\mathbf{F}_y^* = \mathbf{F}_y$, $\mathbf{A}^* = \partial \mathbf{F}_x / \partial \mathbf{Q}$, and $\mathbf{B}^* = \partial \mathbf{F}_y / \partial \mathbf{Q}$ and the model reduces to a standard fixed-grid finite element formulation as it should.

Petrov-Galerkin Test Function

The particular finite element test function employed here follows closely that first given by Berger (1992) applied to the shallow water equations modified to account for bed curvature effects and by Berger (1993) and Berger and Stockstill (1993) for application to advection dominated flows. Each of these studies were directed toward fixed grid formulations of the shallow water equations. The fixed grid formulation is appropriate for modeling bounded flows in channels having vertical sidewalls. Their findings show that the test function which is weighted upstream along characteristics provides the numerical dissipation needed to reduce the short wavelength oscillations associated with advection dominated flow. It is well known that short wavelength oscillations are a result of discretization. Fourier components of the equations can be composed of all wavelengths as a result of boundary conditions

and computer round-off (Pinder and Gray 1977). Wavelengths shorter than two times the grid spacing can not be resolved and are aliased into longer wavelengths (Abbott 1979). This results in spurious oscillations if no numerical dissipation mechanism is applied. The basic idea of Berger's method is to apply diffusion as a result of flow parameters. The scheme is a form of the Streamline Upwind Petrov-Galerkin (SUPG) method of Hughes and Brooks (1982). Stockstill and Berger (1994) have applied this finite element model to various rectangular high-velocity channel configurations. However, the present work extends Berger's test function to account for moving grid effects so that flow in trapezoidal high-velocity channels can be simulated.

The Petrov-Galerkin part of the test function, ϕ_i , is defined (Berger 1993, and Berger and Stockstill 1993) as

$$\phi_i = \beta \left(\Delta x \frac{\partial \phi_i}{\partial x} \hat{\mathbf{A}} + \Delta y \frac{\partial \phi_i}{\partial y} \hat{\mathbf{B}} \right) \quad (4.26)$$

where β is a dimensionless number between 0 and 0.5, and ϕ is the linear basis function. This part of the test function serves to dissipate spurious oscillations at short wavelengths attributed to advection dominated flows. The coefficient β is a dissipation parameter. Larger values of β result in large dissipation of the short wavelength components which provides stability, yet small values of β produce more accurate results (Berger 1993). In 4.26 Δx and Δy are representative elemental dimensions having units of length. Following the relation given by Katopodes (1984) the elemental lengths are chosen as

$$\Delta x = 2 \sqrt{\left(\frac{\partial x}{\partial \xi}\right)^2 + \left(\frac{\partial x}{\partial \eta}\right)^2} \quad (4.27)$$

and

$$\Delta y = 2 \sqrt{\left(\frac{\partial y}{\partial \xi}\right)^2 + \left(\frac{\partial y}{\partial \eta}\right)^2} \quad (4.28)$$

where ξ and η are the local coordinates defined from -1 to 1 (see figure 4.2).

$\hat{\mathbf{A}}$ and $\hat{\mathbf{B}}$ are computed in the following manner. Beginning with the definition of the convection matrices \mathbf{A}^* and \mathbf{B}^* (4.17 and 4.18, respectively), the characteristic matrices can be rewritten as

$$\mathbf{P}^{-1} \Lambda_x \mathbf{P} = \mathbf{A}^* \quad (4.29)$$

and

$$\mathbf{T}^{-1} \Lambda_y \mathbf{T} = \mathbf{B}^* \quad (4.30)$$

where $\Lambda_x = \mathbf{I}\lambda$ and $\Lambda_y = \mathbf{I}\gamma$ are the matrices of the eigenvalues of \mathbf{A}^* and \mathbf{B}^* , respectively. The matrices \mathbf{P} and \mathbf{P}^{-1} consist of the right and left eigenvectors of \mathbf{A}^* and \mathbf{T} and \mathbf{T}^{-1} are made up of the right and left eigenvectors of \mathbf{B}^* . Then $\hat{\mathbf{A}}$ and $\hat{\mathbf{B}}$ are defined as

$$\hat{\mathbf{A}} \equiv \mathbf{P}^{-1} \hat{\Lambda}_x \mathbf{P} \quad (4.31)$$

and

$$\hat{\mathbf{B}} \equiv \mathbf{T}^{-1} \hat{\Lambda}_y \mathbf{T} \quad (4.32)$$

where

$$\mathbf{P}^{-1} = \frac{1}{2c} \begin{bmatrix} 0 & 1 & -1 \\ 0 & (u+c) & -(u-c) \\ 1 & v & -v \end{bmatrix} \quad (4.33)$$

$$\hat{\Lambda}_x = \begin{bmatrix} \frac{\lambda_1}{\sqrt{\lambda_1^2 + \gamma_1^2}} & 0 & 0 \\ 0 & \frac{\lambda_2}{\sqrt{\lambda_2^2 + \gamma_1^2}} & 0 \\ 0 & 0 & \frac{\lambda_3}{\sqrt{\lambda_3^2 + \gamma_1^2}} \end{bmatrix} \quad (4.34)$$

$$\mathbf{P} = \begin{bmatrix} -v & 0 & 1 \\ -(u-c) & 1 & 0 \\ -(u+c) & 1 & 0 \end{bmatrix} \quad (4.35)$$

$$\mathbf{T}^{-1} = \frac{1}{2c} \begin{bmatrix} 0 & 1 & -1 \\ 1 & u & -u \\ 0 & (v+c) & -(v-c) \end{bmatrix} \quad (4.36)$$

$$\hat{\Lambda}_y = \begin{bmatrix} \frac{\gamma_1}{\sqrt{\gamma_1^2 + \lambda_1^2}} & 0 & 0 \\ 0 & \frac{\gamma_2}{\sqrt{\gamma_2^2 + \lambda_1^2}} & 0 \\ 0 & 0 & \frac{\gamma_3}{\sqrt{\gamma_3^2 + \lambda_1^2}} \end{bmatrix} \quad (4.37)$$

and

$$\mathbf{T} = \begin{bmatrix} -u & 1 & 0 \\ -(v-c) & 0 & 1 \\ -(v+c) & 0 & 1 \end{bmatrix}. \quad (4.38)$$

Here,

$$\lambda_1 = u - u_g$$

$$\lambda_2 = (u - u_g) + c$$

$$\lambda_3 = (u - u_g) - c$$

$$\gamma_1 = v - v_g$$

$$\gamma_2 = (v - v_g) + c$$

$$\gamma_3 = (v - v_g) - c$$

and $c = (gh)^{1/2}.$

The test function employed here, ψ_i , has two parts, a Galerkin portion in which the test function, ϕ_i , is identical to the basis function used, and a Petrov-Galerkin portion, φ_i , which is added to provide the numerical stability required in modeling

high-velocity flows containing shocks such as oblique standing waves and hydraulic jumps.

Temporal Derivatives

The semidiscrete model given in 4.25 is an unsteady form of the governing equations. Steady state solutions are obtained by marching the solution in time until convergence is obtained. Use of this time dependent approach requires discretization of the temporal derivatives of 4.25. Here a finite difference expression is used for the temporal derivatives. The expression for the temporal derivative of the variable vector, \mathbf{Q}_j , is

$$\left(\frac{\partial \mathbf{Q}_j}{\partial \tau} \right)^{m+1} \approx \alpha \left(\frac{\mathbf{Q}_j^{m+1} - \mathbf{Q}_j^m}{\tau^{m+1} - \tau^m} \right) + (1-\alpha) \left(\frac{\mathbf{Q}_j^m - \mathbf{Q}_j^{m-1}}{\tau^m - \tau^{m-1}} \right) \quad (4.39)$$

where j is the nodal location and m is the time step. An α equal to 1 results in a first order backward difference approximation and an α equal to 3/2 results in a second order backward difference approximation of the temporal derivative. The simulations conducted here are all for steady state solutions, therefore an $\alpha = 1$ is used exclusively because time accuracy is irrelevant. This eliminates the second term in the temporal derivative (i.e. only two time levels of information are used) thus reducing the computational effort.

Boundary Conditions

The number of required boundary conditions can be determined by examining the characteristics of the governing equations. Verboom et al. (1982) and Drolet and Gray (1988) show from the theory of characteristics that the number of boundary

conditions required is equal to the number of characteristic half planes exterior to the domain entering the domain. Two families of characteristics exist for the shallow water equations. The first family is a cone having a radius equal to the time-wave celerity product, $t(gh)^{1/2}$. This family corresponds to the concentric rings on the water surface resulting from a small disturbance. The second family corresponding to advection is the plane centered on the axis of the cone. The characteristics are paths on which information about the flow variables travels. Imposition of a boundary prevents information from traveling in the same manner as it would in the absence of the boundary. Information which originates within the domain is known by the model and therefore requires no additional effort. However, information which originates outside the domain must be provided to the model as boundary conditions. The required number of boundary conditions for the inflow, outflow, and sidewall boundaries is shown in table 4.1. The term V_n is the outward normal component of fluid velocity.

Open Boundaries

The boundary conditions specified at inflow boundary nodes for subcritical inflow are u and v or p and q . Supercritical inflow boundary nodes require specification of u , v , and h or p , q , and h . The tailwater is specified as the only boundary condition for subcritical outflow by setting the depth at each outflow boundary node. No boundary conditions are specified for supercritical outflow.

Side Boundaries

A no flux boundary condition is specified for sidewall boundaries. The weak

Table 4.1: Number of boundary conditions required.

Type of Boundary	Flow Regime	
	Subcritical $u^2 + v^2 \leq gh$	Supercritical $u^2 + v^2 > gh$
Inflow ($V_n < 0$)	2	3
Outflow ($V_n > 0$)	1	0
Sidewall ($V_n = 0$)	1	1

form of the governing equations includes line integrals around the boundaries (see 4.12 and 4.13). These integrals which consist of flux terms are the system's natural boundary conditions. Natural boundary conditions are applied to all moving boundaries and any fixed (vertical) sidewall boundaries. These boundaries are no flux boundaries in that there is no net flux of mass or momentum through them. This boundary condition is enforced in a weighted average sense through the weak statement. Mass flux through the boundary (Γ) is set to zero

$$\oint_{\Gamma} (p^* n_x + q^* n_y) d\Gamma = 0 \quad (4.40)$$

where $p^* = p - u_g h$ and $q^* = q - v_g h$. Also, there is no net momentum flux through the

side boundaries, therefore

$$\oint_{\Gamma} \left[(up^*)n_x + (uq^*)n_y \right] d\Gamma = 0 \quad (4.41)$$

and

$$\oint_{\Gamma} \left[(vp^*)n_x + (vq^*)n_y \right] d\Gamma = 0 . \quad (4.42)$$

Sidewall boundary stresses are modeled in a manner agreeable with the purpose of the work developed here. The purpose is to provide a tool for evaluation of flood control channels in which determination of the flow depth is of primary importance. Because applying the no slip condition (i.e. zero velocity) at the sidewalls requires significantly greater grid resolution than is required for accurate solution of the flow depth, sidewall drag is treated as a partial slip condition by approximating the boundary stress terms in the governing equations (integrated along the sidewall) by the Manning friction loss relationship

$$- \int_{\Gamma} \phi_i (h\sigma_{xx}n_x + h\sigma_{xy}n_y) d\Gamma = \int_{\Gamma} \phi_i gp \frac{n^2 \sqrt{p^2 + q^2}}{C_0^2 h^{4/3}} d\Gamma \quad (4.43)$$

and

$$- \int_{\Gamma} \phi_i (h\sigma_{yx}n_x + h\sigma_{yy}n_y) d\Gamma = \int_{\Gamma} \phi_i gq \frac{n^2}{C_0^2} \frac{\sqrt{p^2 + q^2}}{h^{4/3}} . \quad (4.44)$$

Therefore,

$$\oint_{\Gamma} \phi_i (F_x^* n_x + F_y^* n_y) d\Gamma = \oint_{\Gamma} \phi_i \begin{bmatrix} 0 \\ \left(\frac{1}{2}gh^2\right)n_x + gp \frac{n^2}{C_0^2} \frac{\sqrt{p^2 + q^2}}{h^{4/3}} \\ \left(\frac{1}{2}gh^2\right)n_y + gq \frac{n^2}{C_0^2} \frac{\sqrt{p^2 + q^2}}{h^{4/3}} \end{bmatrix} d\Gamma . \quad (4.45)$$

The partial slip condition allows velocities at the sidewalls. If the depth of flow at these boundaries is set equal to zero as it exists in the real system, there are singularities (i.e. division by zero) in the F_x^* , F_y^* , and H vectors. To avoid this problem, depths at the side boundaries are set to a small constant value, \hat{h} . These side boundary depths can be set to less than five percent of the centerline depth in a trapezoidal channel as demonstrated in Chapter 6 (see figure 6.6). This introduces error, but if the specified depth at the boundary is sufficiently small, this error will not significantly affect the results.

The flow velocity and grid velocity at a moving boundary are related by

$$(\mathbf{V} - \mathbf{V}_g) \cdot \hat{\mathbf{n}} = 0 \quad (4.46)$$

where $\hat{\mathbf{n}}$ is the unit vector outward normal to the moving boundary. The boundary

conditions at the moving boundary are

$$h(\tau^{m+1})_j = \hat{h} \quad (4.47)$$

and

$$(\mathbf{V}_g)_j = \alpha \left(\frac{\mathbf{X}(\tau^{m+1})_j - \mathbf{X}(\tau^m)_j}{\tau^{m+1} - \tau^m} \right) + (1-\alpha) \left(\frac{\mathbf{X}(\tau^m)_j - \mathbf{X}(\tau^{m-1})_j}{\tau^m - \tau^{m-1}} \right) \quad (4.48)$$

where j is the node location and \mathbf{X} is the spatial coordinate vector. The time step discretization of the grid velocity is identical to that used to approximate $\partial \mathbf{Q} / \partial \tau$.

Through enforcement of the natural boundary conditions (equations 4.40, 4.41, and 4.42) and the relationship of fluid and grid velocities (equation 4.46), the boundary locations (waterlines) are calculated. These boundary conditions require no net mass or momentum to pass in or out of these side boundaries of height \hat{h} at the waterline. The no flux boundary conditions are also applied to the vertical sidewall boundaries of rectangular channel reaches. Because these boundaries do not move, rectangular channel reaches are modeled using a fixed grid in which $\mathbf{V}_g = 0$.

As formulated above, there are potentially four degrees of freedom at each node: h_j , p_j , q_j , and s_j , where s_j is the magnitude of displacement of node j in the direction $\hat{\theta}$ which is here taken as the direction of maximum side slope. In the flow field the grid does not move and so p , q , and h are the unknowns. However, a side boundary on a sloping sidewall is a moving boundary, but the depth of flow on this boundary is constant over time ($h = \hat{h}$) and is specified. Rather than calculating h at this moving boundary, the boundary location and the boundary velocity must be

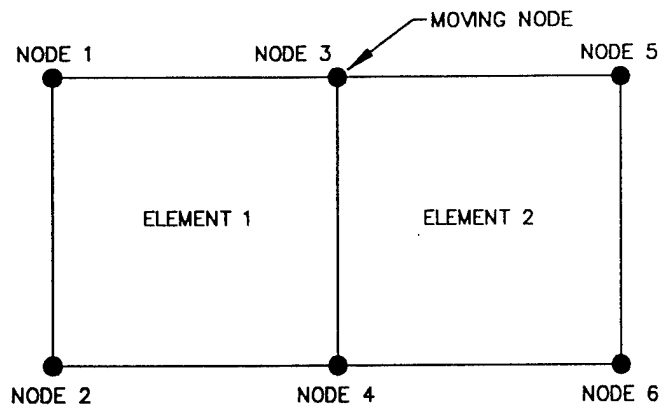
calculated. The three degrees of freedom on the moving boundaries are p , q , and s . For moving boundary nodes, a solution is sought for p_j , q_j , and s_j ; whereas, the variables to be solved for the fixed grid nodes are p_j , q_j , and h_j .

The selection of boundary flow depth values (\hat{h}) is problem dependent. The choice of an appropriate depth at the moving waterline is influenced by the scale of the flow field simulated. Choosing \hat{h} as a percentage of the centerline depth given for uniform flow is a logical nondimensional approach for trapezoidal channels. This method is used in the simulations reported in Chapters 5 and 6.

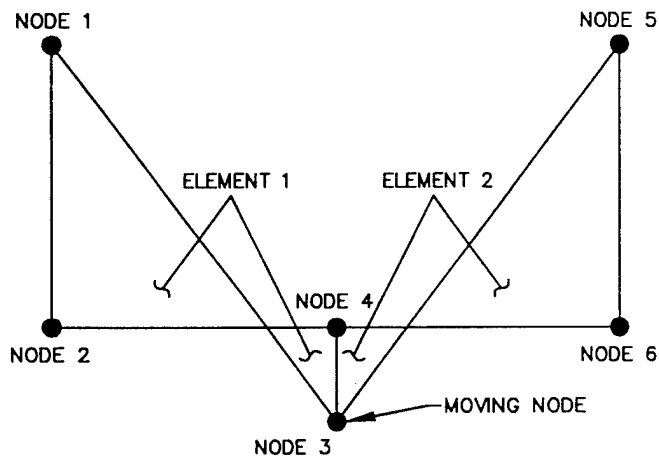
Movement of Interior Nodes

The boundary conditions associated with the moving boundary nodes are sufficient for describing boundary motion. In summary, these boundary conditions are that there is no net flux of mass or momentum through the moving boundary and that the depth at the moving boundary is a constant. However, large displacements of the moving boundary nodes can lead to element shape distortions. Excessive outward displacement results in elements adjacent to the boundary having unacceptable aspect ratios; whereas, inward movement can lead to element "folding" (Baines 1994) where nodes move across element lines producing ill formed elements as shown in figure 4.3.

This problem can be overcome by manually restructuring the computational mesh every few time steps and interpolating from the results of the last time step. This is quite laborious and therefore an automatic regridding method was developed whereby the interior nodes lying on the side slopes are moved each time step as a function of boundary nodal displacement. Interior side slope nodes are moved along



a. Adjacent elements prior to nodal displacement (time step m)



b. Ill formed elements resulting from excessive nodal displacement (time step $m+1$)

Figure 4.3. Schematic of element folding from excessive nodal displacement.

grid lines (element sides) with their displacements being related to their original relative positions across the side slope. For example, if a side slope is evenly divided into 4 elements between the waterline (where the exterior node is a moving boundary node) and the slope toe (where the interior node is a fixed node), then given the solution of the boundary node displacement for a time step, the interior side slope

nodes are repositioned at the quarter points across the side slope. MacKinnon and Carey (1993) successfully use a somewhat similar method in modeling thermal ablation and consolidation in porous media.

After new x and y coordinates are computed for the moving interior nodes, flow variables and the invert elevation for these nodes are recomputed using a linear interpolation from the previously computed grid. The grid velocities of these moving interior nodes are then computed as a displacement rate using 4.48 which is the same equation used for the boundary nodes.

The process of moving interior nodes lying on the side slopes as a function of moving boundary nodal displacement helps maintain good element aspect ratios and reduces element folding. By only allowing the nodes associated with the channel side slopes to move, the invert shape, in particular the side slope toe, is maintained.

Initial Conditions

Initial conditions are specified at the beginning of each simulation. These initial conditions include values of the flow variables and the location of the flow boundaries. Because these initial conditions are not the steady state solution of the two-dimensional equations, the moving finite element model of the shallow water equations is "time stepped" to steady state. This procedure facilitates the calculation of flow fields having standing waves and hydraulic jumps.

Initial conditions are related to uniform flow conditions. Given the discharge, cross section shape, roughness, and slope for each reach of the channel, the Manning's equation is used to compute normal depth and the cross sectionally averaged velocity

as though the channel were prismatic. The depth over each side slope is then computed from the cross sectional normal depth. The velocity computed from the Manning's equation is used as the initial velocity for straight channels, but this is cumbersome for geometrically complex channels because velocity in the two-dimensional model is a vector quantity. Computing the x- and y-component of velocity for channels composed of numerous reaches having various cross sectional and plan view shapes is tedious. Therefore, the initial conditions for complicated channel configurations are chosen as a motionless pool at normal depth for each reach. Initial depths and velocities are specified as those given for uniform flow for straight channels; whereas, uniform flow depths and zero velocity are given as initial conditions for geometrically complex channels.

Solution Procedure

The system of nonlinear equations is solved using the Newton-Raphson iterative method. Let \mathbf{R}_i be a vector of the nonlinear equations computed using an assumed value of \mathbf{L}_j where

$$\mathbf{L}_j = \begin{cases} \begin{Bmatrix} h_j \\ p_j \\ q_j \end{Bmatrix} & \text{if node } j \text{ is an interior node} \\ \begin{Bmatrix} s_j \\ p_j \\ q_j \end{Bmatrix} & \text{if node } j \text{ is a moving boundary node .} \end{cases} \quad (4.49)$$

\mathbf{R}_i is the residual error for a particular test function i . Subsequently, \mathbf{R}_i is forced toward zero as

$$\frac{\partial \mathbf{R}_i^k}{\partial \mathbf{L}_j^k} \Delta \mathbf{L}_j^k = -\mathbf{R}_i^k \quad (4.50)$$

where k is the iteration number, j the is node location, and $\partial \mathbf{R}_i^k / \partial \mathbf{L}_j^k$ is the Newton-Raphson Jacobian matrix. This linear system of equations is solved for $\Delta \mathbf{L}_j^k$ and then an improved estimate for \mathbf{L}_j^{k+1} is obtained as

$$\mathbf{L}_j^{k+1} = \mathbf{L}_j^k + \Delta \mathbf{L}_j^k. \quad (4.51)$$

This procedure is continued until convergence to an acceptable residual error is obtained.

The novel method for solving the depth, velocity, and domain of the flow field simultaneously as described above is used here. A simultaneous solution of the flow variables and the boundary displacement circumvents stability and convergence problems arising from the magnitudes of the nonlinear terms in the governing equations. The partial derivatives of the residuals with respect to the depth, $\partial \mathbf{R}_i^k / \partial h_j$, are evaluated for the fixed grid nodes, whereas, partial derivatives of the residuals with respect to the nodal displacement, $\partial \mathbf{R}_i^k / \partial s_j$, are evaluated for the moving nodes. All derivatives are determined analytically.

A contribution of this study is the determination of the Newton-Raphson Jacobian terms involving s_j which are presented in Appendix A.

The solution proceeds as follows for each time step:

- (I) Given the solution from the last time step or initial conditions, two time levels (m and $m+1$) of information is at hand for each node j :

$$h_j^{m+1}, p_j^{m+1}, q_j^{m+1}, x_j^{m+1}, y_j^{m+1}, (u_g)_j^{m+1}, (v_g)_j^{m+1}, h_j^m, p_j^m, q_j^m, x_j^m, \text{ and } y_j^m$$

(note for initial conditions, the variables at time level m are equal to those at time level $m+1$)

(II) Time Loop

(A) Update variables:

$$(1) \quad h_j^{m-1} = h_j^m \quad \text{then} \quad h_j^m = h_j^{m+1}$$

$$(2) \quad p_j^{m-1} = p_j^m \quad \text{then} \quad p_j^m = p_j^{m+1}$$

$$(3) \quad q_j^{m-1} = q_j^m \quad \text{then} \quad q_j^m = q_j^{m+1}$$

$$(4) \quad x_j^{m-1} = x_j^m \quad \text{then} \quad x_j^m = x_j^{m+1}$$

$$(5) \quad y_j^{m-1} = y_j^m \quad \text{then} \quad y_j^m = y_j^{m+1}$$

$$(6) \quad (u_g)_j^m = (u_g)_j^{m+1}$$

$$(7) \quad (v_g)_j^m = (v_g)_j^{m+1}$$

(B) Newton-Raphson Loop (the computed variables are the new values for time level $m+1$)

(1) Initialize the displacement of each node j :

$$\bullet \quad s_j = 0$$

(2) Compute \mathbf{R}_i^k

(3) Calculate the Jacobian $\partial \mathbf{R}_i^k / \partial \mathbf{L}_j^k$:

(a) If node is a moving boundary node, evaluate

$$\frac{\partial \mathbf{R}_1^k}{\partial s_j}, \quad \frac{\partial \mathbf{R}_1^k}{\partial p_j}, \quad \text{and} \quad \frac{\partial \mathbf{R}_1^k}{\partial q_j}.$$

(b) If the node is an interior node, evaluate

$$\frac{\partial \mathbf{R}_1^k}{\partial h_j}, \quad \frac{\partial \mathbf{R}_1^k}{\partial p_j}, \quad \text{and} \quad \frac{\partial \mathbf{R}_1^k}{\partial q_j}.$$

(4) Solve the linear system of equations, i.e. compute $\Delta \mathbf{L}_j^k$.

(a) If node is a moving boundary node, the results are

$$\Delta \mathbf{L}_j = \begin{Bmatrix} \Delta s_j \\ \Delta p_j \\ \Delta q_j \end{Bmatrix}$$

(b) If the node is an interior node, the results are

$$\Delta \mathbf{L}_j = \begin{Bmatrix} \Delta h_j \\ \Delta p_j \\ \Delta q_j \end{Bmatrix}$$

(5) Update the variables at each node j :

(a) If node j is a moving node, then:

(i) $s_j^{k+1} = \Delta s_j^k$ (note s_j^k is initialized to zero at the beginning of each iteration)

(ii) $p_j^{k+1} = p_j^k + \Delta p_j^k$

(iii) $q_j^{k+1} = q_j^k + \Delta q_j^k$

(iv) $x_j^{k+1} = x_j^k + s_j^{k+1} \theta_{xj}$

(v) $y_j^{k+1} = y_j^k + s_j^{k+1} \theta_{yj}$

(vi) $z_j^{k+1} = z_j^k + s_j^{k+1} (dz_0/ds)_j$

(vii) $(u_g)_j^{k+1} = (dx/d\tau)_j^{k+1}$ (see equation 4.48)

(viii) $(v_g)_j^{k+1} = (dy/d\tau)_j^{k+1}$ (see equation 4.48)

where $(dz_0/ds)_j$ is the side slope in direction

of $\hat{\theta} = (\theta_x, \theta_y)$ at node j .

(b) If node j is a fixed node, then:

(i) $h_j^{k+1} = h_j^k + \Delta h_j^k$.

(ii) $p_j^{k+1} = p_j^k + \Delta p_j^k$

(iii) $q_j^{k+1} = q_j^k + \Delta q_j^k$

(6) Evaluate residual error using the max-norm of change in Froude number from the last iteration (see discussion following this solution procedure outline).

$$\text{residual error} = \max_i \left| \frac{Fr_i^{k+1} - Fr_i^k}{Fr_i^k} \right| \text{ for each } i.$$

where

$$Fr_i^{k+1} = \sqrt{\frac{(p_i^{k+1})^2 + (q_i^{k+1})^2}{g(h_i^{k+1})^3}}$$

$$Fr_i^k = \sqrt{\frac{(p_i^k)^2 + (q_i^k)^2}{g(h_i^k)^3}}$$

and i is the node location.

- (a) If the nondimensional residual error is greater than a specified tolerance (generally of the order 10^{-3}) then return to step (IIB1).
- (b) If the nondimensional residual error is acceptable, then move the interior nodes
 - (i) move interior nodes on the side slope along an element side in proportion to their distance from the associated moving boundary node
 - (ii) linearly interpolate the bed elevation at the new node position
 - (iii) linearly interpolate values of h_j , p_j , and q_j from values computed during step (IIB5)
 - (iv) compute grid velocities of moving interior nodes

$$(u_g)_j^{k+1} = (dx/d\tau)_j^{k+1} \text{ (see equation 4.48)}$$

$$(v_g)_j^{k+1} = (dy/d\tau)_j^{k+1} \text{ (see equation 4.48)}$$

(III) Advance to the next time step, go to step (I).

The Froude number change is a nondimensional representation of the change in the values of the flow variables. This nondimensional representation avoids problems of scale dependence. The same convergence criterion is applied to both laboratory scale problems and prototype channels.

The coordinates of the moving nodes are updated every iteration and the Newton-Raphson Jacobian for the nodal displacement is derived accordingly (Appendix A). The movement of interior nodes depends on the displacement of the boundary nodes. However, inclusion of these effects within the Newton-Raphson scheme would significantly enlarge the coefficient matrix because several interior nodes depend on each moving boundary node. To avoid this, the interior nodes are moved once each time step. Therefore, inclusion of the effects of interior node movement within the Newton-Raphson procedure is not required.

CHAPTER 5

MODEL VALIDATION

This chapter provides the results of a test conducted to verify that the model is an accurate numerical approximation of the governing equations. It is important to check whether the discrete numerical model is actually solving the shallow water equations properly. This verification consists of comparing model results to an analytic solution of the shallow water equations. The particular geometric configuration chosen for this test is a horizontally curved, V-shaped channel of constant radius of curvature having side slopes of 1 vertical on 5 horizontal and no longitudinal slope. The mild side slopes were chosen to accentuate any boundary (i.e. waterline location) differences between the model and the analytical results.

Analytic Equations

An analytical solution of the shallow water equations written in cylindrical coordinates is determined assuming steady irrotational flow of an inviscid fluid having no radial component of velocity. The z-direction momentum equation,

$$\rho \left(\frac{u_{\omega}}{r} \frac{\partial u_z}{\partial \omega} + u_z \frac{\partial u_z}{\partial z} \right) = - \frac{\partial P}{\partial z} - \rho g \quad (5.1)$$

where

r = the radial distance

$u_{\omega} = u_{\omega}(r)$ = the ω -direction component of velocity

$u_z = u_z(r)$ = the vertical component of velocity

ρ = the fluid density

and

P = the pressure,

under the hydrostatic assumption reduces to

$$\frac{\partial P}{\partial z} = -\rho g . \quad (5.2)$$

Integrating and specifying zero pressure at the surface,

$$P(z) = \rho g(z_s - z) \quad (5.3)$$

where z_s is the water-surface elevation.

The r -direction momentum equation,

$$\rho \left(u_r \frac{\partial u_r}{\partial r} + \frac{u_\omega}{r} \frac{\partial u_r}{\partial \omega} - \frac{u_\omega^2}{r} + u_z \frac{\partial u_r}{\partial z} \right) = -\frac{\partial P}{\partial r} \quad (5.4)$$

where u_r is the radial component of velocity, reduces to

$$\frac{\partial P}{\partial r} = \rho \frac{u_\omega^2}{r} . \quad (5.5)$$

The Bernoulli equation is given as

$$\frac{P}{\rho g} + z + \frac{u_\omega^2}{2g} = C_1 \quad (5.6)$$

where C_1 is a constant. Differentiation of 5.6 with respect to r yields, for constant elevation z

$$\frac{\partial P}{\partial r} = - \rho u_{\omega} \frac{\partial u_{\omega}}{\partial r} . \quad (5.7)$$

Equating 5.5 and 5.7 and integrating provides the velocity distribution function which is identical to that of a free vortex,

$$u_{\omega} = \frac{C_2}{r} \quad (5.8)$$

where C_2 is a constant.

The water-surface gradient found by substituting 5.3 into 5.5, differentiating with respect to r , and then including 5.8 is given as

$$\frac{\partial z_s}{\partial r} = \frac{u_{\omega}^2}{gr} = \frac{C_2^2}{gr^3} . \quad (5.9)$$

Test Conditions

The normal depth concept is not applicable to ideal flow in a channel having no longitudinal slope. Therefore, initial conditions for this test were arbitrarily selected. The centerline radius and depth were chosen to be 500.0 ft and 5.0 ft, respectively. Since the interest of this research is on modeling supercritical flow, the lowest local Froude number chosen was 1.0. The location of the lowest Froude number is at the channel centerline. Specifying a Froude number of 1.0 and depth of 5.0 ft results in a centerline velocity of 12.69 ft/sec. The channel side slopes were fixed at 1 vertical on 5 horizontal. With this information, the velocity distribution and depth variations across a section were computed. So as not to introduce vorticity into the flow field, these results were used as the inflow boundary conditions for the grid

nodes located at $\omega = 0$ degrees. The initial conditions for the remainder of the flow field were specified as a uniform velocity distribution and a level water surface. Inflow boundary and initial conditions used for the model verification are shown in figure 5.1. Flow at the outflow boundary was supercritical and therefore no outflow boundary condition was specified.

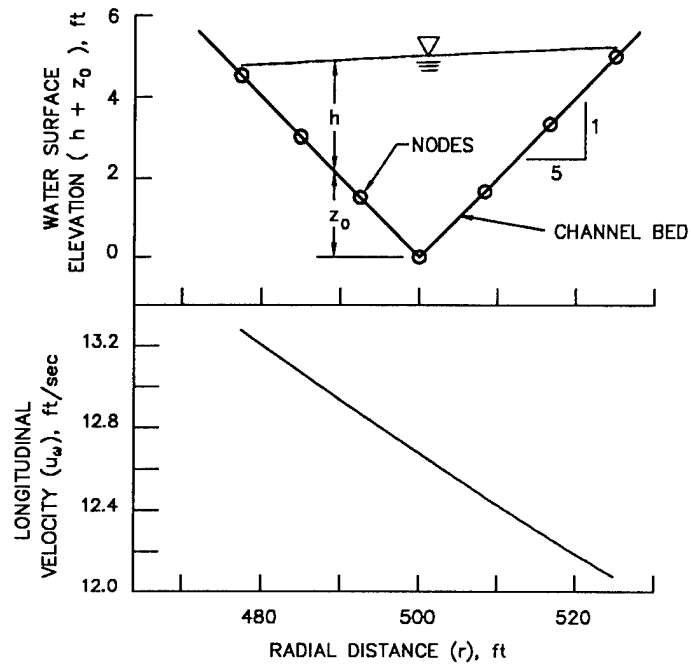
The model parameters used are presented in table 5.1. The boundary depth, \hat{h} , was chosen to be 5 percent of the centerline depth resulting in steady state local Froude numbers of 4.7 at the inside boundary and 4.3 at the outside boundary. This choice of \hat{h} resulted in an error of approximately 0.25 percent in cross sectional area. This error was deemed acceptable for model verification.

The curved channel was discretized into 6 elements in the radial direction and the length of the channel was divided into 207 elements such that the length-to-width ratio of each element was approximately 2. The numerical model computational mesh, shown in figure 5.2, had 1456 nodes and 1242 elements.

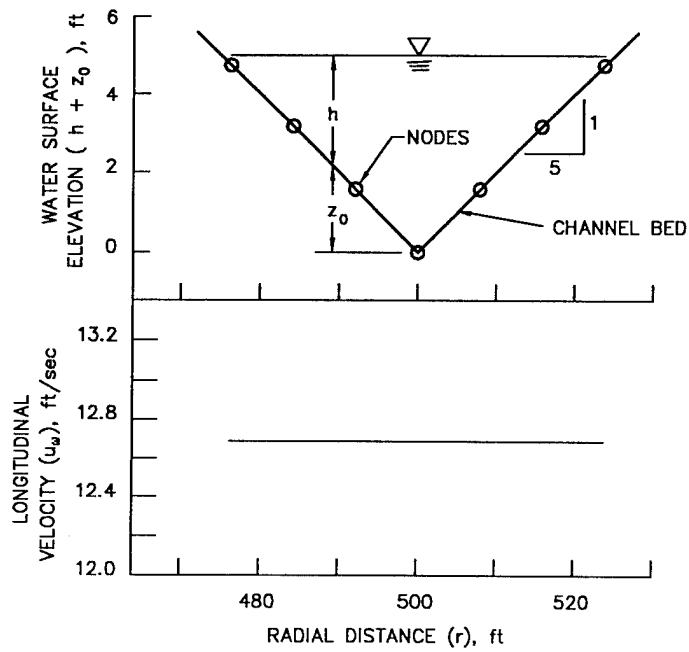
Initial time step selection was based on the Courant number defined as

$$Cr = \frac{\sqrt{u^2 + v^2} + \sqrt{gh}}{\frac{\ell_{\min}}{\Delta t}} \quad (5.10)$$

where ℓ_{\min} is the minimum grid spacing and Δt is the time step. The numerical stability constraint for many explicit models of hyperbolic partial differential equations is the Courant-Friedrichs-Lewy (CFL) condition (Anderson et al. 1984). The CFL



a. Inflow boundary conditions (nodes at $\omega = 0$ degrees)



b. Initial conditions (nodes at $0 \text{ degrees} < \omega < 360 \text{ degrees}$)

Figure 5.1. V-shaped channel boundary and initial conditions (exaggerated abscissa).

Table 5.1: V-shaped channel, model parameters.

Condition	Value
α	1.0
β	0.1
n	0
v	0
\hat{h}	0.25 ft

condition limits the time step size by restricting the Courant number to be less than or equal to 1.0. The model developed for this dissertation is fully implicit (equations 4.39 and 4.48) and is not subject to the CFL condition; however, experience in modeling rectangular high-velocity channels (Stockstill and Berger 1994) has shown that a time step corresponding to a Courant number near unity is a good choice for startup.

Simulations were conducted using a time step of 1.0 sec which resulted in Courant numbers of 1.1, 1.7, and 1.0 at the inside boundary, channel centerline, and outside boundary, respectively. The model converged to steady state in 250 sec.

Test Results

The analytic solution is compared to model results at the cross section located at an ω value of 180 degrees. The flow depths are compared with the analytic solution in figure 5.3. A comparison of the longitudinal velocity, u_ω , is shown in

figure 5.4. The largest velocity error, $(V_{\text{model}} - V_{\text{analytical}})/V_{\text{analytical}}$, was 0.148 percent at the first node outside the centerline node where the simulation velocity at this node was too high.

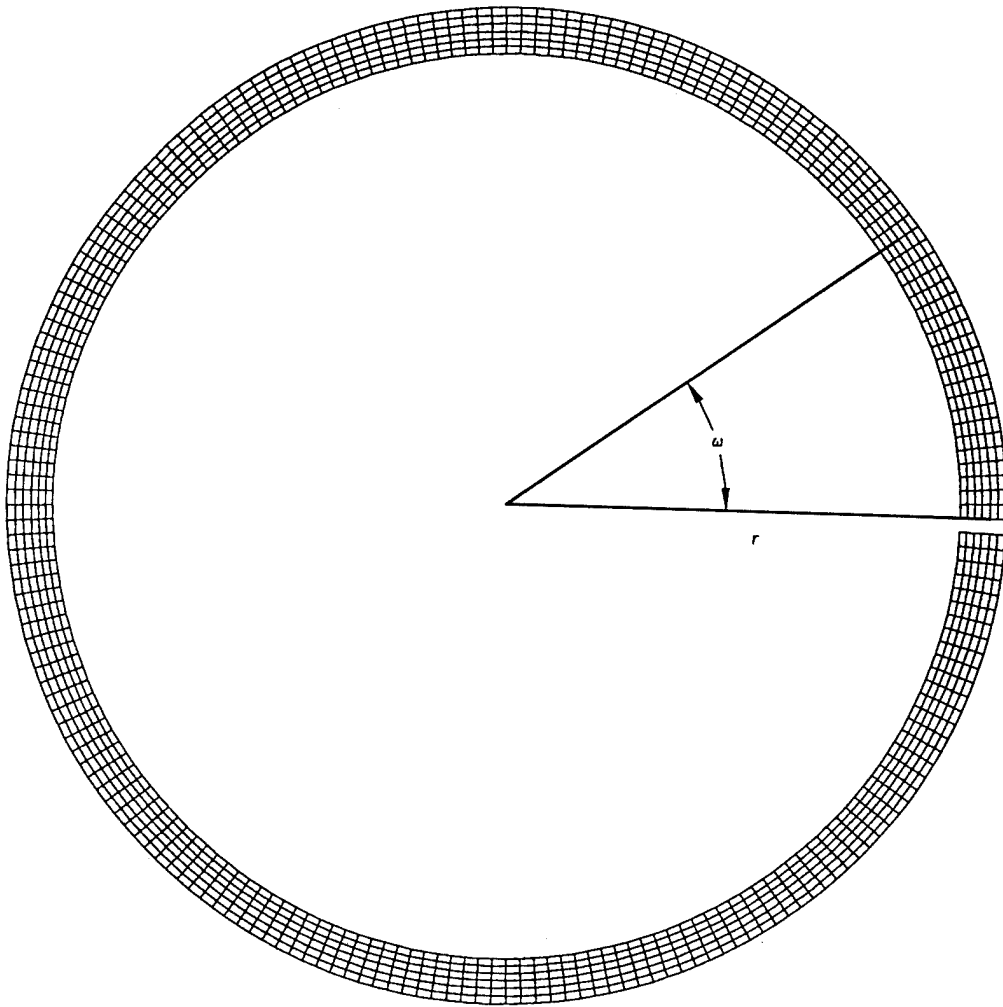


Figure 5.2. Numerical model computational mesh for V-shaped channel.

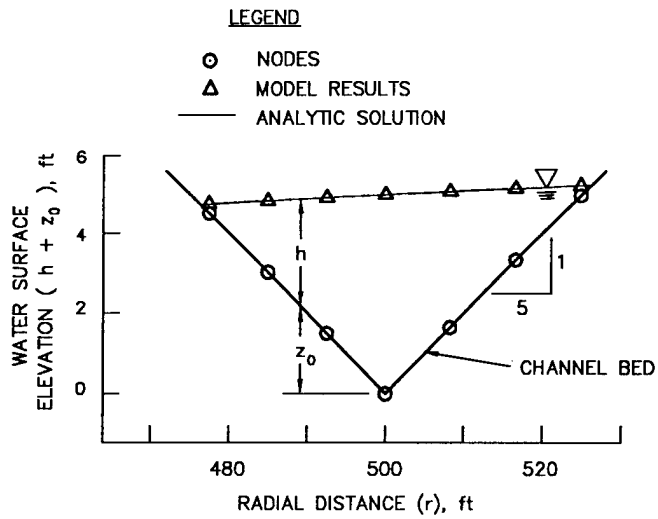


Figure 5.3. Analytical and model computed flow depths for V-shaped channel (exaggerated abscissa).

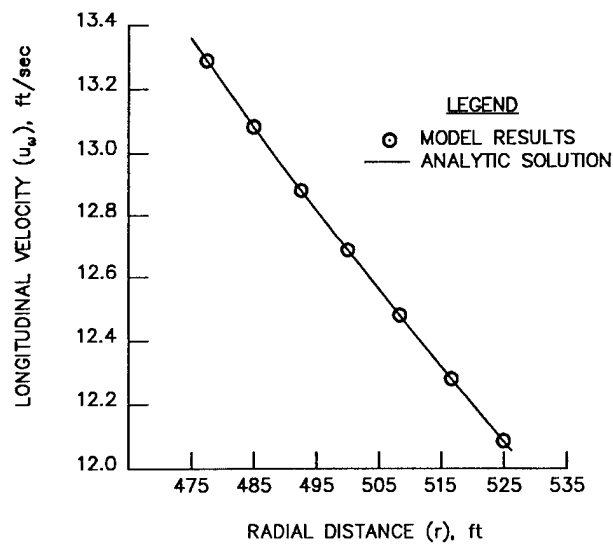


Figure 5.4. Analytical and model computed longitudinal velocity for V-shaped channel.

Since there are no energy losses throughout the flow field, the specific energy defined as

$$E = \frac{u_{\omega}^2}{2g} + h + z_0 \quad (5.11)$$

is a constant. Choosing the bed elevation, z_0 , as zero at the channel centerline, values of specific energy are presented in table 5.2. The error shown in table 5.2 is the ratio of the model results minus the analytic solution divided by the analytic solution. The largest error in the computed solution was 0.051 percent and is associated with the first node outside the centerline node. The volumetric flow rate computed by the model through the cross section at an ω value of 180 degrees differed from that specified at the inflow boundary by 0.039 percent. This continuity check demonstrates that the model conserves mass. These results show that the model is a numerical

Table 5.2: V-shaped channel, analytical solution and model computed specific energy.

Radial Distance, ft	Specific Energy, ft		Percent Error
	Analytic Solution	Model Results	
477.4667	7.5000	7.4980	-0.027
484.9626	7.5000	7.4990	-0.013
492.5042	7.5000	7.5027	0.036
500.0000	7.5000	7.4993	-0.009
508.2810	7.5000	7.5038	0.051
516.6127	7.5000	7.4989	-0.015
524.8941	7.5000	7.5030	0.040

representation of the ideal shallow water equations with moving boundaries. It is noted that these ideal equations exclude boundary friction and turbulence effects.

CHAPTER 6

MODEL TESTING

Additional model evaluations are made in this chapter by comparing model results with laboratory data. These evaluations are referred to as model testing in that tests were conducted to determine the shallow water model's ability to simulate real flows.

A series of flume tests were conducted at the U.S. Army Engineer Waterways Experiment Station, Hydraulics Laboratory. Four geometric configurations were tested. One flume consisted of a trapezoidal channel having a horizontal curve. Three flume tests were conducted using a trapezoidal channel constructed on a tilting platform. These tests documented the flow conditions at a trapezoidal-to-rectangular transition, a rectangular-to-trapezoidal transition, and flow obstructions geometrically similar to bridge piers.

The flow in each test was on average in the supercritical regime. The cross sectional average Froude number given as

$$Fr = \frac{\bar{V}}{\sqrt{gh_{\text{eff}}}} \quad (6.1)$$

was greater than unity. Here \bar{V} is the cross-sectional averaged velocity (discharge divided by cross-sectional flow area normal to the flow direction), and h_{eff} is the effective, or hydraulic depth (cross-sectional flow area normal to the flow direction divided by the free-surface width). However, local Froude numbers expressed in terms of local flow variables as

$$Fr_t = \frac{\sqrt{u^2 + v^2}}{\sqrt{gh}} \quad (6.2)$$

may be less than or greater than unity along the sloping sidewalls. The flow over the sloping sidewalls may be subcritical even though the cross section on average experiences supercritical flow.

Frequently the water-surface elevation in supercritical channels oscillates in time even under steady inflow boundary conditions. This is particularly prevalent in the vicinity of shocks such as oblique standing waves and hydraulic jumps. Water surface oscillations were observed in each of the flume tests conducted in this study. The flow in each test was only quasisteady in that flow depths and velocities varied about mean values. The data presented herein are approximate temporally averaged values.

Model testing described in this chapter was conducted in a progression of difficulty from a moving finite element modeling standpoint. The first comparison was with supercritical flow in a trapezoidal-to-rectangular transition. Although the first test was not a demanding test for the moving boundary scheme, it did show the model's ability to simulate oblique standing waves. The second test was a more general two-dimensional case of supercritical flow in a trapezoidal channel with a horizontal bend. The third test was of supercritical flow in a rectangular-to-trapezoidal transition and the fourth test was of subcritical and supercritical flow in a trapezoidal channel having multiple flow obstructions. The flow conditions in these last two tests included oblique standing waves in the trapezoidal channels.

The model parameters used in each of these tests were based solely on information known prior to model simulations. These parameters were never used as model calibration devices in that the model parameters were not adjusted to improve the simulation results' comparison with the observed laboratory data.

Trapezoidal-to-Rectangular Transition

Flume tests were conducted using a tilting open channel flume 80 ft long and 1 ft high with a base width of 2 ft and side slopes of 1 vertical on 2.25 horizontal (figure 6.1). The flume was constructed of plastic coated plywood covered with rolled epoxy paint. The range of tilt allowed the flume to be set on hydraulically steep

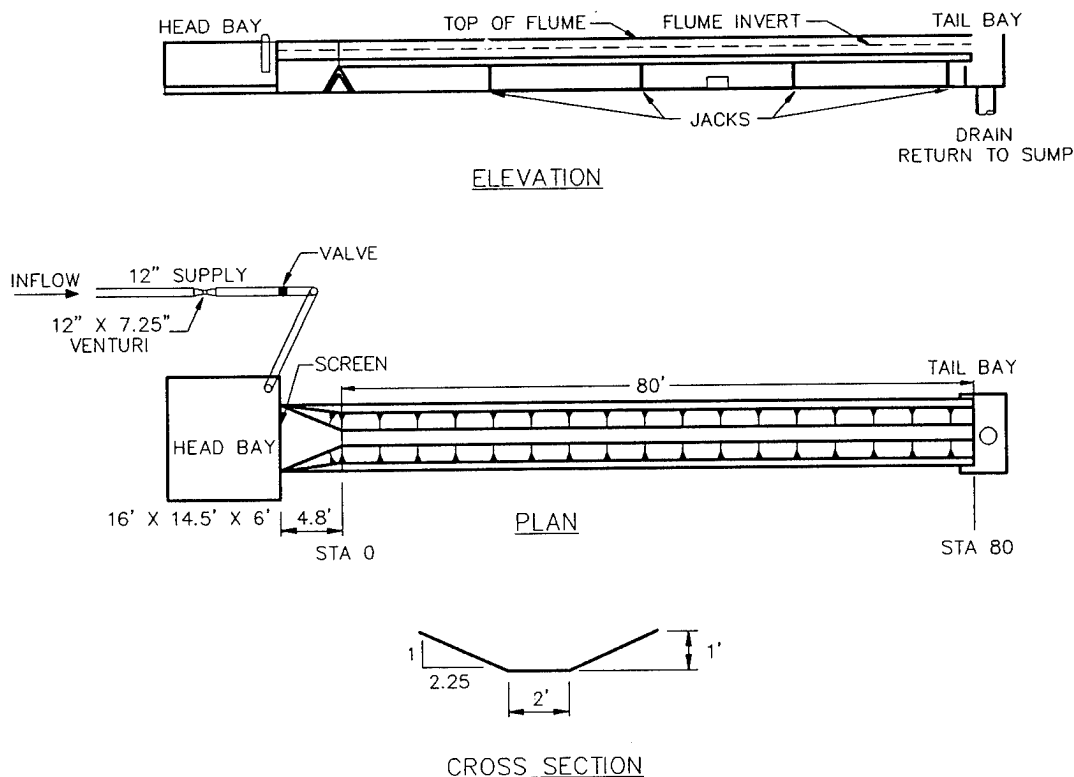


Figure 6.1. Plan and elevation views of tilting flume.

slopes which produced supercritical flow. Water was supplied to the flume by a circulating system. The water was pumped from a sump to a 12-inch supply pipe. The flume discharge was returned to the sump through a drain line. The discharge was measured using a factory calibrated 12-inch by 7.25-inch venturi meter installed in the supply line. This inflow was discharged into a headbox and baffled with a screen. Flow at the downstream end of the channel was supercritical. Boundary conditions should not be imposed at supercritical outflow boundaries (table 4.1); therefore, no tailgate was used.

Documentation of the flow conditions consisted of photographs and measured flow depths and velocities. Flow depths were measured using point gages with a limit of reading of 0.001 ft. Velocity measurements were made with a commercial propeller type flow meter mounted to permit measurement of current from any direction; the meter elevation was also adjustable. The 0.46-inch (outside diameter) measuring head of the velocity meter was constructed of a five bladed PVC rotor mounted on a stainless steel spindle. For the magnitude of velocities reported in this study, the manufacturer specification lists the probe accuracy as ± 0.05 ft/sec.

A trapezoidal-to-rectangular transition was built by placing vertical walls at the top of the side slopes starting 36.5 ft from the upstream end of the flume and ending at the side slope toe at sta 50. The transition rate was 1 lateral on 6 longitudinal. The flume was rectangular in cross section from sta 50 to the flume end (sta 80). A plan view of the trapezoidal-to-rectangular channel transition is shown in figure 6.2. Figure 6.3 is a dry bed photograph of this transition.

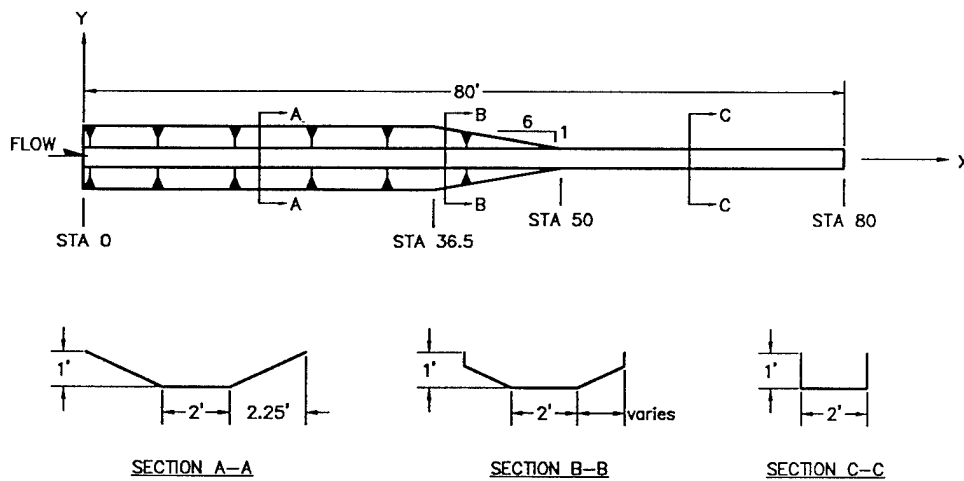


Figure 6.2. Plan view and sections of trapezoidal-to-rectangular transition.

Test Conditions

Model testing consisted of comparing flume data obtained with a discharge of $4.00 \text{ ft}^3/\text{sec}$ on a slope of 0.010 with simulation results. The test setup produced supercritical flow with an average Froude number approaching the transition (within the trapezoidal channel) of 2.0. This initial configuration was a simple test for the moving boundary model because the straight prismatic trapezoidal channel flow conditions were nearly uniform with smooth waterlines and flow boundaries were established by the vertical sidewalls, but only after the waterline intersected the vertical transition walls. However, as the supercritical flow over the sloping sidewalls intercepted the vertical transition walls, oblique standing waves were produced within the rectangular portion of the flume as shown in figure 6.4. These oblique positive waves were generated on each side of the channel and met at the channel centerline where the maximum local flow depth was produced. The standing waves were

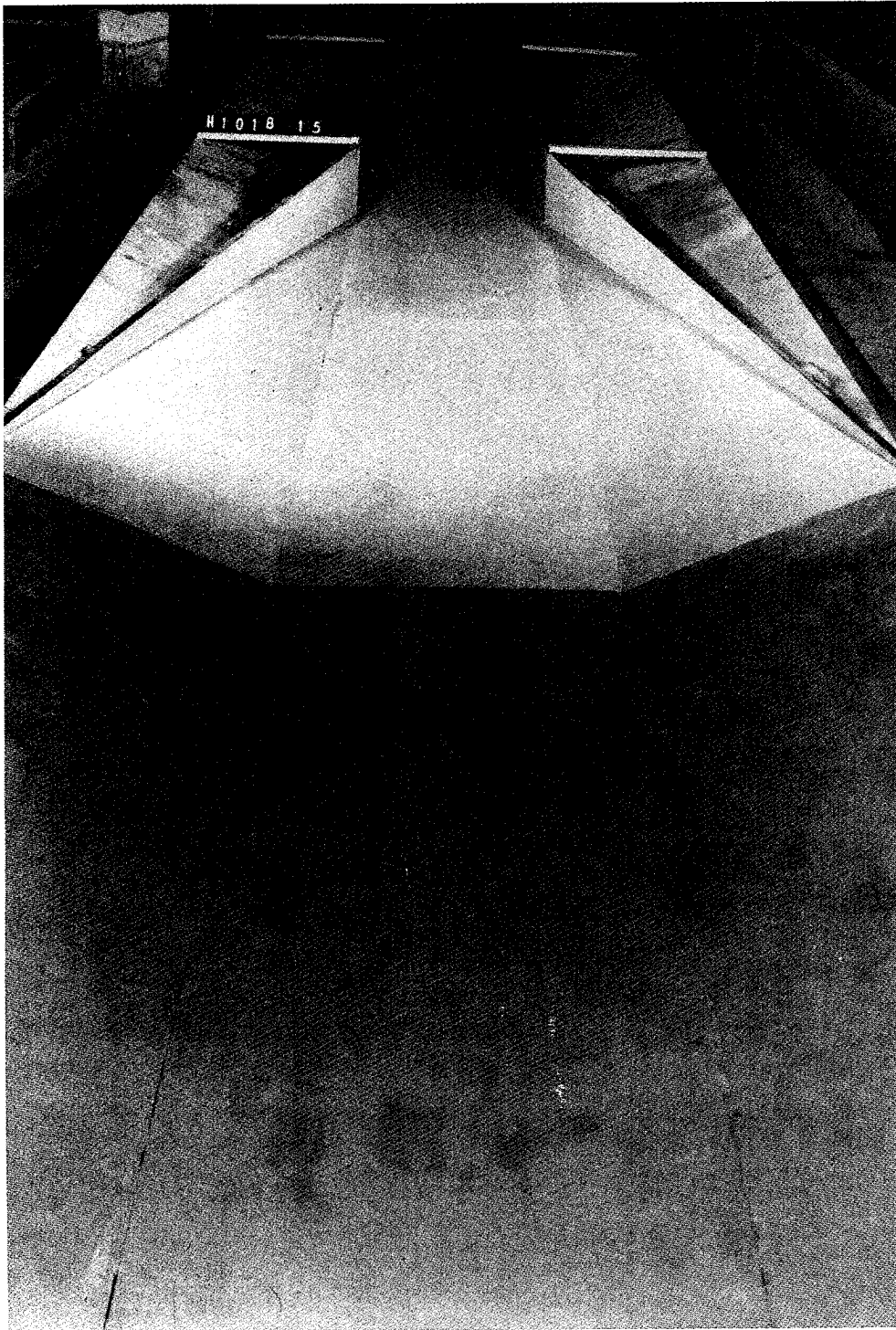


Figure 6.3. Dry bed view of trapezoidal-to-rectangular transition.

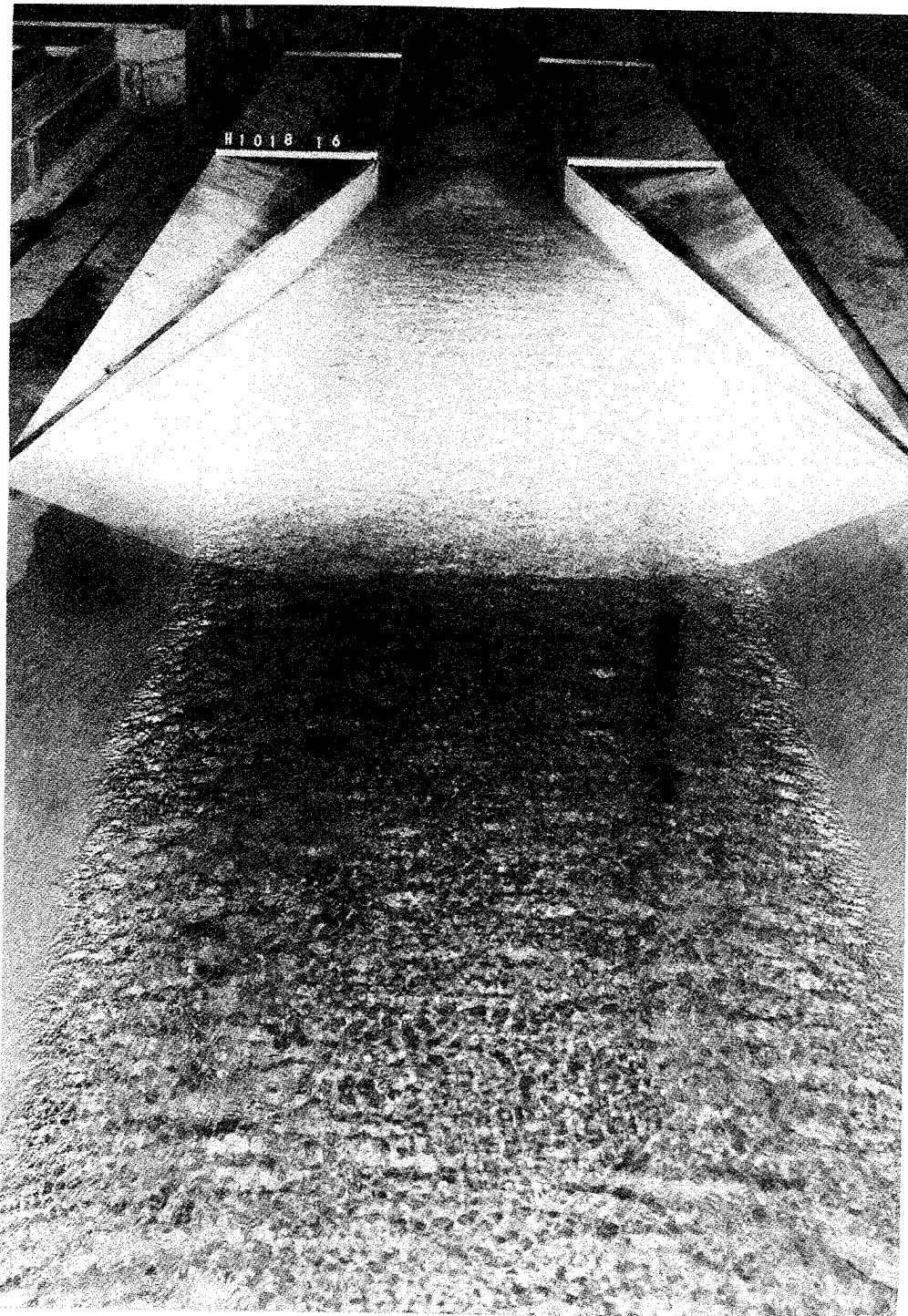
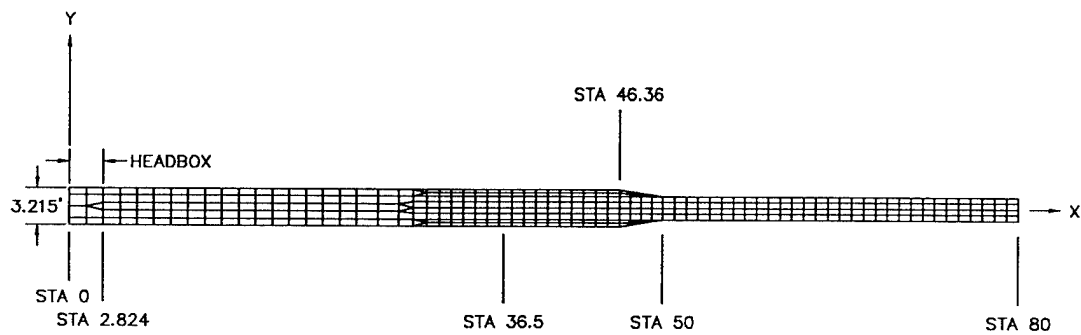


Figure 6.4. Flow conditions in trapezoidal-to-rectangular transition, approach Froude number = 2.0 (looking downstream).

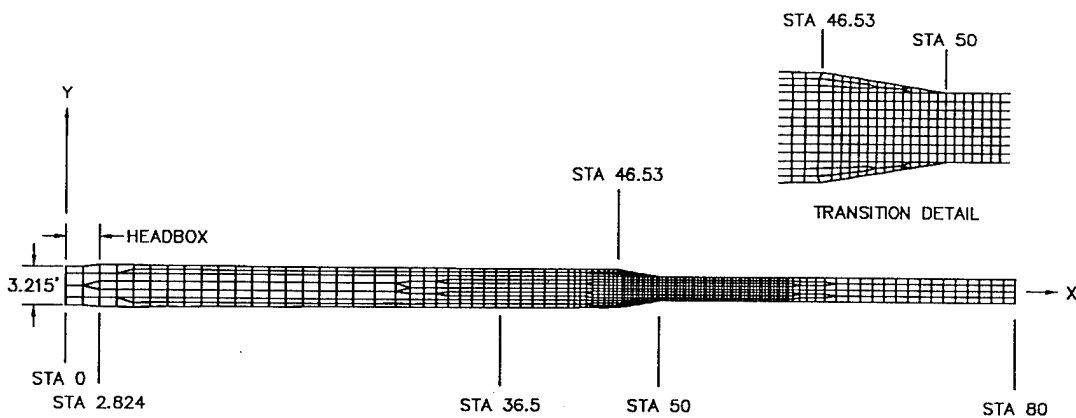
reflected from the sidewalls for quite some distance downstream of the transition. Although this first case was not a definitive test for the moving boundary scheme, it did show the model's ability to simulate oblique standing waves.

Initial mesh construction within the trapezoidal reach of the channel required an estimate of the top width of the flow so the location of the side boundaries could be established. In trapezoidal channels the top width is set by the flow depth, therefore an estimate of the flow depth was sought. A Manning's n value of 0.009 for the smooth boundaries of epoxy painted plywood was used to compute normal depth for the trapezoidal channel with a discharge of $4.00 \text{ ft}^3/\text{sec}$, a channel slope of 0.010, a base width of 2.0 ft, and 1 vertical on 2.25 horizontal side slopes. The top width of the initial grid was determined using the computed normal depth applied to this channel while accounting for the specified depth at the moving boundary, \hat{h} . The lateral horizontal distance from the side slope toe to the waterline was set equal to the difference in normal depth and the depth at the waterline divided by the side wall slope (1/2.25). The initial mesh had 458 nodes and 389 elements and is shown in figure 6.5. The initial grid contained 3 elements across the channel bottom at the upper end (headbox outlet, sta 2.82) and 4 elements across the bottom from upstream of the transition (sta 28.8) to the flume end (sta 80). Side slope resolution varied from one element at the upper end to 2 elements on each side slope in the vicinity of the transition beginning at sta 30.0. The upstream end of the mesh was composed of points used to simplify the boundary condition input. The nodes at the upstream end of the channel represented a 2.82 ft-long "headbox" in that the inflow cross section (at

sta 0.0) was of rectangular shape and the mesh was fixed at these boundaries. This "box" transitioned from rectangular to the actual flume shape over the box length of 2.82 ft. Some 44 ft upstream of the transition (waterline/vertical wall intersection) were modeled to minimize any entrance effects caused by the "headbox". A 30-ft



a. Initial mesh



b. Final mesh

Figure 6.5. Numerical model computational meshes for trapezoidal-to-rectangular transition.

long reach of the channel downstream of the transition was also included in the calculations.

The inflow boundary was supercritical and required the specification of p , q , and h at each inflow node. Since the computational mesh's x axis was made to lie on the flume centerline, q was set to zero and each value of p was determined as the total discharge divided by the width of the "headbox" (3.215 ft). Flow at the outflow boundary was supercritical in the rectangular channel and so no boundary conditions were specified. The boundary conditions used are presented in table 6.1 and the model parameters used are listed in table 6.2. The turbulent kinematic viscosity was computed (equation 4.5) using normal depth and velocity for the rectangular reach of

Table 6.1: Trapezoidal-to-rectangular transition, boundary conditions.

Boundary	Flow Regime	Boundary Condition	Value
Inflow	Supercritical	h	0.280 ft
		p	1.244 ft ² /sec
		q	0.0
Outflow	Supercritical	h	Not Specified
		p	Not Specified
		q	Not Specified

Table 6.2: Trapezoidal-to-rectangular transition, model parameters.

Condition	Value
α	1.0
β	0.1
n	0.009
C_b, v_t	0.1, 0.023 ft ² /sec
\hat{h}	0.01 ft

channel. This was the major area of interest concerning model evaluation because this portion of the channel contained the oblique standing waves generated at the transition. The chosen parameters were never adjusted to make the model results more closely match the laboratory data. The numerical model was never "calibrated" to replicate the observed quantities. The selected constant depth ($\hat{h} = 0.01$ ft) at the moving sidewall boundaries (figure 6.6), was less than 5 percent (3.6 percent) of the depth at the channel center and produced a cross sectional area error of approximately 0.03 percent at the inflow boundary. Sidewall boundaries within the trapezoidal portion of the channel were allowed to move in conjunction with the depth solution. All moving nodes were confined to move in the direction of maximum side slope with the exception of each sidewall boundary node at the vertical wall where the trapezoidal-to-rectangular transition begins. These nodes were only allowed to move in the direction

parallel to the transition walls. This allowed the waterline to move upstream or downstream as the solution depth increased and decreased, respectively. The remaining sidewall boundary nodes within the transition and all nodes within the rectangular portion of the channel were fixed.

Initial conditions for these simulations were the flow variables given for uniform flow in each of the two typical sections. That is, normal depth (0.28 ft) and velocity (5.41 ft/sec) for the trapezoidal reach were used as the initial conditions for the upstream reach (sta 0.0 to sta 46.36) and normal depth (0.34 ft) and velocity (5.95 ft/sec) for the rectangular reach were used as the initial conditions for the lower end of the flume (sta 50 to sta 80). Approximate mean values of the uniform conditions in the upper and lower reaches were used for the initial conditions within the transition. Given the initial and boundary conditions, simulations were conducted with the initial mesh (figure 6.5a) using time steps of 0.1 sec and 0.2 sec for a total time of 13 sec. A time step of 0.1 sec resulted in a Courant number of approximately 0.9 at the smallest grid element. Although the model is fully implicit, the computational runs described in this dissertation typically were started using time steps corresponding to Courant numbers near 1.0. After model startup the time steps were increased to speed up steady state convergence.

The computational mesh was refined at this point and the current values for the coarse mesh were interpolated to the refined mesh using a bilinear interpolation scheme which is identical to the basis functions used in the finite element model (equation 4.9). This process of refining the mesh and time marching to steady state

was continued three times (4 computational meshes, total) until refinement of the mesh did not alter the model results. This grid convergence sequence resulted in the final computational mesh shown in figure 6.5b. The final mesh had 1114 nodes and 1001 elements. The sidewall transverse resolution varied from 2 elements at the upstream end of the modeled reach to 3 elements in the vicinity of the transition beginning at sta 44.31. The bottom transverse resolution varied from 3 elements at the upper end, to 8 elements at the transition, to 4 elements at the lower end. A transverse-to-longitudinal aspect ratio of 1.0 was used for the elements within and downstream of the transition. A time step of 0.1 sec was used for the final grid. The primary difference in the flow solutions provided by the various grids was that peak flow depths in the oblique standing waves increased as the grid resolution increased. The increased grid resolution in this region also sharpened the standing wave patterns.

The evolution of the flow depth at the centerline node located at sta 50.0 is presented in figure 6.6. The length of simulation time for each of the four computational meshes is also shown on this figure. The time history plot illustrates the time stepping to steady state process at a point in the flow field. The depth at this point changed less than 10^{-5} ft after 60 sec.

Test Results

Comparisons are made between the water surface elevations measured in the flume and those obtained from the model simulations. Depths are reported relative to the channel bottom as illustrated in figure 6.7. Flow depths in the flume were measured at small enough intervals so that linear interpolations of the observed values

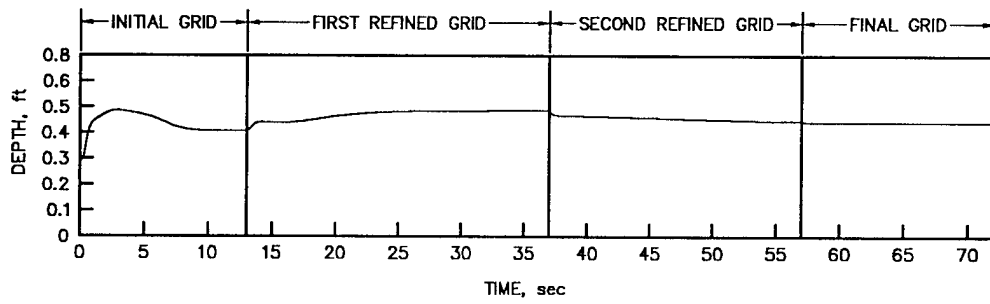


Figure 6.6. Time history of depth for trapezoidal-to-rectangular transition at centerline of sta 50.

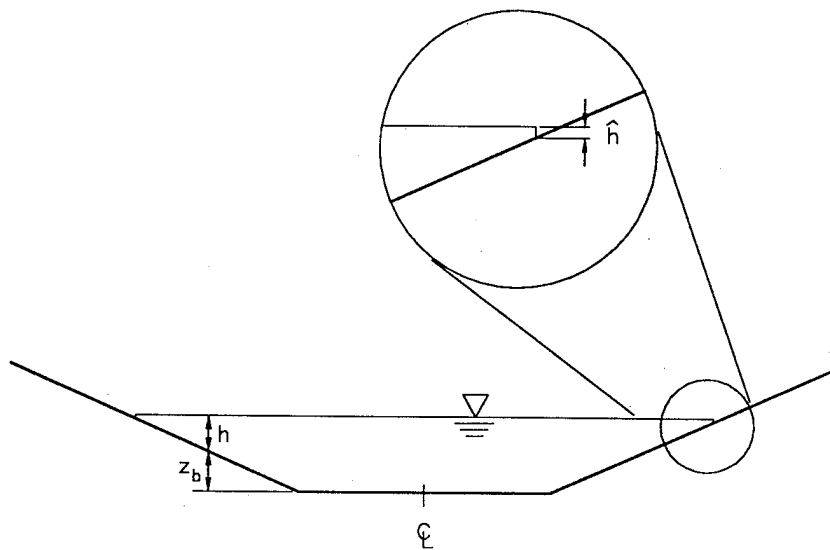


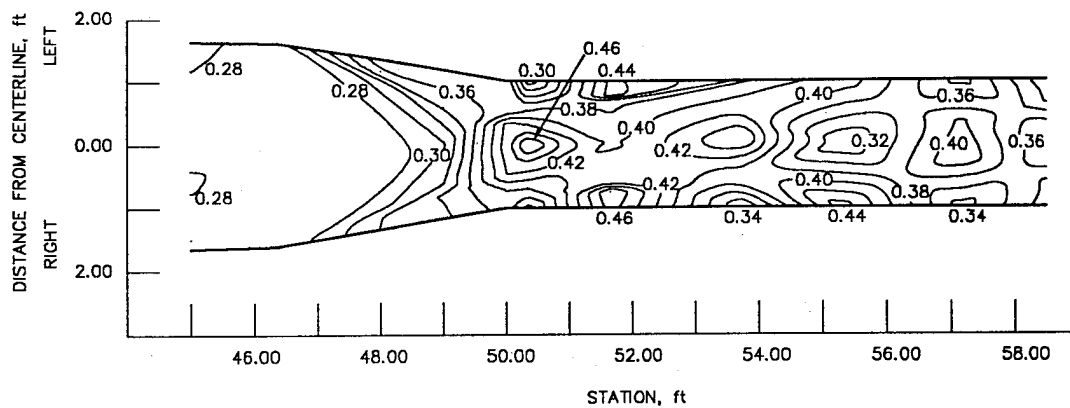
Figure 6.7. Definition sketch of depths plotted on depth contours.

provided an accurate map of the water surface. The spatial intervals of observation points varied from 2.5 ft longitudinally and 0.5 ft transversely upstream of the transition to as small as 0.35 ft longitudinally and 0.13 ft transversely within and downstream of the transition.

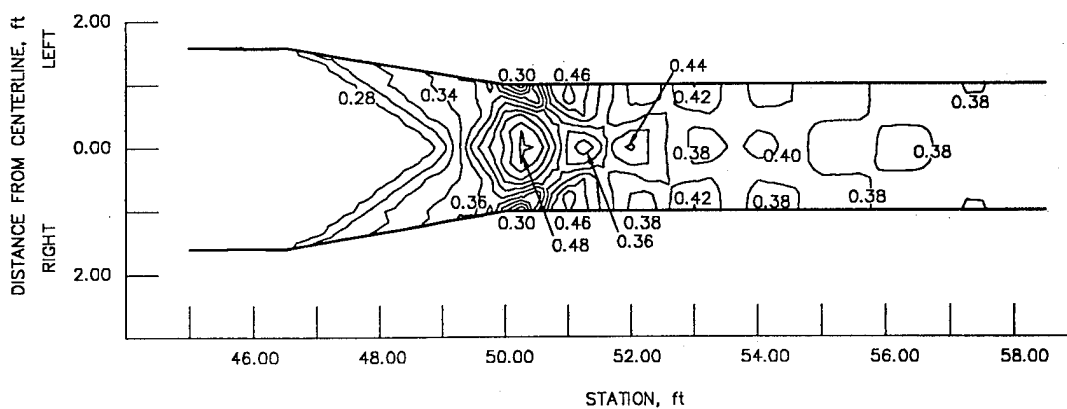
Contours of laboratory data and numerical model results were plotted using the FastTABS postprocessor (Brigham Young University 1993). The laboratory results were placed on an irregular grid whose grid points corresponded to the coordinates at which the data were measured. First a value at each grid cell center is obtained using a bilinear interpolation of the cell's nodal values. Next, values at the cell side midpoints are obtained by linear interpolation of the nodal values. The cell is then subdivided into a series of triangles with vertices at the element nodes, at each midpoint of the cell sides, and at the cell center point. The data are then linearly interpolated from the values at the vertices. Finally, contour lines are drawn at a user specified interval.

Contours of the observed and computed flow depths relative to the channel bottom ($h + z_b$ in figure 6.7) are presented in figure 6.8. Figure 6.9 is the computed water-surface mesh. Water-surface profiles along the left wall and centerline are provided in figure 6.10. These results show that the model adequately captures the magnitude of the highest oblique standing waves but does not accurately reproduce the wave phases. Wave height attenuation through the transition is abrupt in the shallow water model. Similar wave phase errors have been observed by others (Jimenez and Chaudhry 1988, Bhallamudi and Chaudhry 1992, Berger 1992, Hager et al. 1994, and

Berger and Stockstill 1994) in two-dimensional shallow water applications to supercritical flow in rectangular channels and by Ippen (1951) when his analytic model is compared with laboratory data. These wave phase errors are attributed to the hydrostatic pressure assumption which results in all wavelengths traveling at the speed



a. Flume data



b. Model results

Figure 6.8. Depth contours (feet above channel bottom) for trapezoidal-to-rectangular transition.

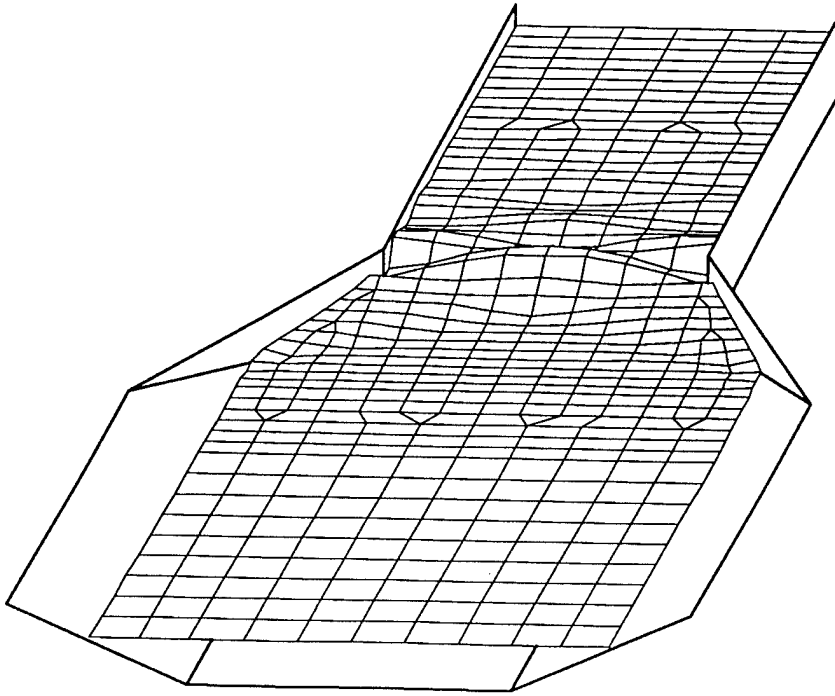
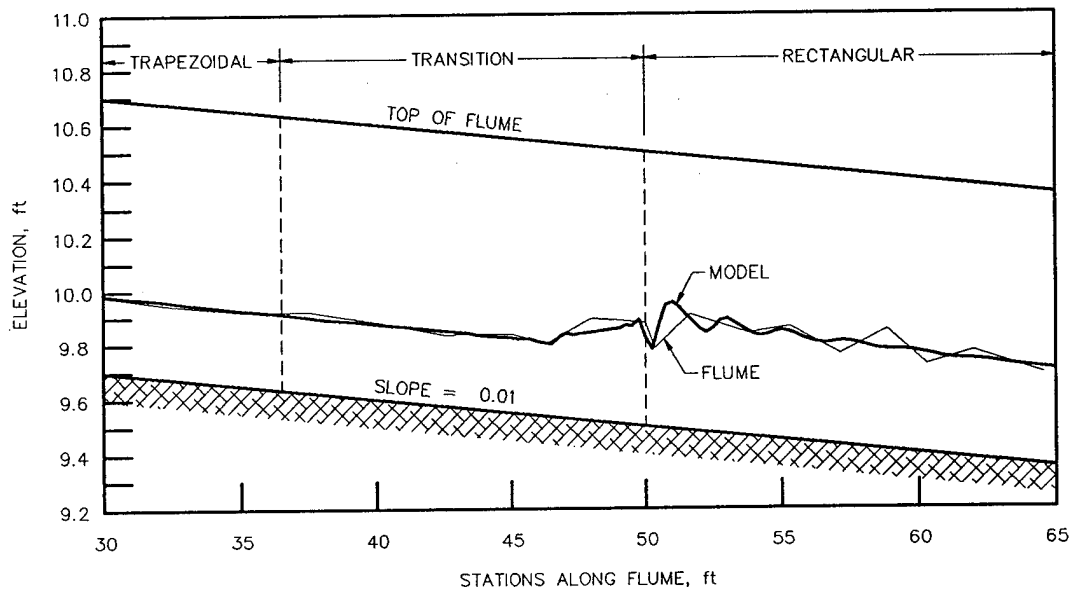


Figure 6.9. Computed water-surface mesh for trapezoidal-to-rectangular transition.

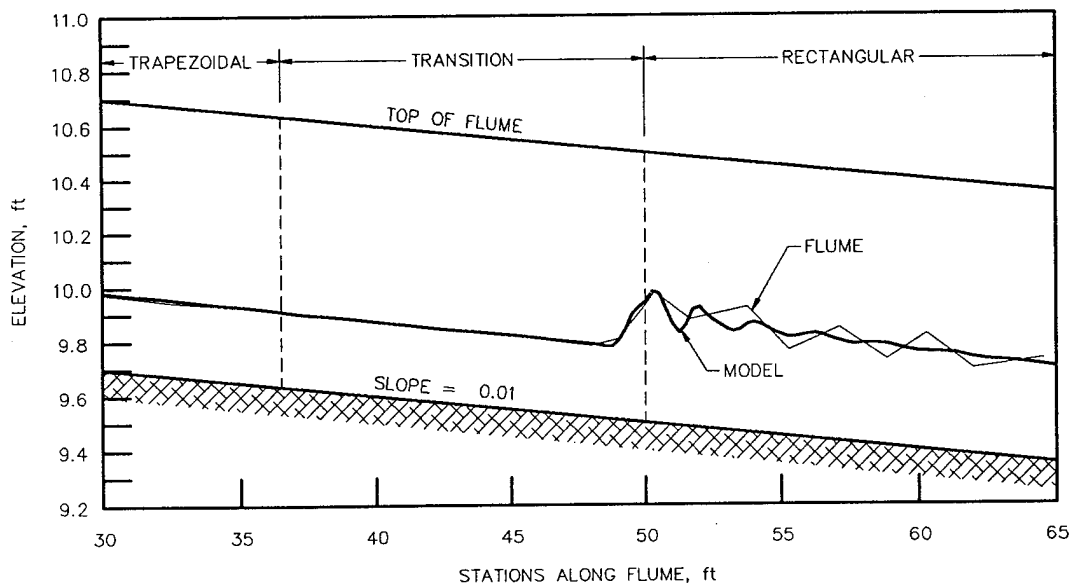
of a long wave, $c = (gh)^{1/2}$. Actually however, the wave celerity is dependent on the wave length, L_w , and is given as (Lamb 1945)

$$c_R = \sqrt{\frac{gL_w}{2\pi} \tanh\left(\frac{2\pi h}{L_w}\right)} . \quad (6.3)$$

As the depth to wavelength ratio (h/L_w) becomes small, c_R approaches c .



a. Profile along left wall



b. Profile along centerline

Figure 6.10. Water-surface profiles for trapezoidal-to-rectangular transition, $n = 0.009$, $C_b = 0.1$, $\hat{h} = 0.01$ ft (datum is 10 ft below sta 0 invert elevation).

The standing waves patterns generated by supercritical flow moving past an inward wall deflection in a rectangular channel are sketched in figure 6.11. The angle between a standing wave front and the upstream wall direction in a rectangular channel is a function of the average approach velocity (U) and the wave celerity (Ippen 1951). For small disturbances, the actual wave angle, δ_R , is

$$\delta_R = \sin^{-1} \left(\frac{c_R}{U} \right) \quad (6.4)$$

whereas the angle given by the shallow water equations is

$$\delta_{SW} = \sin^{-1} \left(\frac{c}{U} \right). \quad (6.5)$$

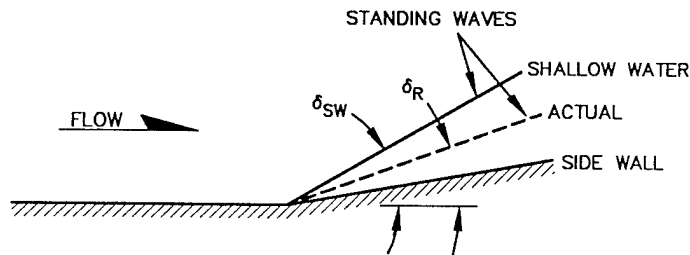
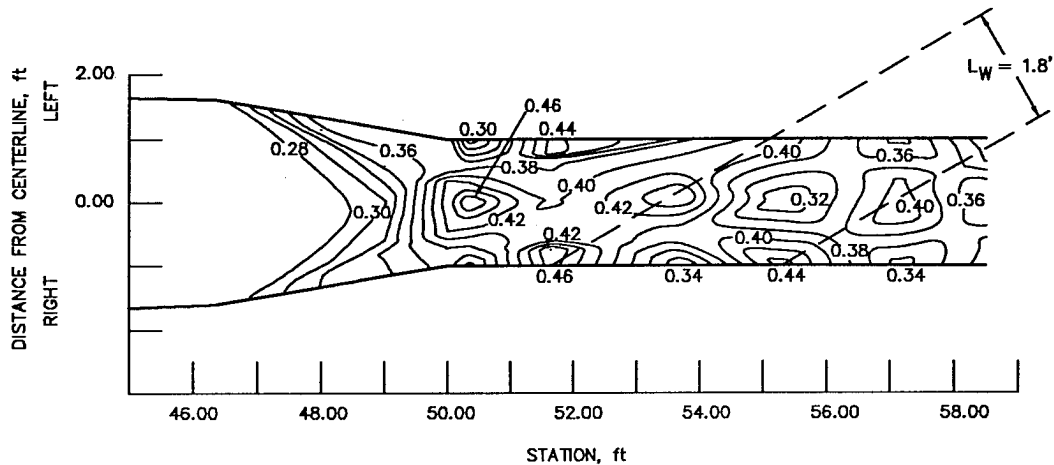
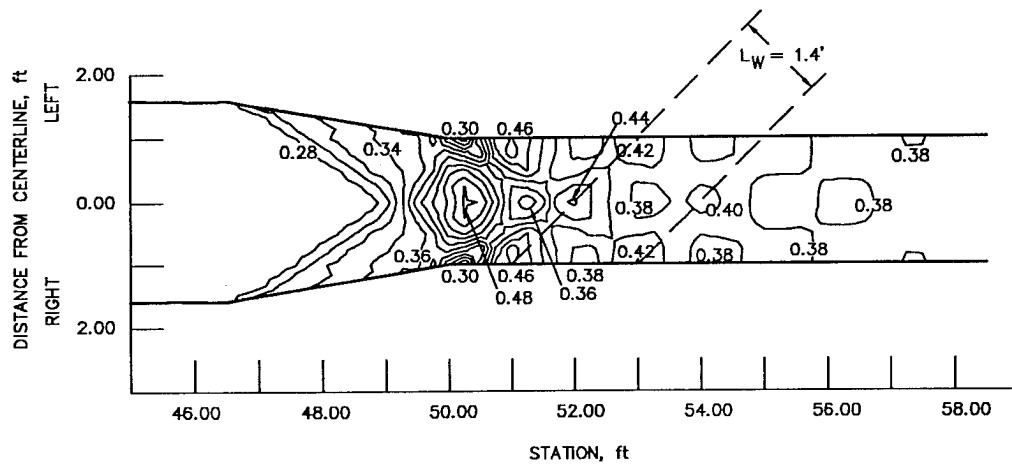


Figure 6.11. Plan view schematic of actual and shallow water model standing wave patterns.

Computed and observed wavelengths are shown on the depth contour plots presented in figure 6.12. The measured wavelength and average flow depth in the flume are approximately 1.8 ft and 0.38 ft, respectively. This depth to wavelength ratio of 0.21 results in an actual wave celerity of 2.8 ft/sec; whereas, the shallow water



a. Flume data



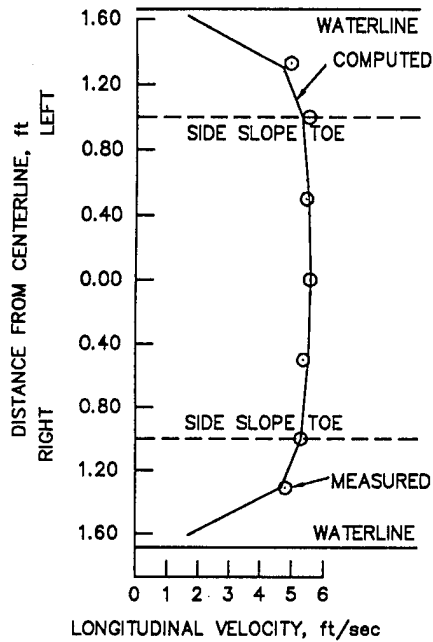
b. Model results

Figure 6.12. Computed and observed wavelengths for trapezoidal-to-rectangular transition.

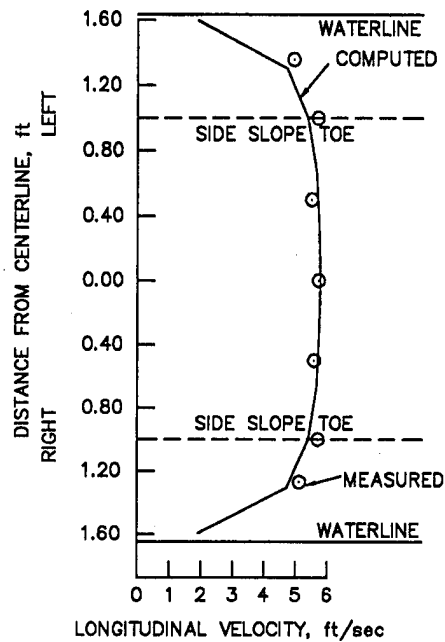
wave celerity associated with a depth of 0.38 ft is 3.5 ft/sec. At an h/L_w of 0.21, the shallow water wave celerity is about 25 percent too high due to the inclusion of an assumed hydrostatic pressure distribution. Because the celerity computed by the shallow water model is too high, the standing wave angle is too large and the distance between peak depths is too short. Employment of higher order shallow water equations which better describe the fluid pressure as influenced by vertical accelerations could reduce the standing wave phase error. However, these Boussinesq equations are still limited to small amplitude waves (Peregrine 1967) and therefore will not accurately model the wave patterns of three-dimensional flow with large water surface curvature. Modeling considerations regarding these higher order equations are further discussed in Chapter 7.

Velocity comparisons are shown in figure 6.13. Each reported measured velocity is the average of three point velocity measurements throughout the flow depth at the station except at stations near the waterline where a single velocity at 60 percent of the depth was assumed to equal the depth average. The three velocities were measured at points that were at 17, 50, and 83 percent of the depth. The velocity plots show that the model results compare well with the observed velocities.

The trapezoidal-to-rectangular channel transition test illustrates the model's ability to simulate oblique standing waves. The phase difference between the model and the real flow should be of little consequence in making engineering decisions regarding the maximum wall height required to contain the flow in a channel being designed. Because of uncertainty in the variations of flow depth above temporal mean



a. sta 30.0



b. sta 40.0

Figure 6.13. Computed and observed depth-averaged longitudinal velocities for trapezoidal-to-rectangular transition (left and right referenced to looking downstream).

averages, constructed wall heights are a maximum in the vicinity of transitions and are only gradually decreased toward stations where the flow is near uniform, thus providing adequate freeboard throughout the region of large standing waves.

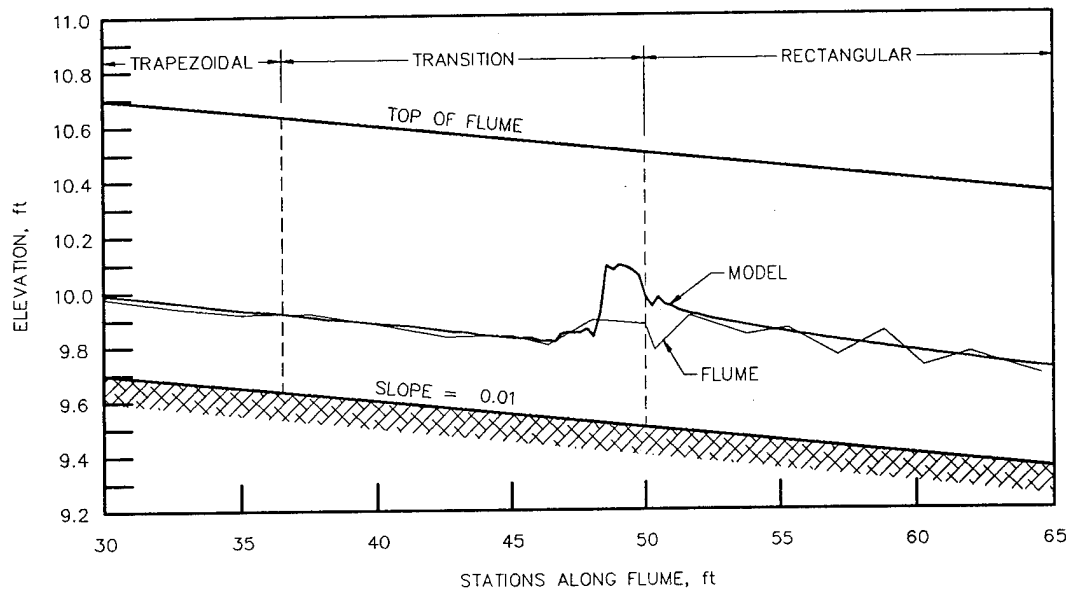
Parameter Sensitivity Tests

Additional simulations of the trapezoidal-to-rectangular transition were

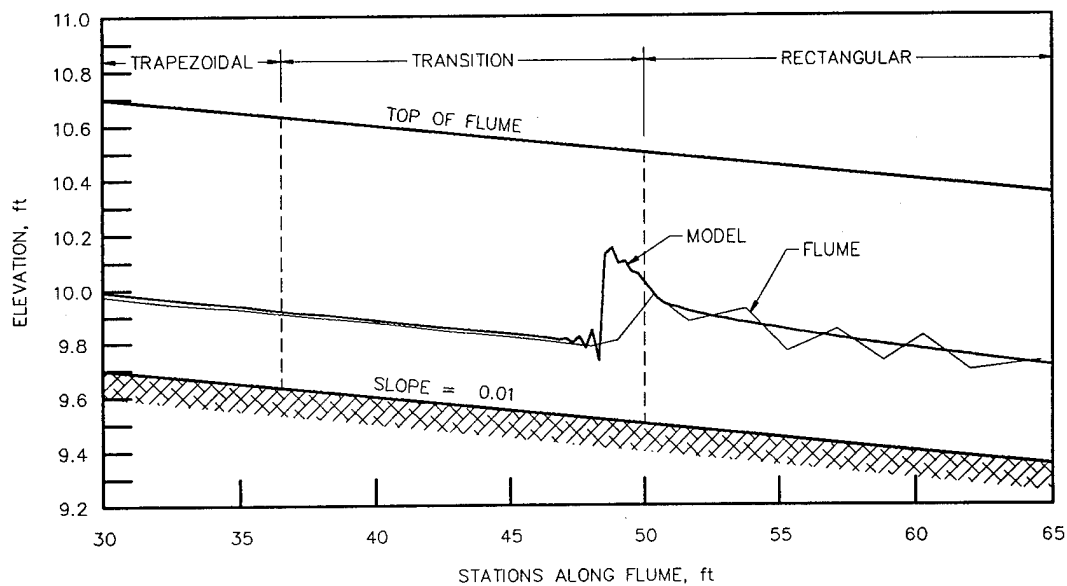
conducted to evaluate the model's sensitivity to the values of specified parameters. In each of these tests, one parameter was changed from the previously reported values (table 6.2) and the model was time stepped to the steady state solution using the results shown in figure 6.8 as the initial conditions. The parameters evaluated were the Manning's roughness coefficient (n), the turbulent kinematic viscosity coefficient (C_b), and the constant depth at the moving boundary nodes (\hat{h}).

Test 1: Manning's n Value

The Manning's n value was changed from 0.009 to 0.010. The steady state solution for $n = 0.010$ is shown as water-surface profiles in figure 6.14. The larger n value resulted in a hydraulic jump forming near sta 48, just upstream of the lower end of the transition. The energy losses along the transition approach with the increased bed roughness resulted in insufficient specific energy to pass the flow through the transition as supercritical. Examination of the water surface elevations upstream of the transition indicates that the computed flow depth is larger than that measured in the flume; whereas, the computed flow depth for a $n = 0.009$ is very close to the observed depth (figure 6.10). These types of laboratory flumes have been documented at the Waterways Experiment Station as having a roughness equivalent to a $n = 0.009$; however, data reduction of these tests were based on unidirectional flow using the hydraulic radius as the flow area divided by the wetted perimeter rather than employing the wide channel assumption that the flow depth approximates the hydraulic radius as is used in the two-dimensional model. The Test 1 results indicate that $n = 0.009$ is appropriate for two-dimensional modeling of the epoxy painted



a. Profile along left wall



b. Profile along centerline

Figure 6.14. Water-surface profiles for trapezoidal-to-rectangular transition, $n = 0.010$, $C_b = 0.1$, $\hat{h} = 0.01$ ft (datum is 10 ft below sta 0 invert elevation).

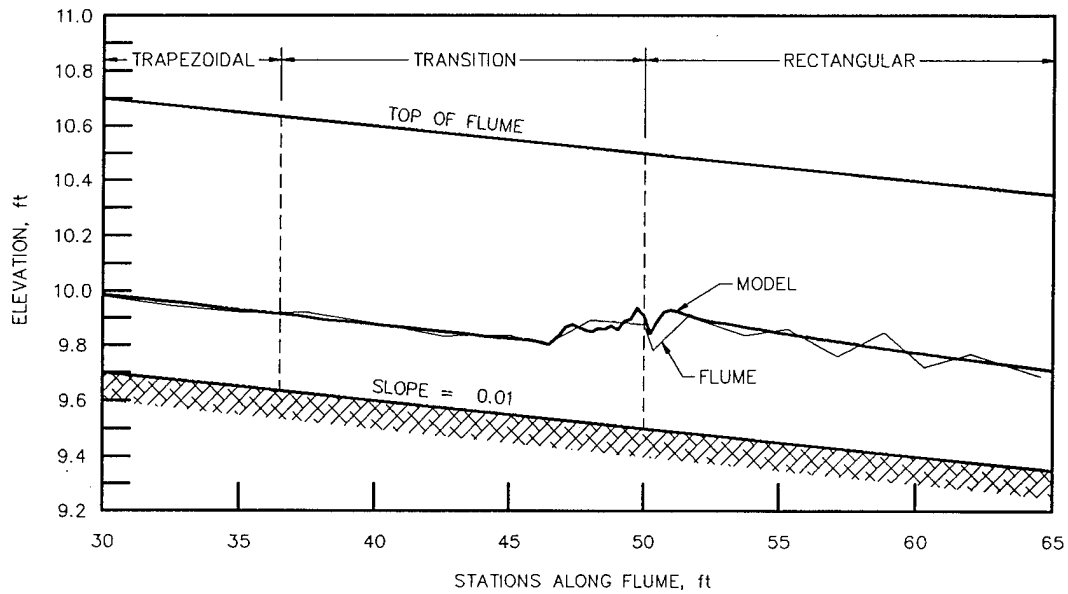
surface of the channel shapes and sizes constructed for the flume tests used here.

Test 2: Turbulent Kinematic Viscosity Coefficient

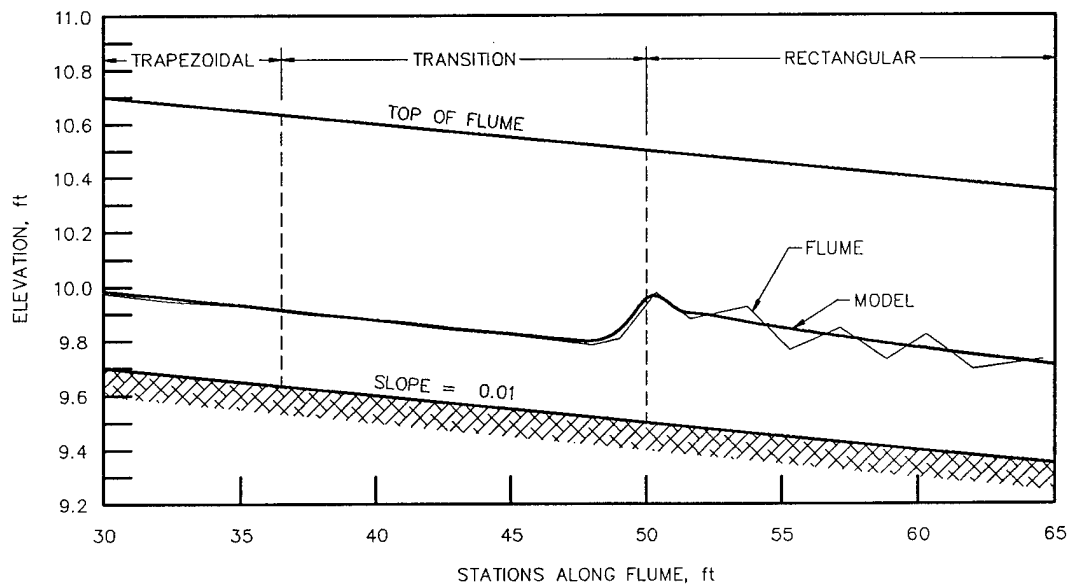
The turbulent kinematic viscosity coefficient (C_b) used in 4.5 was increased by an order of magnitude to test the model sensitivity to selection of this parameter. A C_b value of 1.0 was chosen resulting in a turbulent kinematic viscosity (ν_t) of 0.23 ft²/sec. Initial conditions for this test were the steady state solution shown in figure 6.8. The order of magnitude increase in ν_t did not have a significant effect on the steady state solution for this particular channel and flow configuration. Water-surface profiles resulting from a ν_t of 0.23 ft²/sec are shown in figure 6.15. The increased viscosity did not affect the amplitude of the first standing wave at the channel centerline (figure 6.15b) which compares well with the laboratory data. However, use of the increased viscosity dampened the computed reflected waves downstream of the first waves. The flow depth approaching the transition seems to be modeled correctly using this large viscosity, yet the relatively smooth water surface downstream of the first wave is unrealistic. These test results show that a C_b value of 0.1 provides much better model results than a C_b value of 1.0. The viscosity associated with the large value of C_b over damped the standing waves following the initial wave.

Test 3: Flow Depth at the Moving Boundary

The final sensitivity test evaluated the model response to a smaller flow depth \hat{h} at the moving boundary nodes. A depth of $\hat{h} = 0.005$ ft was selected for this test. This constant depth is one half the value used for the previously discussed tests (figure 6.8). Water-surface profiles of the steady state solution with \hat{h} equal to 0.005 ft are



a. Profile along left wall



b. Profile along centerline

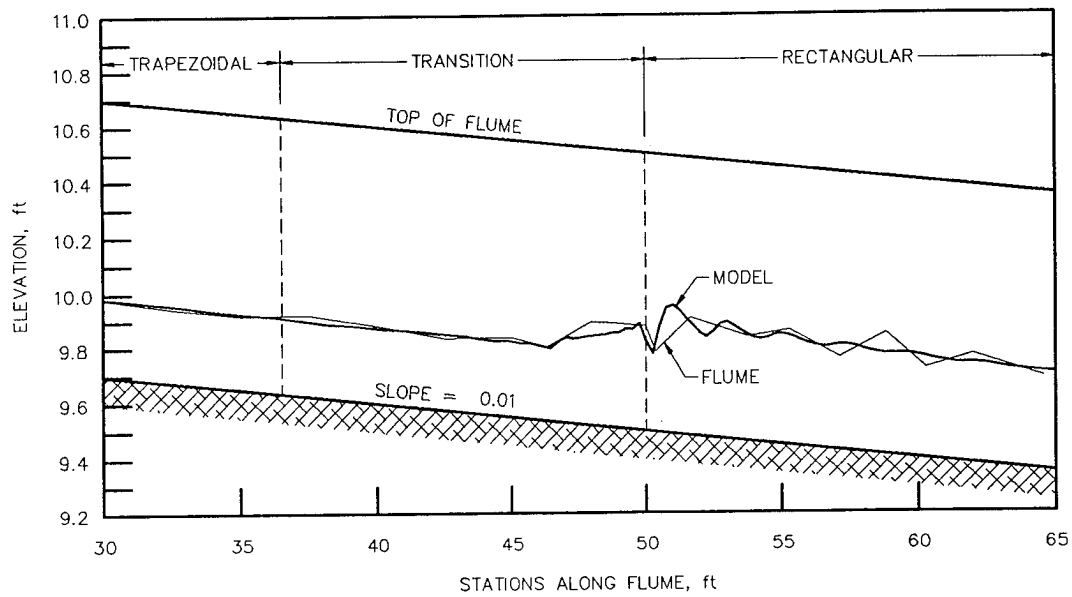
Figure 6.15. Water-surface profiles for trapezoidal-to-rectangular transition, $n = 0.009$, $C_b = 1.0$, $\hat{h} = 0.01$ ft (datum is 10 ft below sta 0 invert elevation).

shown in figure 6.16. As expected, the water surface elevations are practically identical to those computed using an \hat{h} value of 0.01 ft.

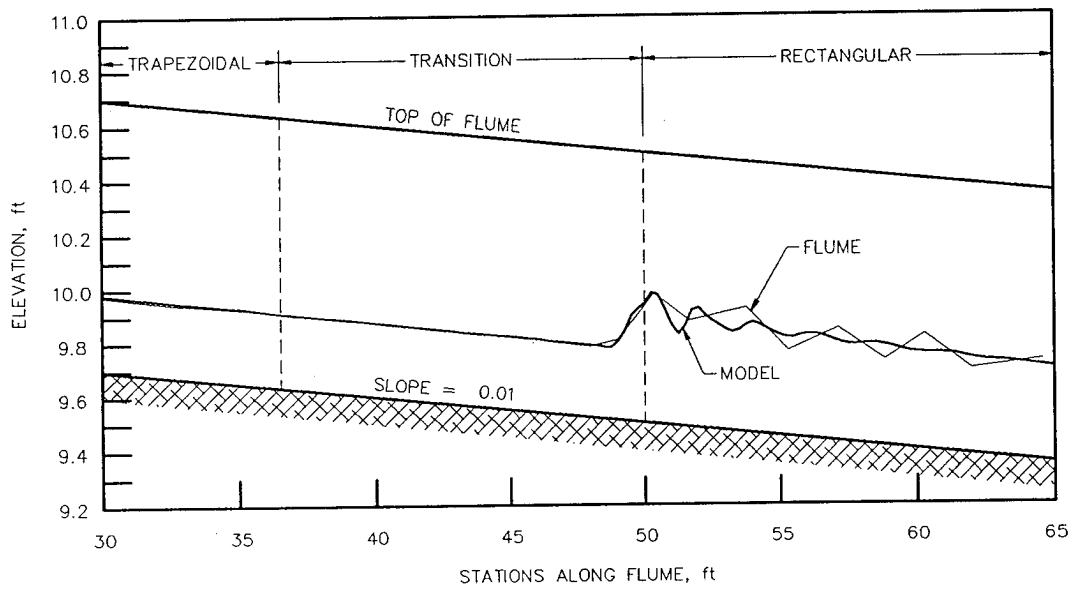
At this point in the testing process, the model's sensitivity to selection of initial conditions was investigated. The model's sensitivity to each of the three parameters was reevaluated using a grid similar in resolution to that shown in figure 6.5b, but rather than using the flow conditions shown in figure 6.8 as the initial conditions, uniform flow conditions (normal depth and velocity) were used as the initial conditions. The steady state solution resulting from these initial conditions were for all practical purposes indistinguishable from the results reported above in the Test 1 through Test 3 sections.

These results indicate that for the discharge and geometric design tested, the model is insensitive to the choice of flow depth at the moving boundary within the range tested and that it is only mildly sensitive to the choice of turbulent kinematic viscosity coefficient. However, for the configuration tested, the model was found to be extremely sensitive to the selection of Manning's n . Therefore, in practice the hydraulic design process should include the evaluation of flow conditions resulting from a range of reasonable roughness coefficients such that an envelope of possible hydraulic conditions can be established. In a hydraulic design situation, without the benefit of laboratory observations, the model indicated that the 1 lateral on 6 longitudinal transition is too abrupt and that it may result in a choked flow condition.

When the model results are compared to the observed flume data, it is apparent that initially chosen values for these parameters (table 6.2) were appropriate for



a. Profile along left wall



b. Profile along centerline

Figure 6.16. Water-surface profiles for trapezoidal-to-rectangular transition,

$n = 0.009$, $C_b = 0.1$, $\hat{h} = 0.005$ (datum is 10 ft below sta 0 invert elevation).

evaluation of the hydraulic performance of the channel. Therefore, these values were used in all subsequent model testing.

Trapezoidal Channel with a Horizontal Curve

The flume, part of a site specific 1:16-scale physical model study of a flood control channel initiated for the U.S. Army Engineer, Los Angeles District, was a trapezoidal channel having a horizontal curve. A portion of the modeled reach consisted of a hydraulically steep, trapezoidal flume having a long horizontal curve. The bend provided a good test case since the direction of nodal displacement in the numerical simulation would vary along the length of the bend and the flow boundary on the inside of the bend would have a different elevation from that on the outside due to the superelevation of the water surface.

The portion of the facility tested for this study was nominally 52.84 ft long on centerline, with wall heights ranging from 0.31 ft to 0.44 ft above the invert, with base widths varying from 0.938 ft to 0.625 ft and side slopes varying from 1 vertical on 3 horizontal to 1 vertical on 2 horizontal. The channel slope was 0.0073. The side slopes in the 8.0-ft-long straight reach (sta 64.741 to sta 56.741) and in the 5.313-ft-long transition section (sta 56.741 to sta 51.428) were covered with crushed rock having an average diameter of 3/8 inches. The flow width within the straight reach was bounded to 2.813 ft by vertical walls at the top of the rock slopes. All other boundaries were constructed of plastic coated plywood covered with rolled epoxy paint. The channel bend was composed of a compound curve in which spiral curves were used to transition between the upstream and downstream tangents to a circular

curve. The circular curve was of radius 15.625 ft. A plan view of the flume is shown in figure 6.17 and photographs of the flume are shown in figure 6.18.

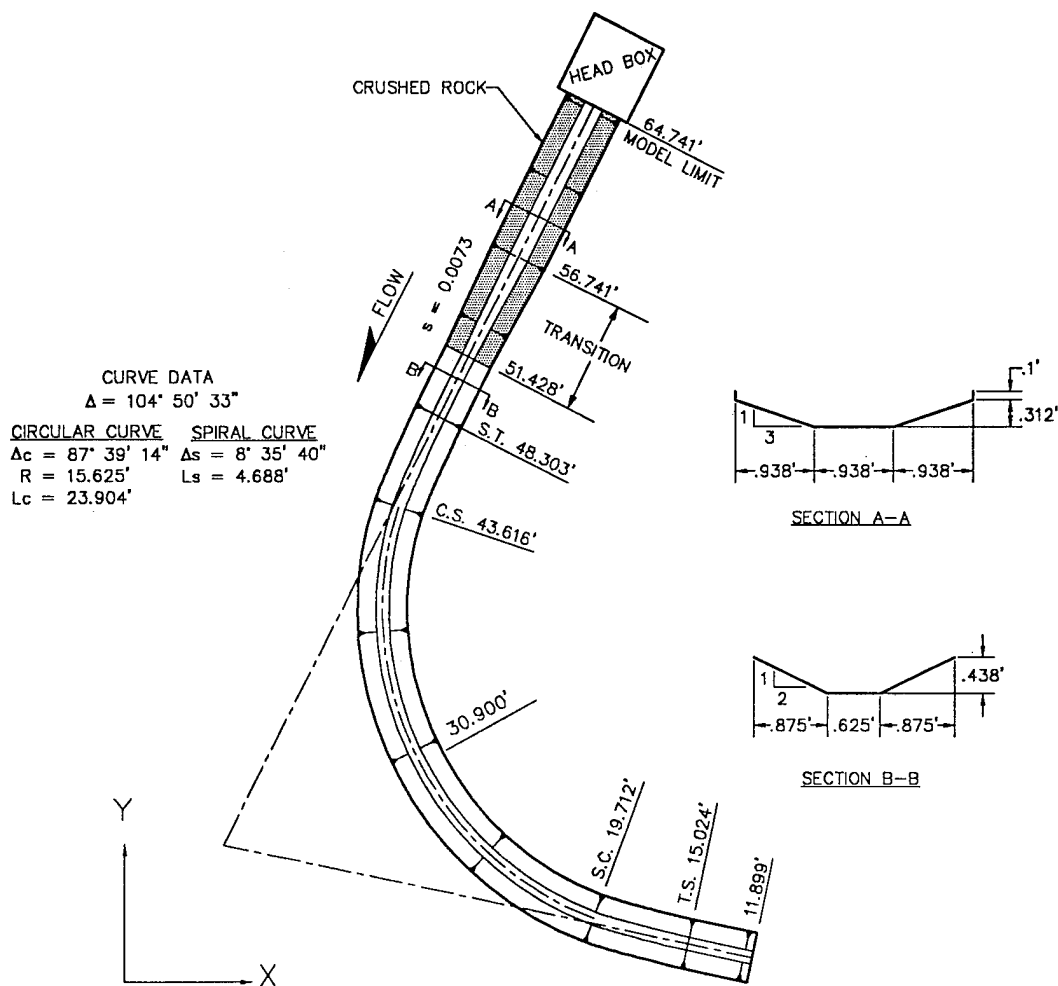
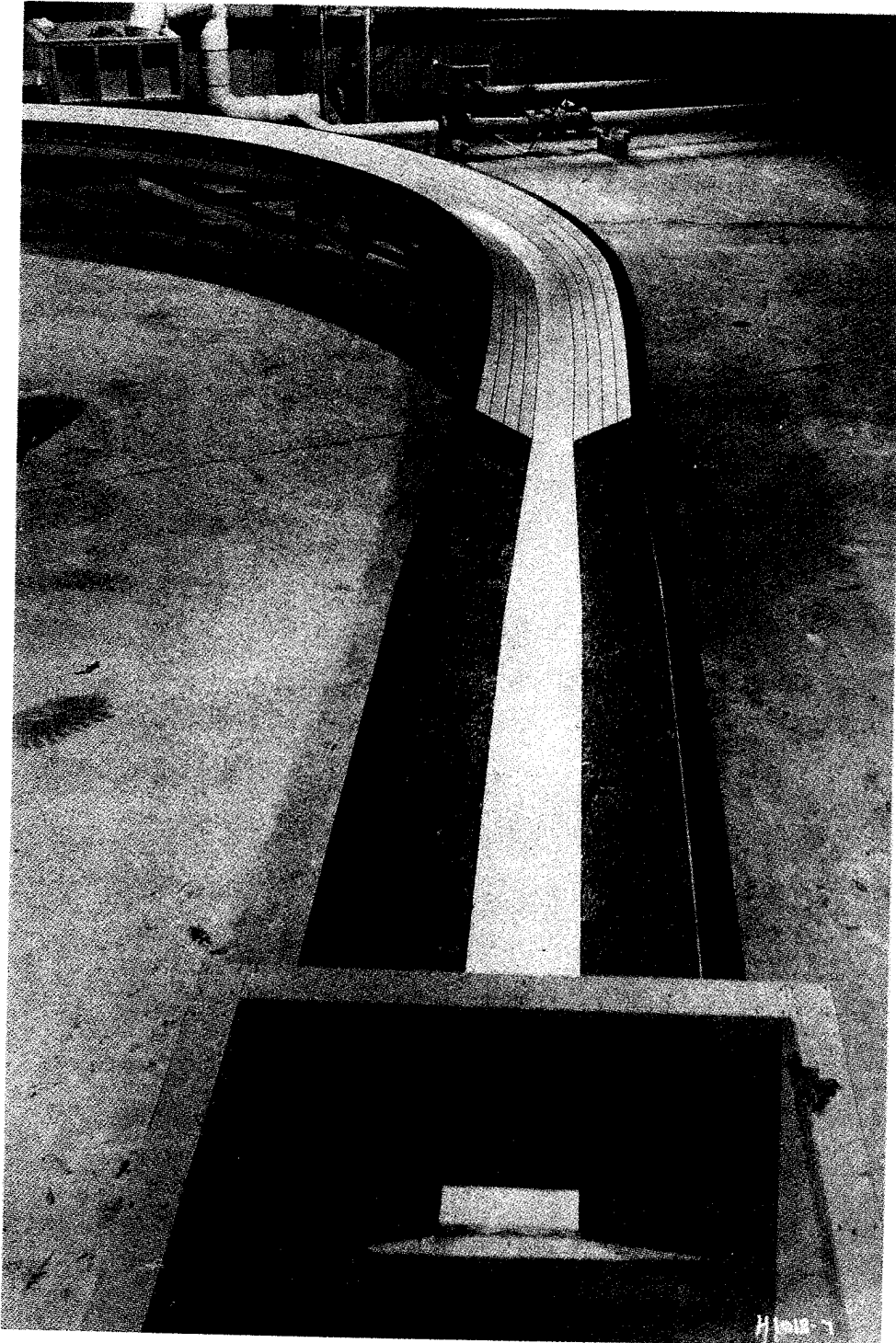
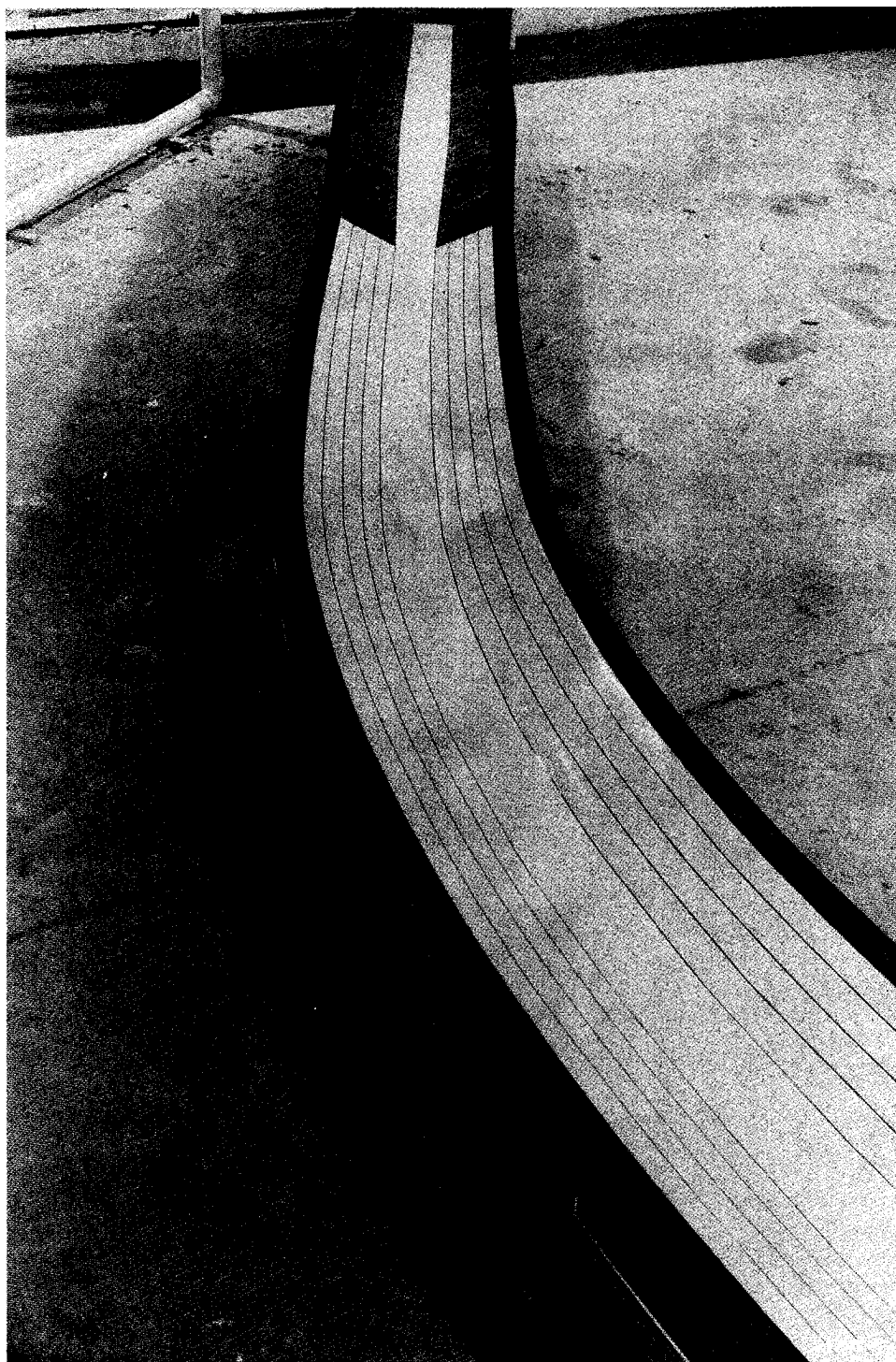


Figure 6.17. Plan view and sections of trapezoidal horizontal curve.



a. Looking downstream

Figure 6.18. Dry bed view of trapezoidal horizontal curve.



b. Looking upstream

Figure 6.18 continued.

Water was supplied from a pump to an 8-inch diameter inflow pipe. The flume discharge was returned to the sump through a drain line. The rate of flow entering the flume was measured using a 6-inch by 3.6-inch venturi meter installed in the inflow pipe. Point gages were used to measure flow depths and a propeller type probe was used to measure velocities. Flow was introduced in the flume by means of a headbox. The flume inflow was subcritical and therefore a sluice gate was not required. The subcritical inflow was established by downstream control within the rock lined transition where the flow accelerated through critical. Upstream of the transition the flow was subcritical and supercritical flow existed downstream of the transition. The outflow downstream of the transition was supercritical and therefore no tailwater level was set.

Test Conditions

Comparisons were made of model results with lab data obtained in the flume with a discharge of 1.22 ft³/sec. The flow conditions in the laboratory flume are shown in figure 6.19. The numerical model used a Manning's n of 0.009 for the epoxy painted plywood area. The n value associated with the crushed rock placed on the side slopes at the upper end was estimated to be 0.021 using the following form of Strickler's equation (US Army, Office, Chief of Engineers 1991):

$$n = 0.036 (D_{90})^{1/6} \quad (6.6)$$

where D_{90} is the size of which 90 percent of the sample is finer and is given in feet. The value for D_{90} was estimated assuming a linear variation in gradation from the D_{100} to the D_{50} values. The roughness parameters were chosen prior to the numerical

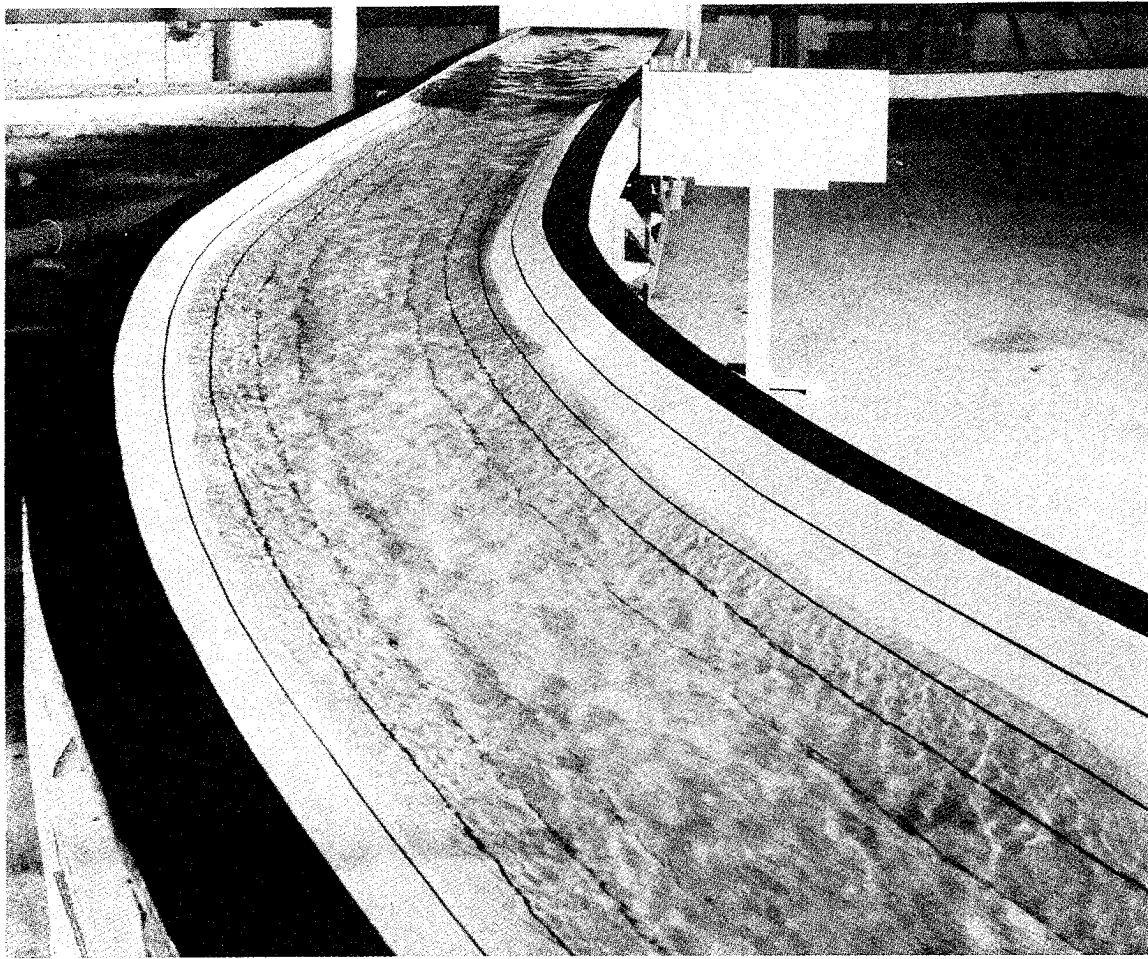


Figure 6.19. Flow conditions in trapezoidal horizontal curve (looking upstream).

model simulations. The values were never changed (or adjusted) to make the model results agree with the measured data; the model was not calibrated to reproduce the flume data.

As with the first test, the initial top width of the flow was based on calculated normal depths. Normal depths were computed assuming uniform straight channels having cross sectional shapes and slopes identical to the curved flume. Two depths

were computed, one for the upper end using an n value of 0.021 for a channel having a base width of 0.938 ft and 1 vertical on 3 horizontal side slopes and one using an n value of 0.009 for a channel having a base width of 0.625 ft and 1 vertical on 2 horizontal side slopes. Both uniform depths were computed using the channel slope of 0.0073. Given a flow depth, the channel base width, and side slopes, the top width was computed for the initial grid. The normal depth for the upper end was 0.31 ft and normal velocity was 2.08 ft/sec (Froude number of 0.81). The normal depth for the section having 1 vertical on 2 horizontal side slopes was 0.25 ft and the normal velocity was 4.25 ft/sec (Froude number of 1.79). The initial mesh, shown in figure 6.20a, had 629 nodes and 541 elements and was considered coarse, but adequate for startup. Lateral resolution of the channel bottom was 3 elements for the upstream portion (bottom width = 0.938 ft) and 2 elements for the remainder of the channel (bottom width = 0.625 ft). Two elements were used on each side slope of the initial mesh.

In the same manner as the previous trapezoidal-to-rectangular transition was modeled, the upstream and downstream ends of the mesh were composed of additional points representing a "headbox" in addition to points added at the downstream end representing a "tailbox". These additional points were used to simplify the boundary condition input. A rectangular section at the inflow boundary simplifies the specification of inflow discharge. The unit discharge is merely the total discharge divided by the width of the rectangular inflow boundary; whereas, the unit discharge at a trapezoidal inflow section varies with depth assuming uniform velocity across the

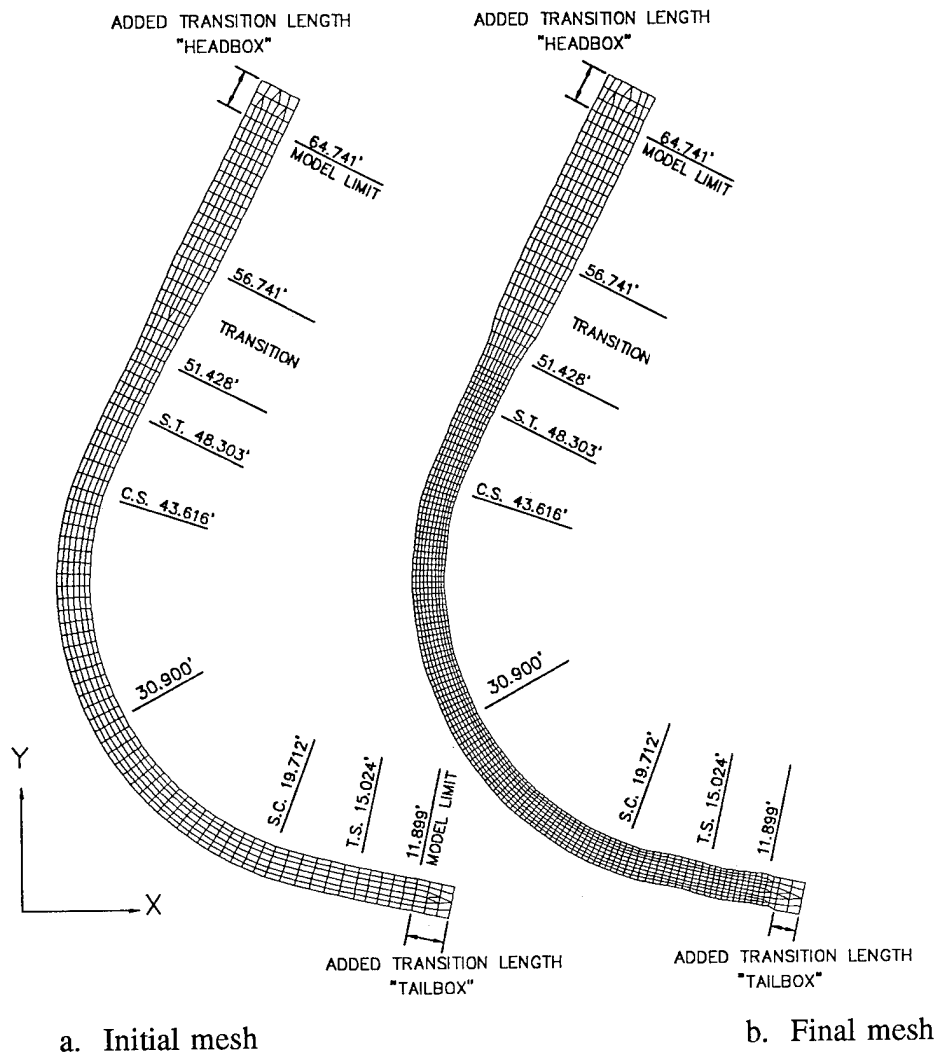


Figure 6.20. Numerical model computational meshes for trapezoidal horizontal curve.

inflow boundary. The use of a rectangular section at the outflow boundary results in fixed nodes at the waterline at the outflow boundary. Because a moving waterline boundary at the outflow boundary produces an additional source of nonlinearity in the solution, a trapezoidal section at the outflow boundary is not desirable. This is the reason additional elements representing a tailbox were used at the outflow boundary

which simplified the model's adherence to specified outflow boundary conditions. These "boxes" in which the boundary nodes were fixed produced a gentle transition from rectangular to trapezoidal shape at the upstream end and trapezoidal to rectangular shape at the downstream end.

The inflow boundary flow was subcritical and required the specification of p and q at each inflow node. Values of p and q were determined as the total discharge ($1.22 \text{ ft}^3/\text{sec}$), applied normal to the inflow boundary, divided by the width of the inflow boundary (2.758 ft). The outflow boundary was supercritical and therefore, no boundary conditions were specified. The upstream and downstream boundary conditions are listed in table 6.3 where the values of p and q are valid for the x and y coordinate system orientation shown in figure 6.20. The coordinate system orientation coincided with the North and East directions of the prototype project plans from which the flume was constructed. The model parameters used for this simulation are presented in table 6.4. The specified boundary depth, $\hat{h} = 0.01 \text{ ft}$, was less than 5 percent of the depth at the channel center in each of the two reaches thus producing a cross sectional area error of roughly 0.06 percent. This specified boundary depth of 0.01 ft applied to normal flow conditions in section A-A (figure 6.17) resulted in an initial grid width of 2.258 ft for this section. An initial grid width of 1.705 ft for section B-B was computed using normal depth (0.28 ft) and a boundary depth of 0.01 ft .

Initially 0.1 sec time steps were used for the simulation for a time of 15 sec . This time step resulted in a Courant number of 1.0 . The time steps were then

Table 6.3: Curved channel, trapezoidal cross section, boundary conditions.

Boundary	Flow Regime	Boundary Condition	Value
Inflow	Subcritical	h	Not Specified
		p	-0.1999 ft ² /sec
		q	-0.3947 ft ² /sec
Outflow	Supercritical	h	Not Specified
		p	Not Specified
		q	Not Specified

Table 6.4: Curved channel, trapezoidal cross section, model parameters (n_1 is Manning's coefficient for the smooth plywood and n_2 is for the crushed rock).

Condition	Value
α	1.0
β	0.1
n_1, n_2	0.009, 0.021
C_b, v_t	0.1, 0.015 ft ² /sec
\hat{h}	0.01 ft

increased to 0.25 sec and simulations were conducted for an additional 235 seconds resulting in a total time of 250 sec.

The computed flow variables and the boundary location at time 250 sec were equal to those resulting from 245 sec of simulation and therefore, this solution was taken to represent the steady state. After the steady state solution was obtained, the initial mesh was refined. Initial conditions for the refined mesh were obtained from the coarser mesh results using a bilinear interpolation scheme. Simulations were then run until steady state was obtained with the refined mesh. This process was continued until mesh convergence was reached, this being the point at which the solution did not change with additional mesh refinement. In this process of mesh convergence, a time step of 0.25 sec was used for a total simulation time of 385 sec. The resulting mesh is shown in figure 6.20b. This final mesh had 1450 nodes and 1303 elements. The primary difference in the coarse and resolved grids was that the finer grid provided slightly larger peak superelevations in the water surface resulting from runup and drawdown on the outside and inside of the bend, respectively.

Test Results

A plot of the computed and observed side boundaries is provided in figure 6.21. The model accurately solved the waterlines through the transition where the flow accelerated from subcritical to supercritical. Contours of the flow depth relative to the channel bottom are shown for the laboratory data and simulation results in figure 6.22. Longitudinal spacing of flow depth measurement varied from 1 ft to 0.27 ft while transverse spacing varied from 0.31 ft near the channel centerline to as

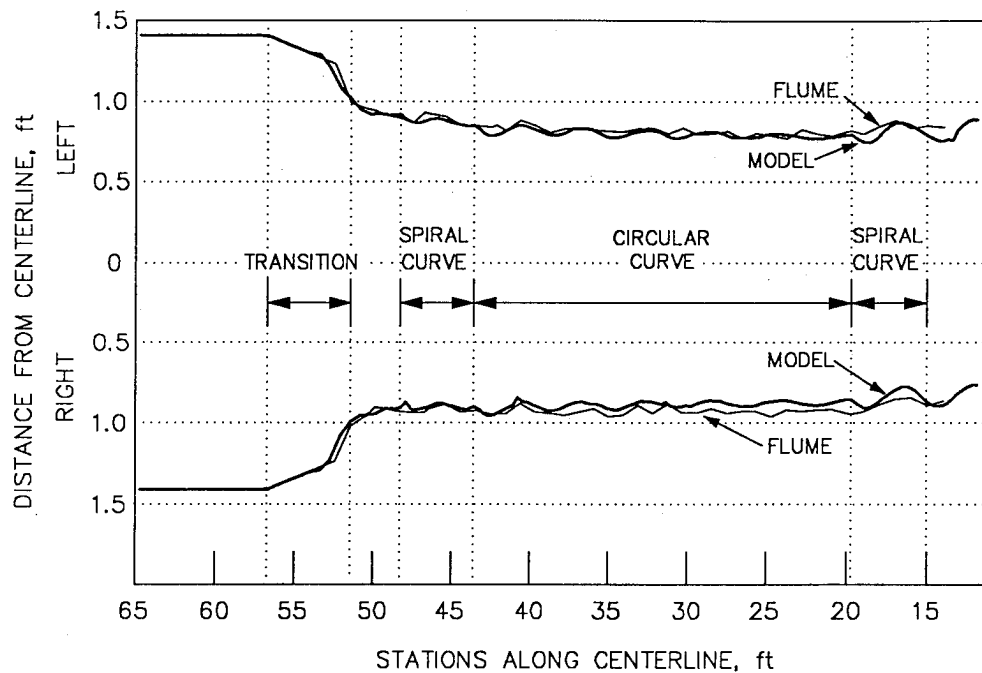
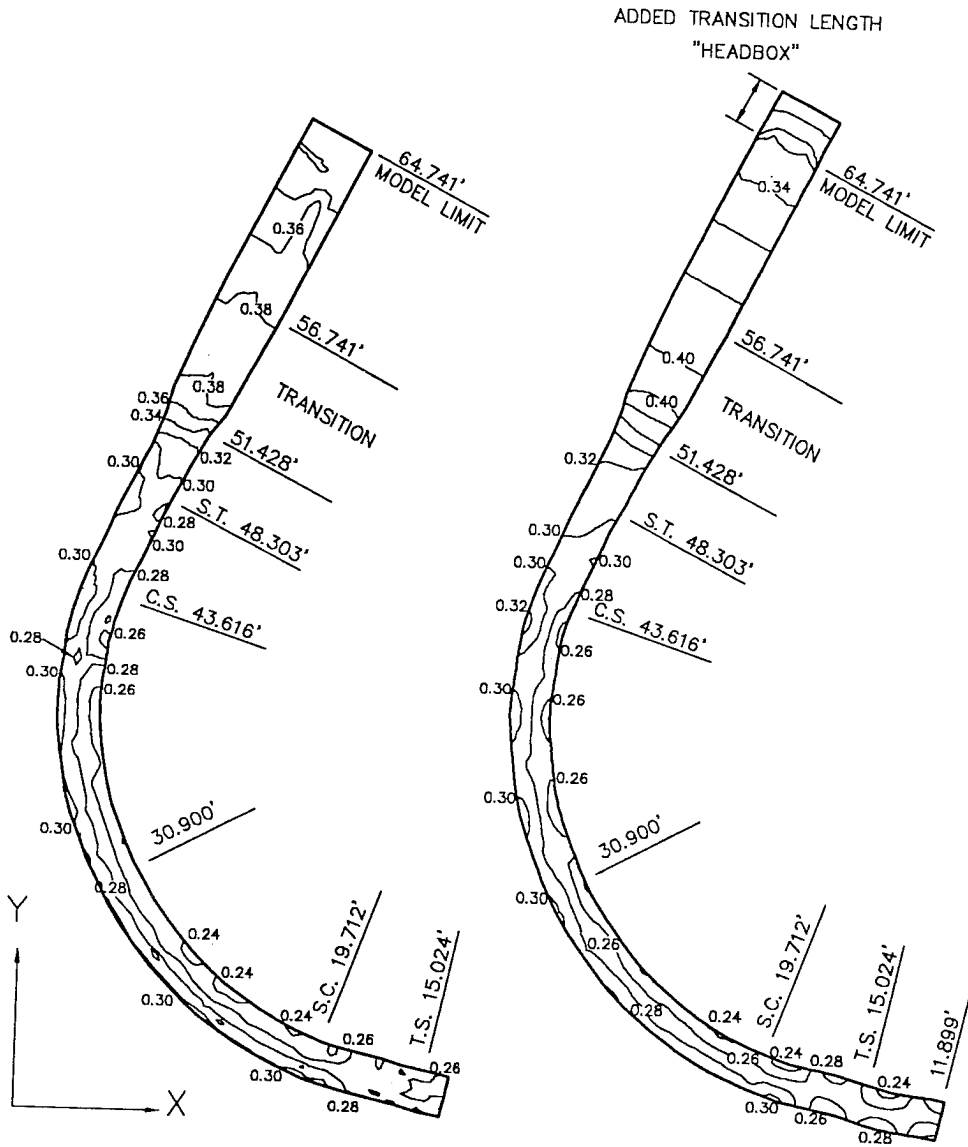


Figure 6.21. Computed and observed side boundaries for trapezoidal horizontal curve.

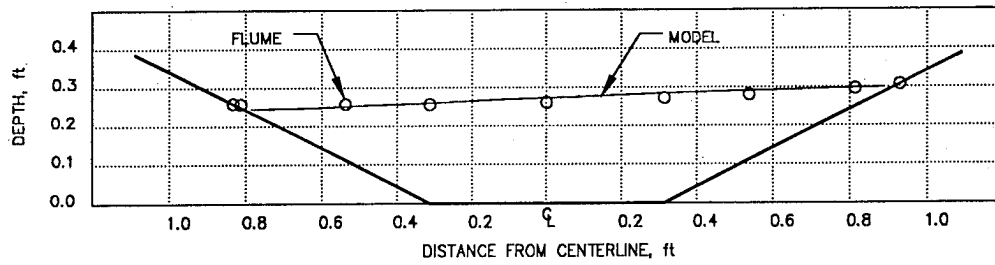
small as 0.02 ft near the waterline. Depth contours of the laboratory data (figure 6.22a) show that the entrance conditions caused flow disturbances at the upper end of the flume. The poor entrance conditions were of little importance since the primary concern of this study is the flow conditions within the channel curve. It is interesting to note the computed water-surface oscillations downstream of the bend as the flow adjusts to uniformity. Unfortunately the tangent reach in the flume was not long enough to produce these disturbances caused by the channel bend. Cross sectional plots of measured and computed water surface elevations near the midpoint of the curve, at the downstream end of the simple curve, and at the downstream end of the spiral curve are provided in figure 6.23. These results show that the superelevation in



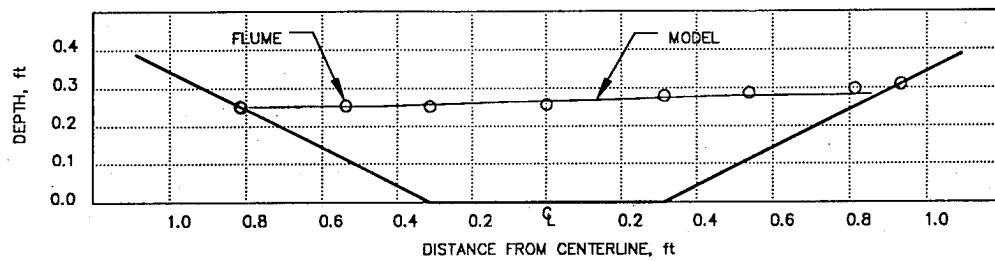
a. Flume data

b. Model results

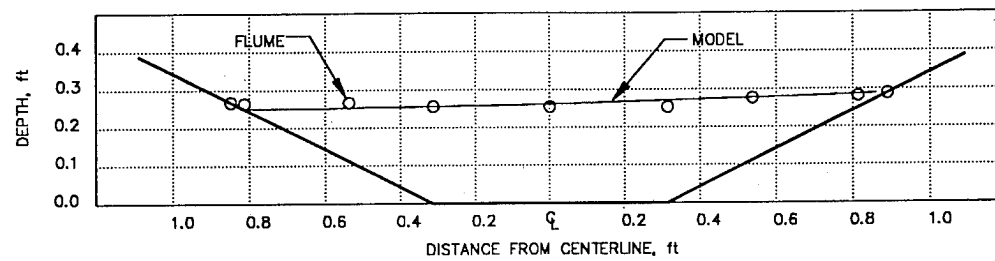
Figure 6.22. Depth contours (feet above channel bottom) for trapezoidal horizontal curve.



a. Sta 30.31



b. Sta 19.71



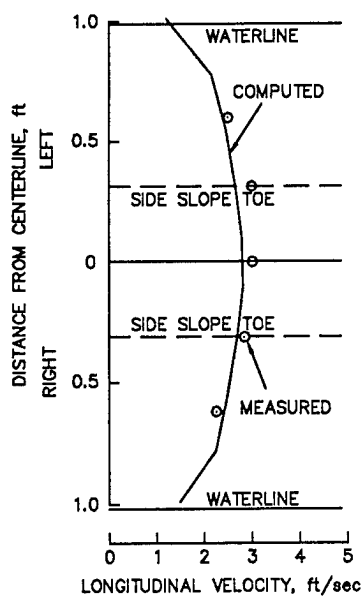
c. Sta 15.02

Figure 6.23. Cross section view of flow depth for trapezoidal horizontal curve (looking downstream).

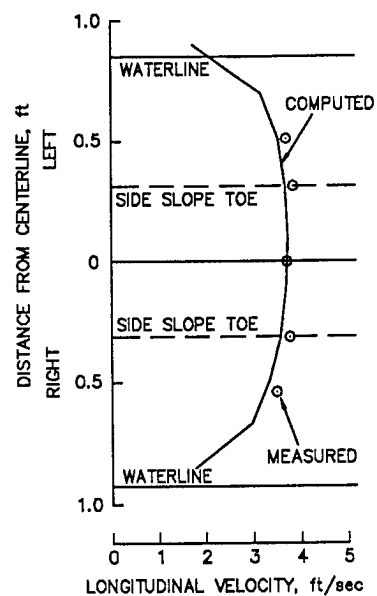
the bend is adequately captured. Figure 6.22 shows that the model adequately reproduces the amplitude of wave oscillations.

Depth-averaged longitudinal velocities at three stations are plotted in figure 6.24. The depth-averaged velocities were generally orientated in directions parallel to the channel centerline. Depth-averaged velocities were obtained in the laboratory by measuring three point velocities (at 17, 50, and 83 percent of the depth) throughout the flow column except at stations near the waterline where the velocity measured at 60 percent of depth was assumed to represent the depth average. The entrance conditions probably produced the unsymmetrical velocity distribution at sta 51.43. The depth contours and velocity plots indicate that the computed depths at sta 51.43 were too large and the velocities too low. However, the differences are small and suggest that the Manning's coefficient used for the crushed rock was perhaps too large. The lateral velocity distribution at sta 43.62 (beginning of the circular curve) is uniform in the channel center, but the largest velocities have migrated toward the outside of the bend at sta 30.90 (approximately the midpoint of the curve).

The depth-averaged model is not capable of simulating the migration of maximum streamwise velocity toward the outside of the bend because the so-called secondary flow that occurs in channel bends is a three dimensional phenomenon and is not addressed using the shallow water equations. Because of this limitation, engineering decisions such as riprap size selection for bank protection in trapezoidal channel bends should not be based solely on the results of depth-averaged models. These models can not provide the location and magnitude of the maximum channel

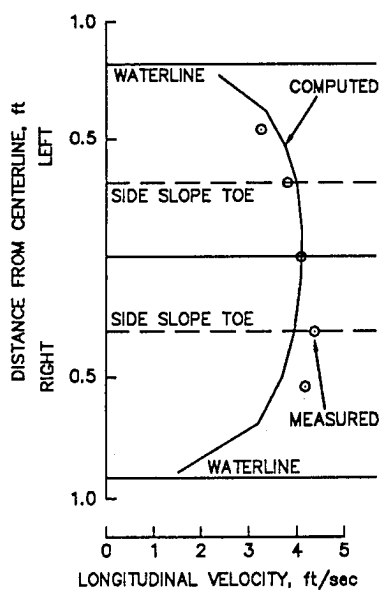


a. Downstream end of transition, sta 51.43



b. Beginning of circular curve,

C.S. sta 43.62



c. Near midpoint of curve, sta 30.90

Figure 6.24. Computed and observed depth-averaged velocities for trapezoidal horizontal curve (left and right directions are referenced to looking downstream).

velocity in trapezoidal channel bends. However, the model does capture the superelevation in the water surface within the channel bend which is most important in flood control channel design. Although the model did not accurately reproduce the velocities near the midpoint of the curve (figure 6.24c) the water surface elevations in this vicinity were accurately computed (figure 6.23a). Water surface elevations are of primary concern in designing high-velocity channels and the model has been shown to predict these satisfactorily.

Rectangular-to-Trapezoidal Transition

Additional model testing was conducted to evaluate the model's ability to capture oblique standing waves in trapezoidal channels. Data were obtained in the tilting open channel flume previously described (figure 6.1) having a base width of 2.0 ft and side slopes of 1 vertical on 2.25 horizontal. A rectangular-to-trapezoidal channel transition was constructed by placing vertical walls at the toe of the side slopes along the first 30.73 ft of the trapezoidal flume. These vertical walls were then continued up the side slopes for a distance of 13.5 ft resulting in a 1 lateral to 6 longitudinal transition on each sidewall (figure 6.25). The resulting flume cross sections were of rectangular shape from the upstream end at sta 0.0 to sta 30.73 and of trapezoidal shape from sta 44.23 to the flume end at sta 80.0. A dry bed photograph of the rectangular-to-trapezoidal transition is provided in figure 6.26.

Test Conditions

The flow conditions documented in the flume experiments and subsequently simulated using the numerical model consisted of a discharge of 3.6 ft³/sec on a slope

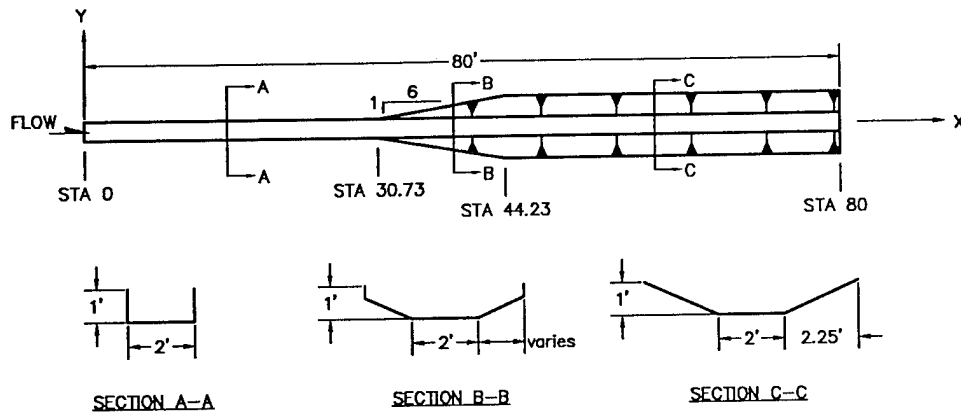


Figure 6.25. Plan view and sections of rectangular-to-trapezoidal transition.

of 0.012. Given uniform conditions, this channel configuration results in a computed Froude number of 2.2 in the transition approach where the channel was a 2-ft wide rectangular section. Flow conditions within and downstream of the transition are shown in figure 6.27. As the flow flared out at the upstream end of the transition, the flow on each side met the steep side slopes. This produced a rise in the water surface within the portion of the transition located over the sloping sidewalls. The flow depth near the channel centerline decreased beginning at the upstream end of the transition due to the expansion of the channel. The water runup on the side slopes and the depression along the centerline were followed by a depression along the side slopes and a rapid increase along the centerline as the standing waves generated at the side slopes intersected. These oblique standing waves resulted in varying waterlines along the left and right side slopes.

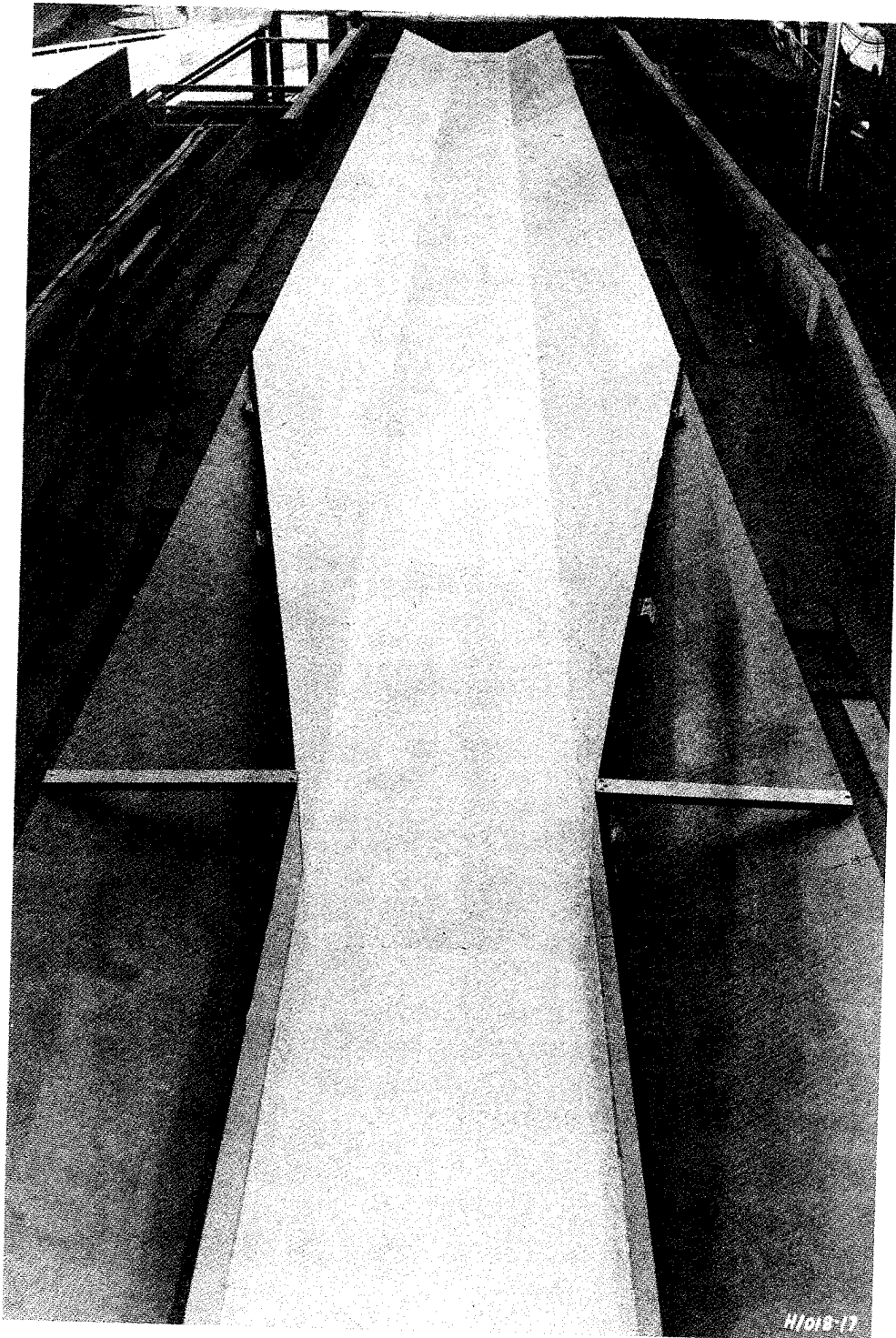


Figure 6.26. Dry bed view of rectangular-to-trapezoidal transition (looking downstream).

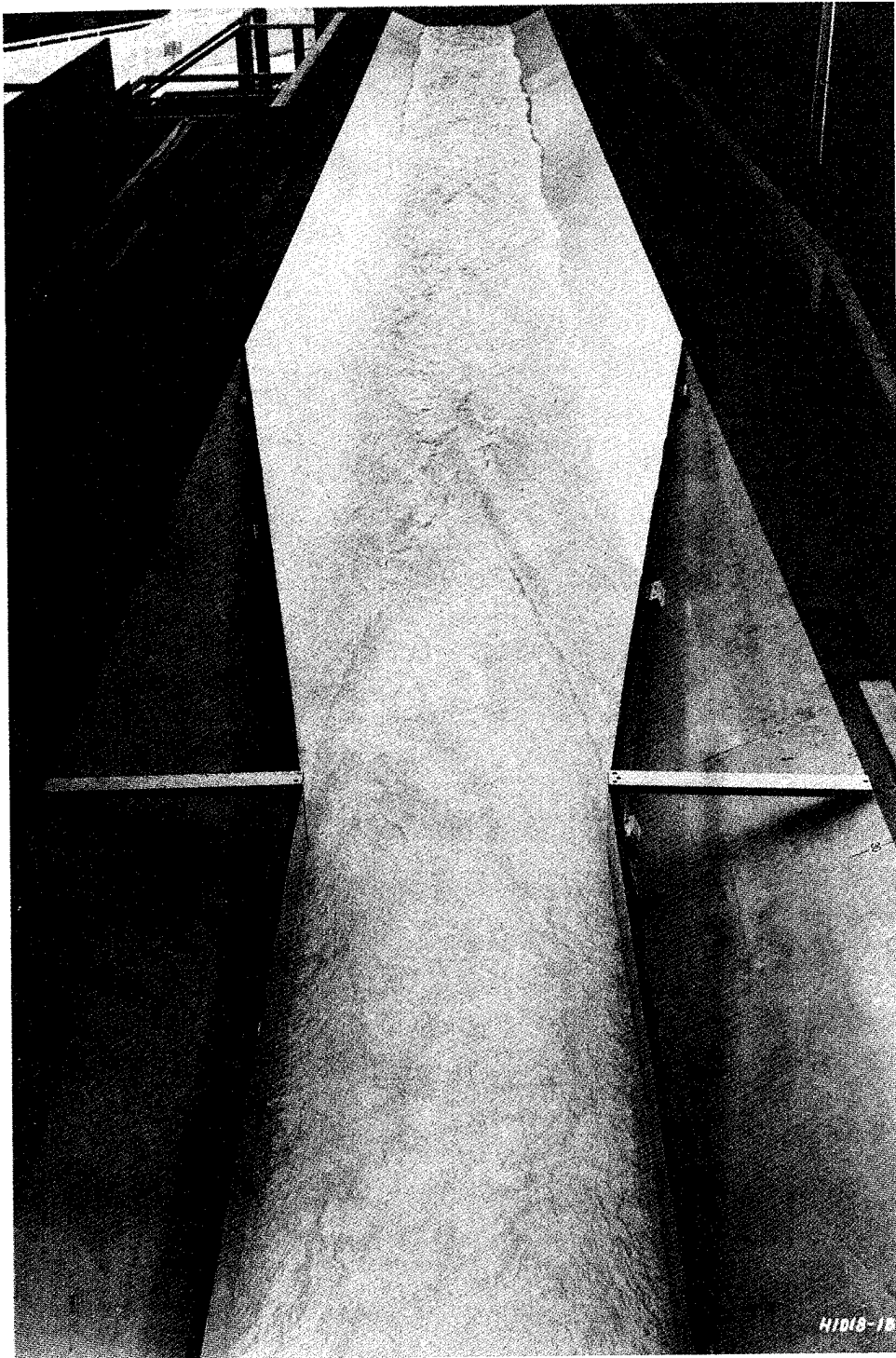
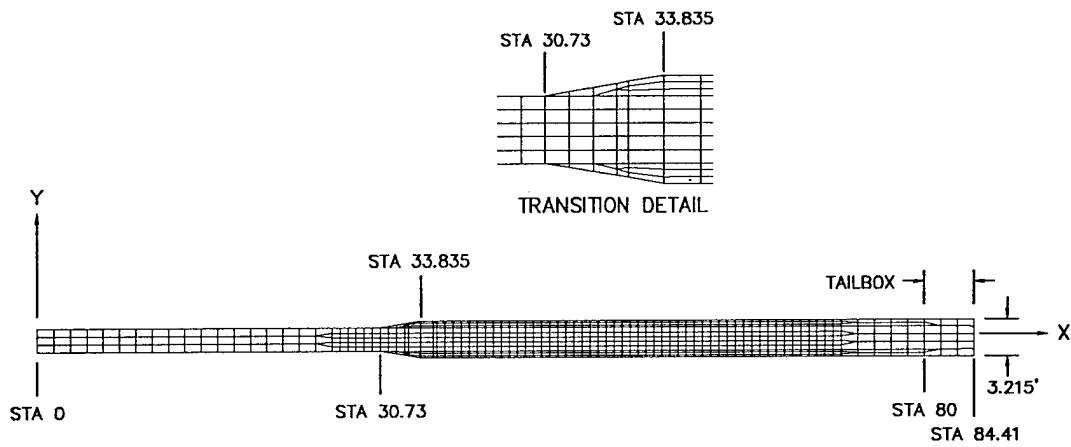
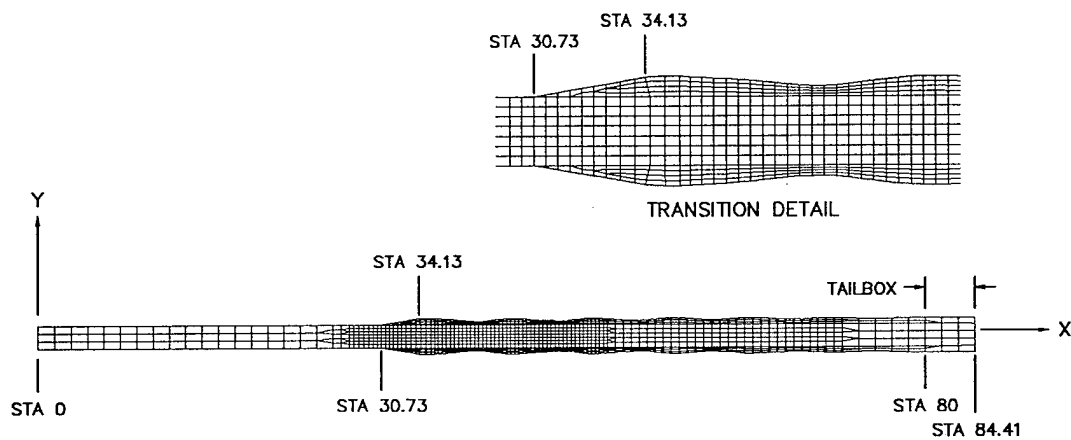


Figure 6.27. Flow conditions in rectangular-to-trapezoidal transition, approach Froude number = 2.2 (looking downstream).

In the same manner as the first two tests, the initial flow conditions and initial grid width were based on normal flow conditions assuming a Manning's n value of 0.009. Normal depth (0.28 ft) and velocity (6.5 ft/sec) were computed for the rectangular section and used as initial conditions for the upstream reach (sta 0.0 to sta 30.73). Also, normal depth (0.24 ft) and velocity (6.0 ft/sec) for the trapezoidal section were used as initial conditions for the downstream reach (sta 34.835 to sta 80.0). The constant depth at the moving boundaries within the trapezoidal section, \hat{h} , was set to 0.01 ft which was about 4 percent of normal depth. The normal depth and \hat{h} were used to compute the initial mesh width (3.035 ft) within the trapezoidal reach. Average values of the flow conditions in the upper and lower reaches were applied as initial conditions within the transition. The initial computational mesh (figure 6.28a) had 846 nodes and 759 elements. The lateral resolution included 3 elements at the upstream end of the rectangular reach. The mesh contained 5 elements across the rectangular channel immediately upstream of the transition beginning at sta 26.34, across the base of the transition, and across the base of the trapezoidal channel downstream of the transition. Three elements were used across each of the side slopes of the trapezoidal reach from the end of the transition to sta 72.6. At the lower end of the flume, the mesh had 2 elements across each side slope and 3 elements across the base. Additional nodes and elements were added to the downstream end representing a 4.41-ft long gentle transition from a trapezoidal to a rectangular section. The outflow boundary elements represented a rectangular "tailbox"; the side wall nodes at the outflow boundary were fixed.



a. Initial mesh



b. Final mesh

Figure 6.28. Numerical model computational meshes for rectangular-to-trapezoidal transition.

Flow at the inflow boundary was supercritical requiring input of p , q , and h . Since the computational mesh was aligned with the x axis (figure 6.28), values of q for each inflow node were set to zero. The p values at these nodes were set equal to

the flow rate per unit width of channel (total discharge, 3.6 ft³/sec, divided by channel width, 2 ft). As mentioned above, depth at the inflow nodes was set to normal depth. The outflow was supercritical and therefore no boundary conditions were specified. The boundary conditions employed in the rectangular-to-trapezoidal transition are shown in table 6.5 and the model parameters used are listed in table 6.6.

Boundary nodes at the waterline/transition wall intersection on each side of the channel were allowed to move in the direction parallel to the vertical transition walls. As the water surface elevation at this point increased or decreased, the intersection point moved downstream or upstream, respectively. All other side slope boundary nodes were specified to move in the direction of maximum side slope. Each of the nodes within the rectangular reach was fixed.

Table 6.5: Rectangular-to-trapezoidal transition, boundary conditions.

Boundary	Flow Regime	Boundary Condition	Value
Inflow	Supercritical	h	0.280 ft
		p	1.80 ft ² /sec
		q	0.0
Outflow	Supercritical	h	Not Specified
		p	Not Specified
		q	Not Specified

Table 6.6: Rectangular-to-trapezoidal transition, model parameters.

Condition	Value
α	1.0
β	0.1
n	0.009
C_b, v_t	0.1, 0.023 ft ² /sec
\hat{h}	0.01 ft

With these initial conditions, boundary conditions, and nodal movement constraints, 4.0 sec of simulation were run using a time step of 0.05 sec which resulted in a Courant number of 1.3. A time step of 0.1 sec was then used for a total simulation time of 19.0 sec. At this time the mesh was refined such that the grid density upstream, through, and downstream of the transition was increased.

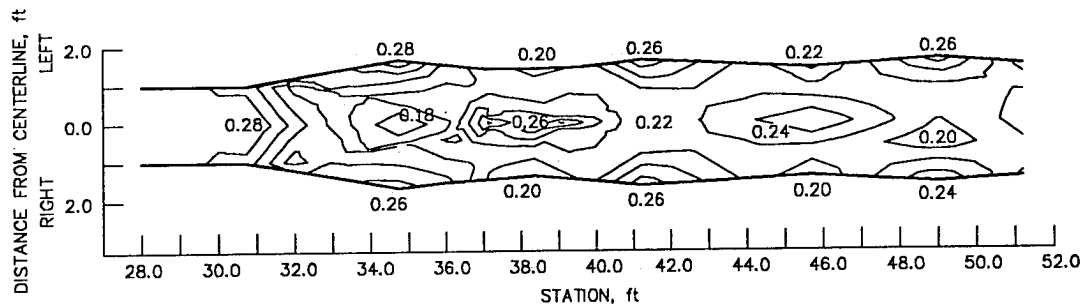
The final grid had 1406 nodes and 1297 elements. The mesh included 7 elements across the rectangular reach immediately upstream of the transition and across the base within the transition, resulting in an element longitudinal-to-transverse aspect ratio of approximately 1.5. Seven elements were used across the base and 4 elements across each side slope from the transition to sta 51.3. The grid was not further refined below sta 51.3. Time steps varying from 0.01 sec to 0.2 sec were used

to simulate a total time of 28.6 sec, the results of which were deemed steady state. The final grid corresponding to the steady state solution, is shown in figure 6.28b. The aspect ratios of the elements located on the side slope varied along the length of the channel in conjunction with the waterline variance (transition detail in figure 6.28b). In the vicinity of maximum flow width, the side slope elements had aspect ratios (longitudinal to lateral) of approximately 3; whereas in regions of minimum flow width the element aspect ratios were about 5. These aspect ratios are appropriate for modeling high-velocity channel flow in rectangular channels (Stockstill and Berger 1994).

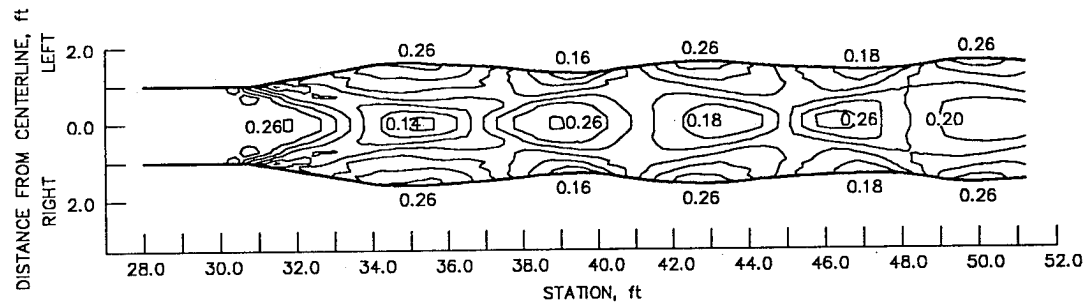
Test Results

Computed water surface elevations are compared with those measured in the laboratory flume by examination of the computed and observed depth contours shown in figure 6.29. These depths are relative to the channel bottom (see figure 6.7). The observed values are interpolations from discrete measurements obtained at a 1.0 ft longitudinal spacing upstream of the transition to as small as 0.5 ft in the vicinity of sta 39. Lateral distances between depth measurements varied from 1.0 ft upstream of the transition (at each wall and on centerline) to 0.07 ft in the vicinity of the standing waves. The model results are further illustrated in the water-surface mesh presented in figure 6.30.

Evaluation of the observed and computed depth contours (figure 6.29), waterlines (figure 6.31), and water-surface profiles (figure 6.32) leads to the conclusion that in this flow situation also there is a phase difference in the computed



a. Flume data



b. Model results

Figure 6.29. Depth contours (feet above channel bottom) for rectangular-to-trapezoidal transition.

and observed wave patterns. The computed location of the first wave peak is slightly downstream of that measured in the flume. This is opposite from the test results for the trapezoidal-to-rectangular transition where the standing waves were contained in the rectangular portion of the channel. This error is probably due to the violation of a combination of model assumptions that the slope is geometrically mild, that the pressure is hydrostatic, and that the velocity is uniformly distributed throughout the fluid column.

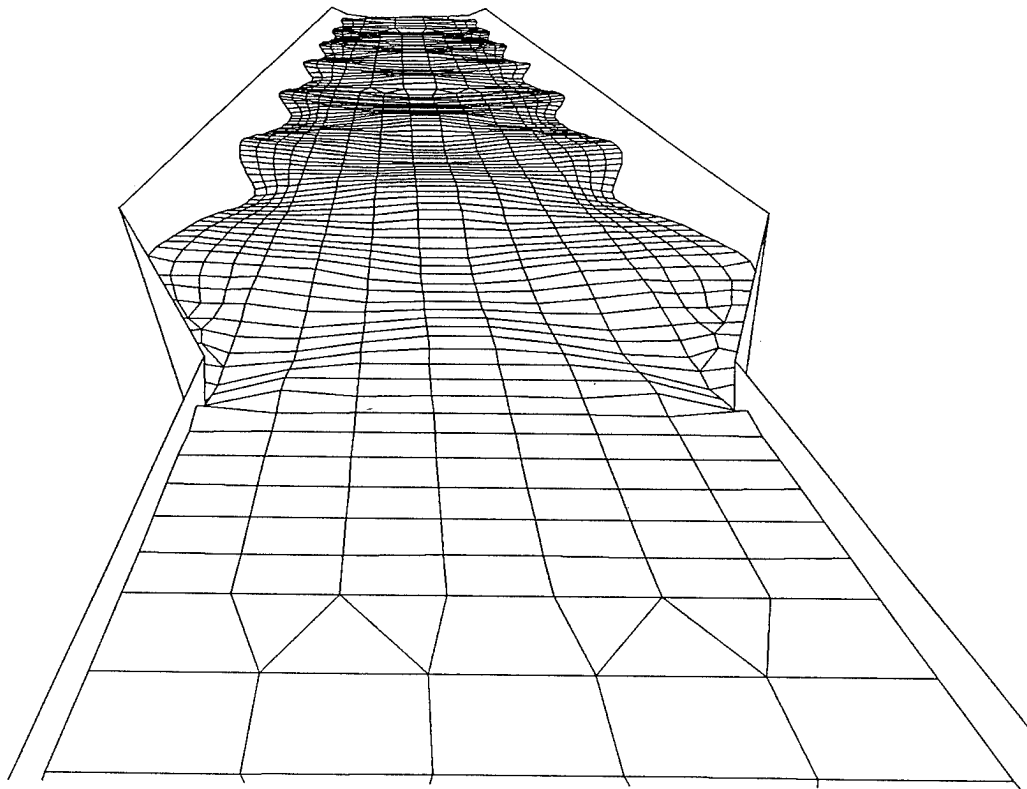


Figure 6.30. Computed water-surface mesh for rectangular-to-trapezoidal transition.

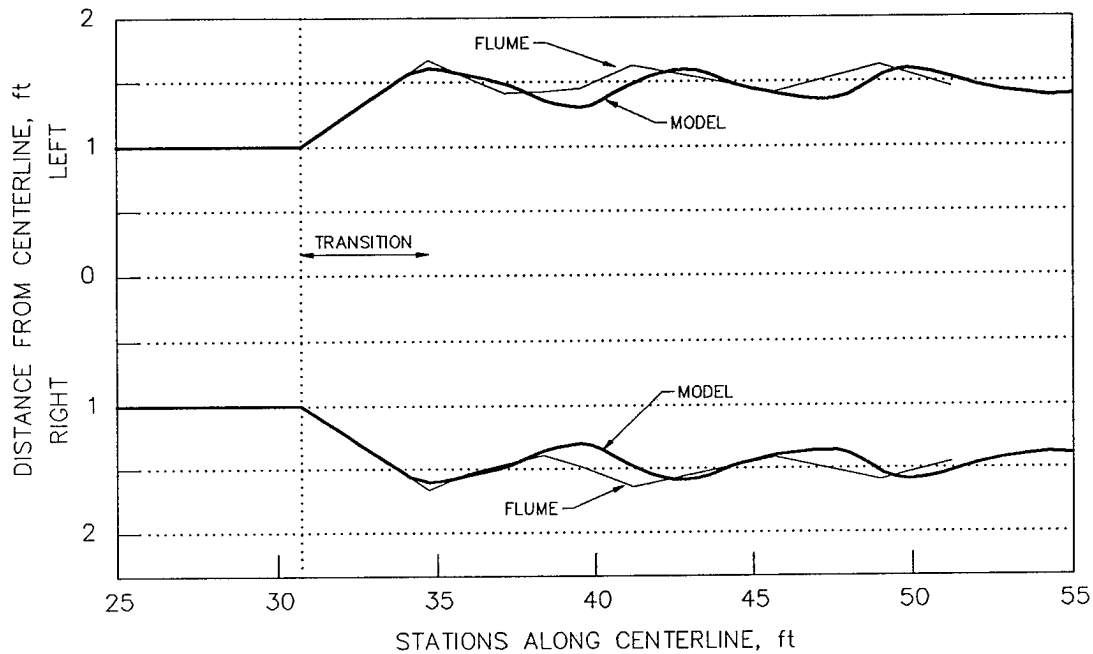
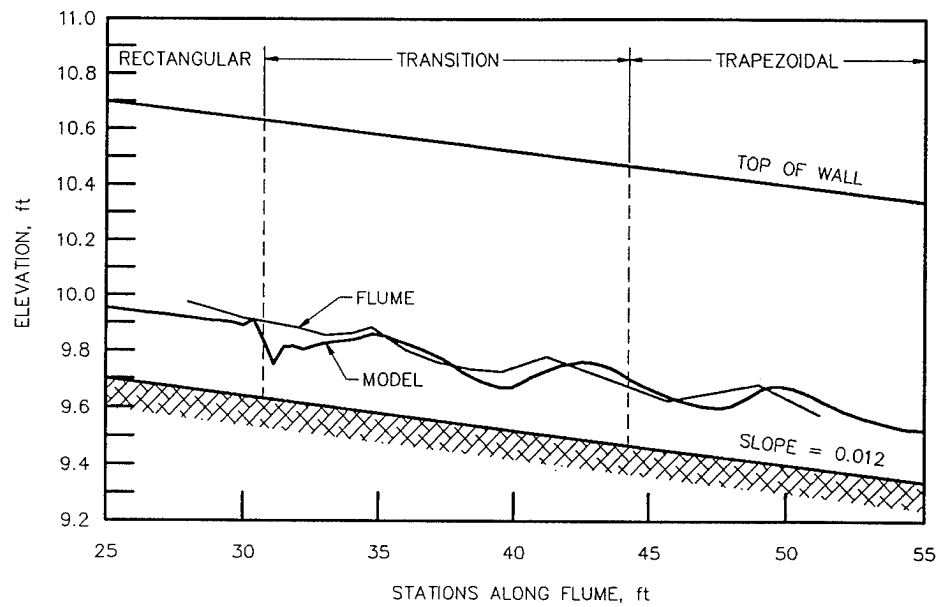
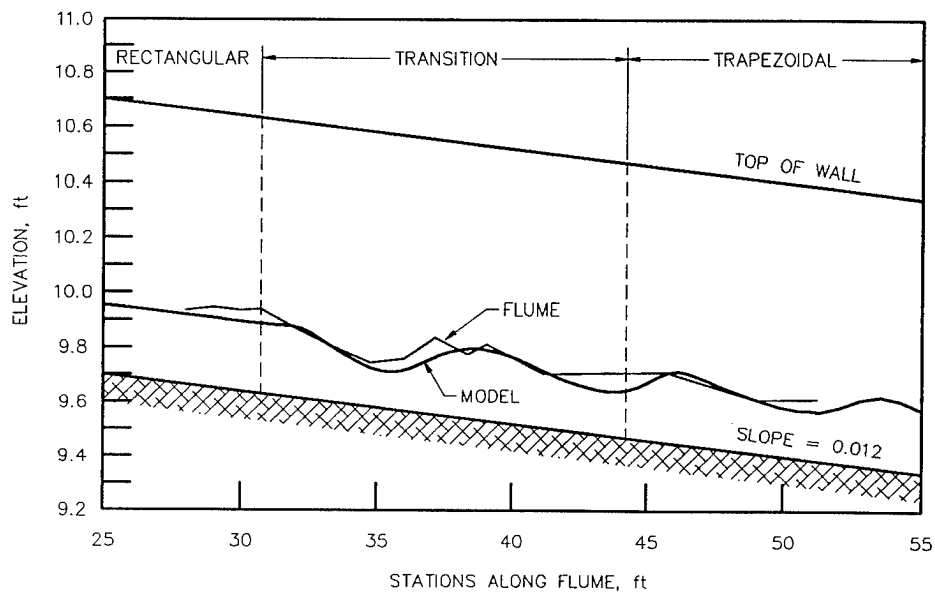


Figure 6.31. Computed and observed side boundaries for rectangular-to-trapezoidal transition.

The computed standing wave phase error may be attributed in part to the depth averaging of velocity assuming a uniform vertical distribution of horizontal velocity. The currents in the rectangular reach of the flume are larger near the surface than near the bed due to boundary drag. A short distance downstream of the vertical wall break, the flow near the surface is directed approximately parallel with the vertical wall while the currents near the slope toe are still generally in the longitudinal direction resulting in secondary currents in this vicinity. There is a significant vertical variation in



a. Profile along left wall



b. Profile along centerline

Figure 6.32. Water-surface profiles for rectangular-to-trapezoidal transition (datum is 10 ft below sta 0 invert elevation).

horizontal velocity throughout the flow near the transition wall, but the depth-averaged model does not account for this vertical variation in velocity. This discrepancy could contribute to the standing wave phase differences between the depth-averaged model and the flume. However, it is difficult to quantify how these velocity errors impact the computed water surface elevation. One can speculate that the depth-averaged velocity given by the model, assuming no vertical variation in horizontal velocity, is faster than that in the real system (flume) near the transition wall. This higher velocity would coincide with a shallower depth, as shown in the water-surface profile along the wall (figure 6.32a). Perhaps the computed momentum of the flow moving up the side slope is excessive resulting in the peak runup occurring too far downstream.

Another possible explanation of model and flume differences is related to the mild-slope assumption employed in the model equations because as the flow expands and contracts, the bed slope for flow near the waterline is significantly steeper than the channel's longitudinal slope. A qualitative assessment of the error introduced by the mild-slope assumption can be made by considering a steep channel in which the flow is nearly parallel to the bed (see figure 6.33). Under these circumstances, the steep-flow equations are a good description of the flow since accelerations normal to the bed are nearly zero, although vertical accelerations may be significant. Insight into solutions given by the mild-slope form of the shallow water equations when applied to steep channels can be obtained by substitution of the mild-slope variables into the steep-slope equations while assuming the steep-slope equations perfectly describe the

flow.

The steady one-dimensional mild-slope equations are

$$\frac{\partial p}{\partial x} = 0 \quad (6.7)$$

and

$$\frac{\partial}{\partial x} \left(\frac{p^2}{h} + \frac{1}{2}gh^2 \right) + gh \frac{\partial z_0}{\partial x} = 0 \quad (6.8)$$

The steep-slope formulation of the shallow water equations are written in terms of the variables depicted in figure 6.33. The steady one-dimensional form of the steep-slope equations are

$$\frac{\partial p'}{\partial x'} = 0 \quad (6.9)$$

and

$$\frac{\partial}{\partial x'} \left(\frac{(p')^2}{d} + \frac{1}{2}gd^2 \cos \zeta \right) + gd \sin \zeta = 0 \quad (6.10)$$

where $p' = u'd$. For constant ζ the steep-slope formulation is written in terms of the mild-slope formulation variables and the resulting equation solved for the water surface slope is given as

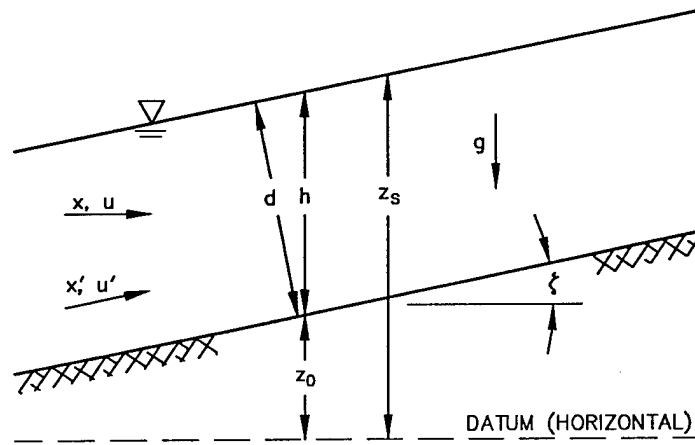


Figure 6.33. Schematic of flow and geometric variables.

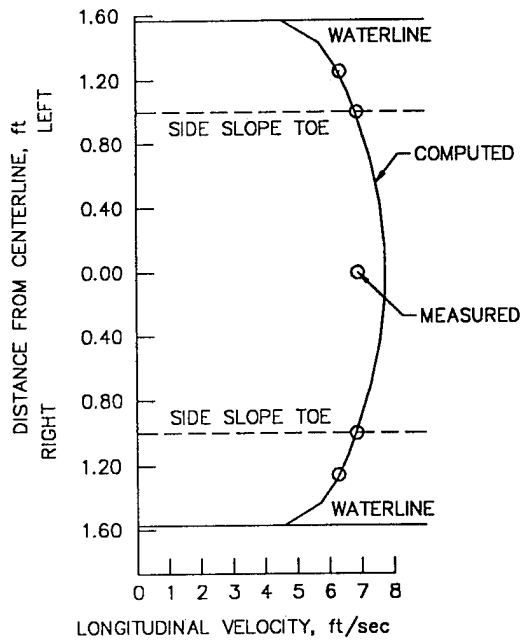
$$\frac{\partial z_s}{\partial x} = \left[1 - \frac{1}{\cos^2 \zeta - \left(\frac{Fr}{\cos \zeta} \right)^2} \right] \frac{\partial z_0}{\partial x} \quad (6.11)$$

Setting $\zeta = 0$ provides the mild-slope solution. As pointed out by Berger (1992), the no slope case seems ambiguous in that $\partial z_0 / \partial x = \tan \zeta$; however, $\partial z_0 / \partial x$ is not among the terms dropped when ζ is assumed to be small. If the flow is supercritical, as found in the rectangular-to-trapezoidal transition test, then $1/(\cos^2 \zeta - (Fr/\cos \zeta)^2)$ is less than unity and the water-surface slope is greater than the bed slope. Equation 6.11 shows that the mild-slope assumption over-estimates the water-surface slope in the case of supercritical flow.

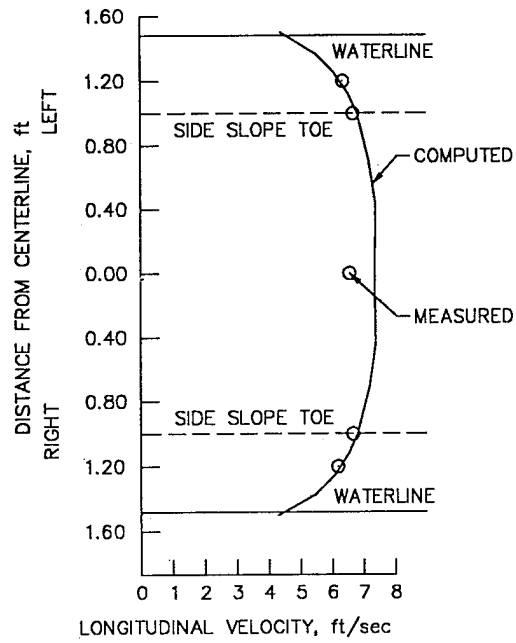
As the flow expands and runs up the steep side slopes in the trapezoidal channel, the mild-slope formulation results in a water-surface slope that is too steep

which produces excessive runup on the side slopes. In the drawdown case as the flow contracts, the mild-slope formulation results in a water-surface slope that again is too steep resulting in excessive drawdown. The errors introduced using the mild-slope formulation in applications to supercritical flow are that on adverse steep slopes the flow depth is too large and the velocity too small and on favorable steep slopes, the flow depth is too small and the velocity is too large. Therefore, the lateral horizontal distance between runup and drawdown given by the model is larger than that observed in the flume. Moreover, since the flow is advected in the longitudinal direction, this error in the lateral direction (runup and drawdown on the side slopes) results in the longitudinal distance between wave peaks being too long. However, the model did capture the general features of the flow and most importantly, from a flood control channel design standpoint, the maximum wave heights.

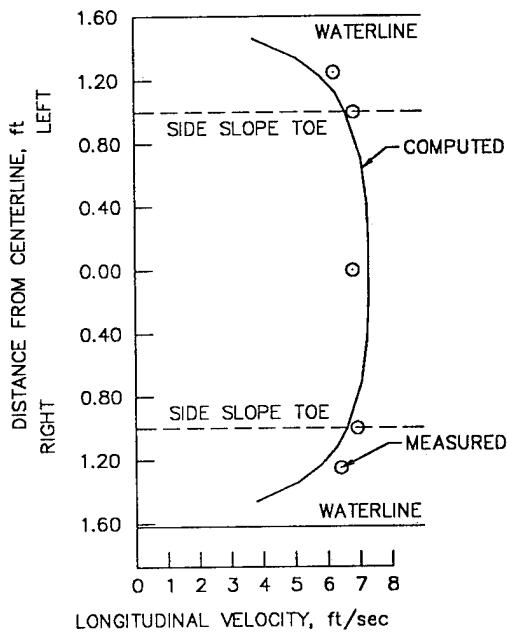
Depth-averaged longitudinal velocity profiles for three stations within the reach of channel having sloping sidewalls are provided on figure 6.34. Each plotted velocity, except those located near the waterline, is the average of three point velocities measured at 17, 50, and 83 percent of the flow depth at a particular station and distance from centerline. At points near the waterline a single measurement of velocity at 60 percent of the flow depth was assumed to represent the depth average. Differences between the model results and the flume data are generally confined to the channel center. The plots suggest that the depth-averaged velocity of the flume flow near the channel center is more uniform across the channel than those predicted by the model. However, generally the velocity comparisons are good.



a. Downstream end of transition, sta 34.1



b. Sta 37.0



c. Sta 41.0

Figure 6.34. Computed and observed depth-averaged velocities for rectangular-to-trapezoidal transition (left and right directions are referenced to looking downstream).

Multiple Flow Obstructions

Three flow obstructions composed of wooden struts were placed in the trapezoidal channel having a base width of 2 ft and 1 vertical on 2.25 horizontal side slopes (figure 6.1), to simulate the conditions resulting from supercritical flow through bridge piers. This test demonstrates the ease with which a finite element grid can be constructed to represent complex geometries such as the bridge piers. The piers were located on the channel base at the left and right toe of the slopes and at the channel centerline. Each strut was 1.0 ft long by 0.1 ft wide having a semicircular nose and tail (radii = 0.05 ft) with the nose of each located at sta 30 (figure 6.35). A dry bed photograph of the piers installed in the flume is provided in figure 6.36.

Test Conditions

Tests were conducted to document the flow conditions resulting from a discharge of $4.0 \text{ ft}^3/\text{sec}$ with the tilting flume (figure 6.1) set at a channel slope of 0.0035. Subsequent to the flume testing, simulations of these flow conditions were conducted to further evaluate the numerical model's abilities.

The initial computational mesh shown on figure 6.37a had 1224 nodes and 1157 elements. The width of the grid was set based on the top width of flow at normal depth in the absence of the flow obstructions. Normal depth (0.35 ft) was computed using a Manning's roughness coefficient n of 0.009 ($Fr = 1.4$). The lateral mesh resolution at the upstream end consisted of 2 elements across each side slope and 3 elements across the base of the trapezoidal section. In the vicinity of the piers, the resolution was increased to 4 elements across each side slope and 7 elements

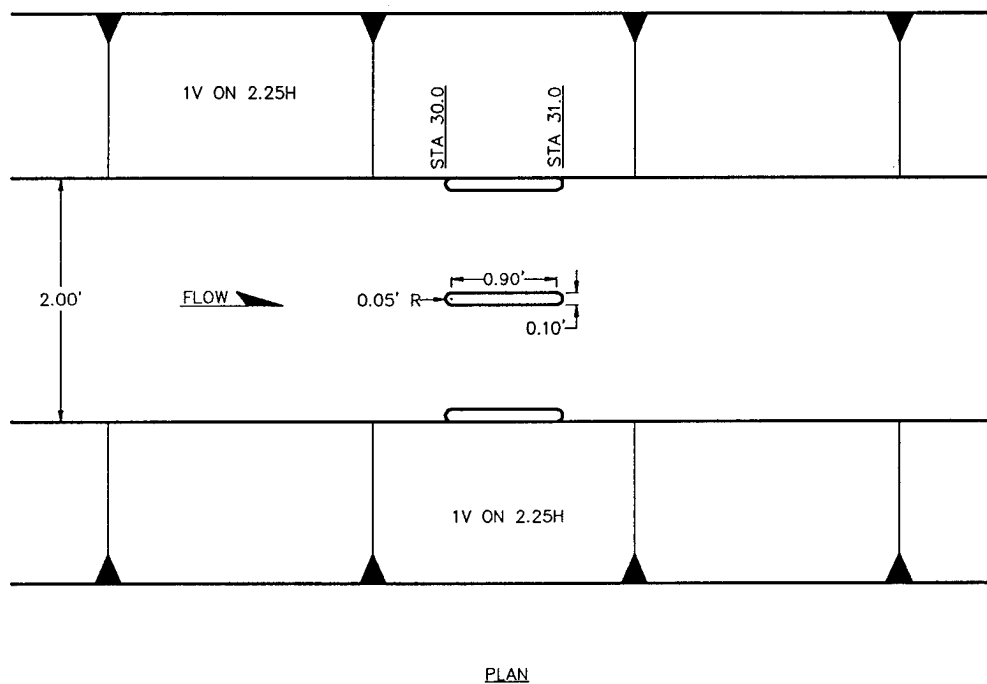


Figure 6.35. Plan view of multiple flow obstructions in the trapezoidal channel.

between each pier. The lower end of the model was represented using 3 elements across each side slope and 4 elements across the base. In a manner similar to the previously reported simulations, the computational mesh was constructed to represent a "headbox" at the inflow boundary and a "tailbox" at the outflow boundary. These nodes and elements that represented fixed rectangular inflow and outflow sections and mild transitions to and from trapezoidal sections were added to the mesh describing the trapezoidal channel. The need to model a moving boundary representing the waterline at the open boundaries was avoided by use of rectangular inflow and outflow sections.

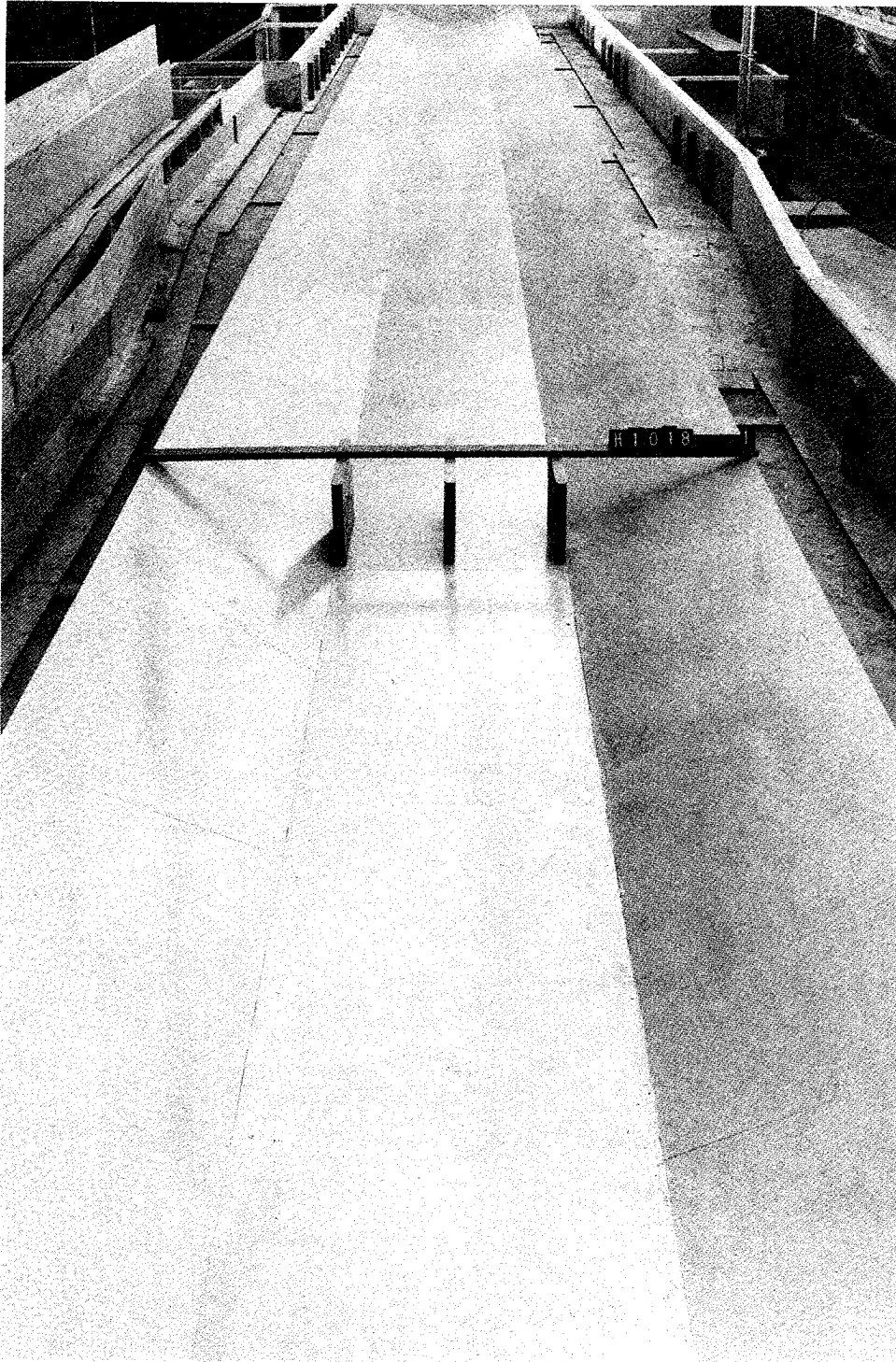
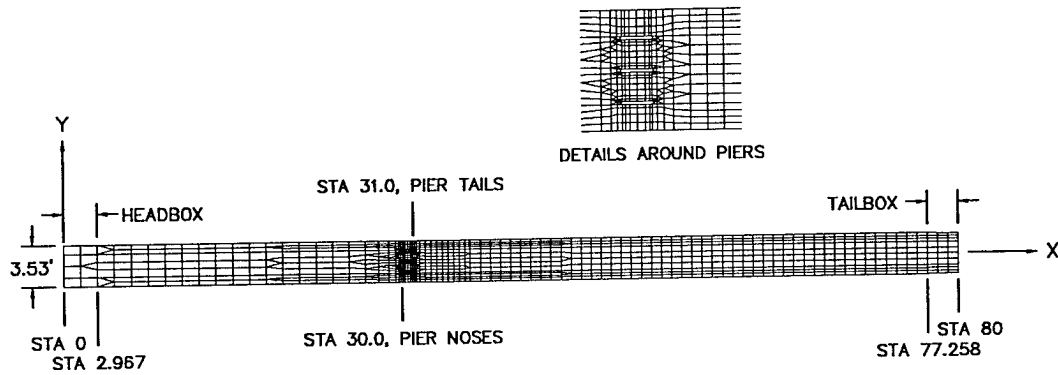
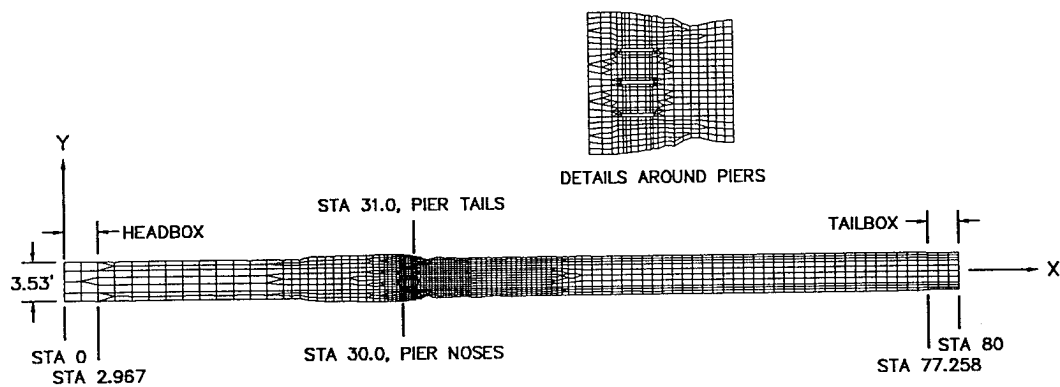


Figure 6.36. Dry bed view of trapezoidal channel with flow obstructions (looking downstream).



a. Initial mesh



b. Final mesh

Figure 6.37. Numerical model computational meshes for trapezoidal channel with flow obstructions.

The inflow was supercritical (Froude number in headbox = 1.2) and therefore required 3 boundary conditions. The grid's x axis was aligned with the channel centerline so that the velocity at the inflow boundary was in the x direction. The value of p at each node was set equal to the unit discharge (total discharge, 4.0 ft³/sec, divided by channel width, 3.53 ft) of 1.133 ft²/sec. The value of q at each inflow node was set to zero. The inflow depth was specified as normal depth. Flow at the outflow boundary was supercritical and required no boundary conditions. The imposed boundary conditions are presented in table 6.7. The sidewall boundary (waterline) nodes were allowed to move in the direction of maximum side slope while maintaining a constant depth (\hat{h}) of 0.01 ft which was less than 3 percent of normal depth. The boundaries describing each pier were fixed, no flux boundaries. Table 6.8 is a listing of the model parameters used in this simulation.

Initial conditions were specified at each node as those given by normal depth flow. The channel centerline was aligned with the grid's x axis and x- and y- directions of velocity were set to 4.0 ft/sec and 0.0 ft/sec, respectively. The flow depth at the channel centerline was set to 0.35 ft such that the water-surface longitudinal profile was parallel to the channel bed profile. With these initial and boundary conditions, simulations were run using time steps varying from 0.01 sec (Courant number of 0.9) to 0.04 sec for a total simulated time of 12.15 sec. The time step was then increased in increments to 0.2 sec for a total simulated time of 67.15 sec. At this time the solution had reached steady state.

Table 6.7: Multiple flow obstructions, boundary conditions.

Boundary	Flow Regime	Boundary Condition	Value
Inflow	Supercritical	h	0.350 ft
		p	1.133 ft ² /sec
		q	0.0
Outflow	Supercritical	h	Not Specified
		p	Not Specified
		q	Not Specified

Table 6.8: Multiple flow obstructions, model parameters.

Condition	Value
α	1.0
β	0.1
n	0.009
C_b, v_t	0.1, 0.016 ft ² /sec
\hat{h}	0.01 ft

The grid was then refined in the vicinity of the obstructions. The density of the grid was increased from immediately upstream of the piers to sta 36.1. The lateral resolution on each of the side slopes adjacent to the piers was increased to 7 elements. The base of the trapezoidal channel downstream of the piers was discretized into 11 elements. The resulting computational mesh had 1852 nodes and 1775 elements. The initial conditions for the denser grid were obtained by interpolation from the steady state solution produced with the original grid using a bilinear interpolation scheme. The steady state solution for the finer mesh was computed using time steps varying from 0.02 sec to 0.1 sec for an additional simulation of 10.4 sec beyond the steady state solution obtained with the original grid. The computational mesh associated with the steady state solution is presented in figure 6.37b.

Test Results

Figure 6.38 shows the flow conditions produced by the three piers. The piers caused a choked flow condition resulting in undulating subcritical flow approaching the piers. The flow accelerated between the obstructions then passed through critical depth which resulted in supercritical flow downstream of the piers. Figure 6.38 shows the multiple oblique standing waves that are generated as the supercritical flow passed around the pier tails. The effects of these standing waves on the shape of the side slope waterlines are also shown on the photograph.

Comparisons are made between the computed and observed flow depths by examination of the depth contours presented in figure 6.39. The depths shown on the contour plots are relative to the channel centerline. The depth contours plotted for the

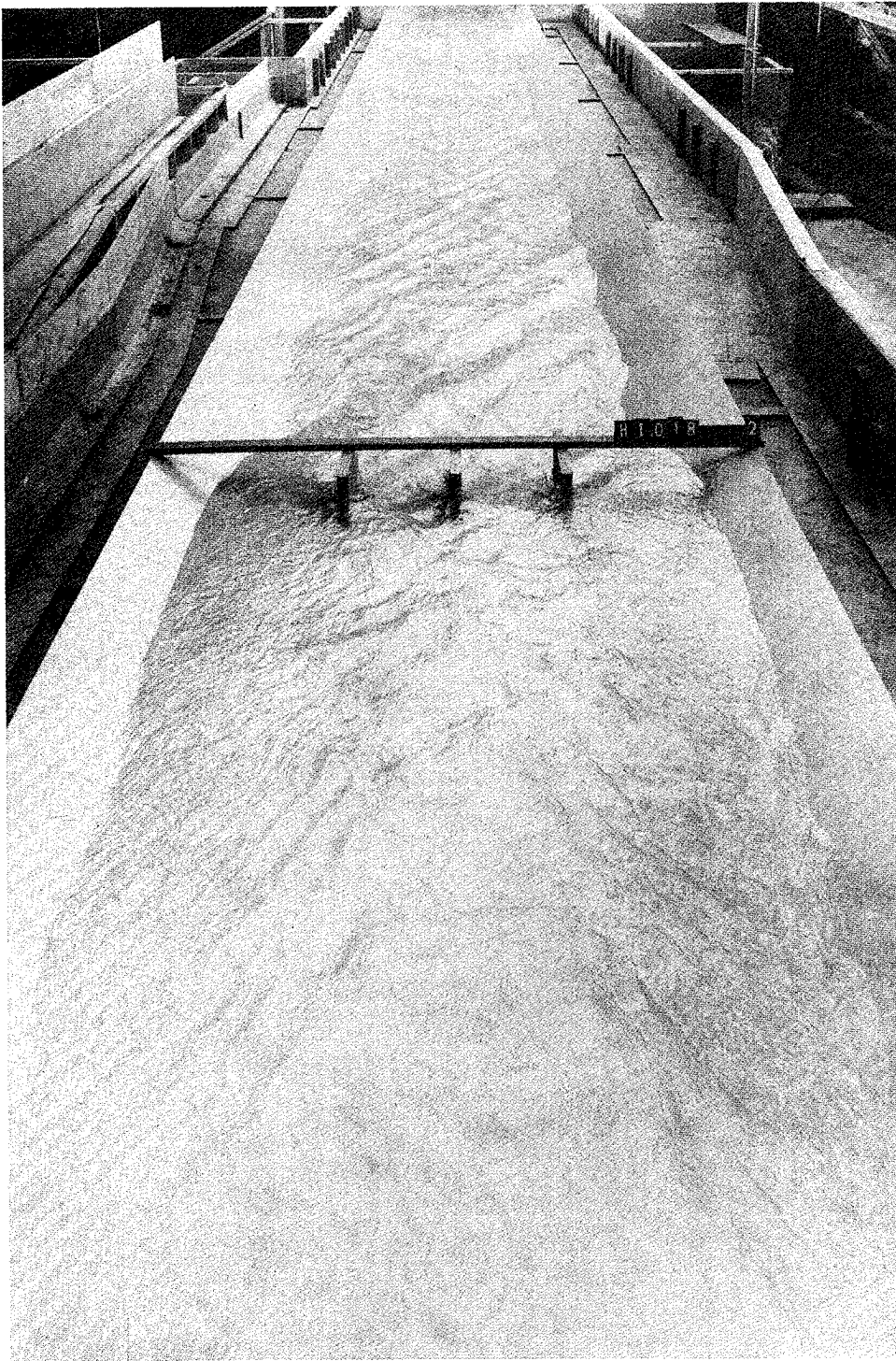
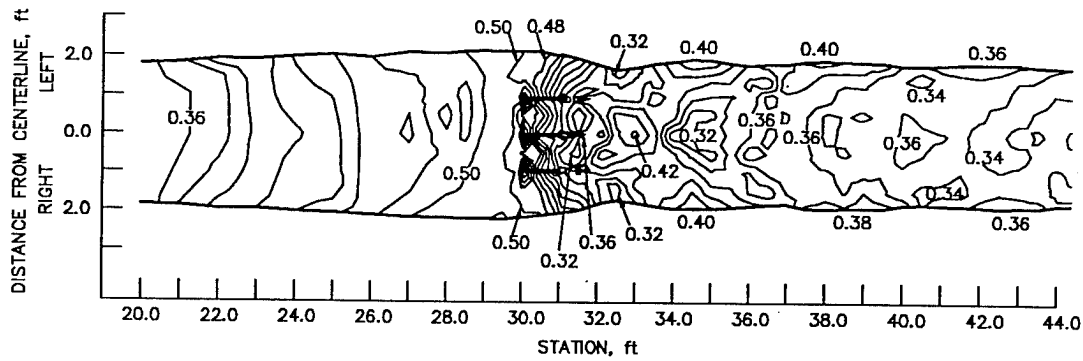
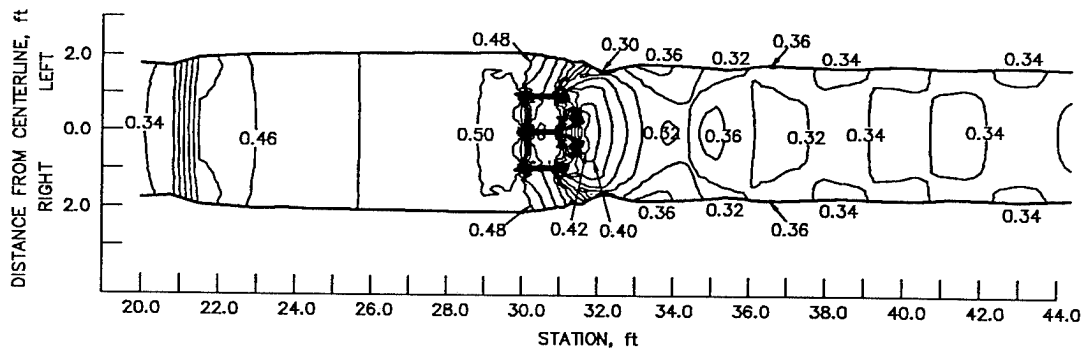


Figure 6.38. Flow conditions in trapezoidal channel with flow obstructions (looking downstream).



a. Flume data



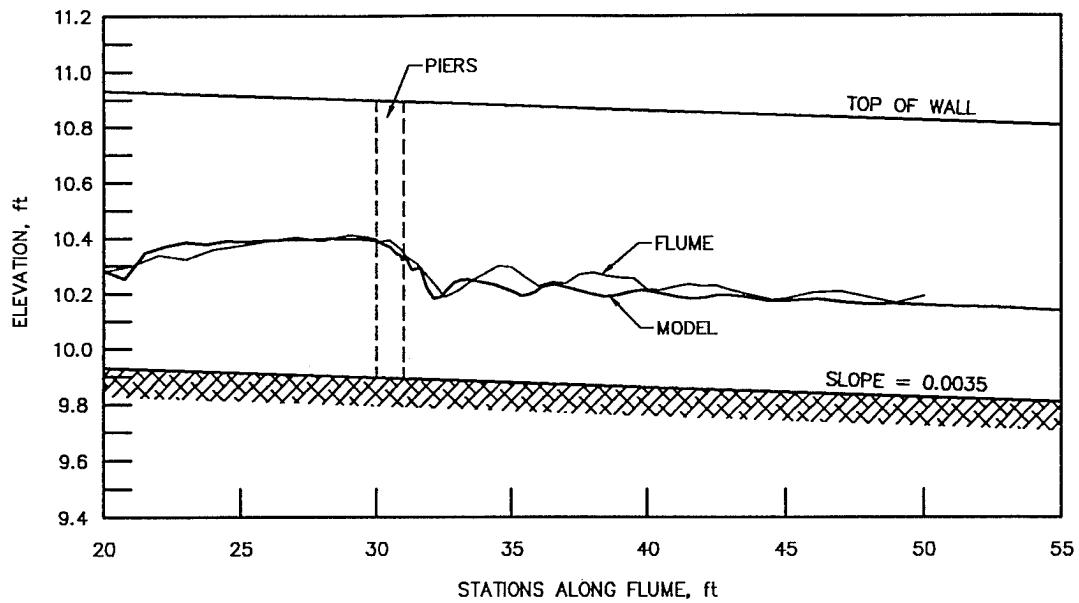
b. Model results

Figure 6.39. Depth contours (feet above channel bottom) for trapezoidal channel with flow obstructions.

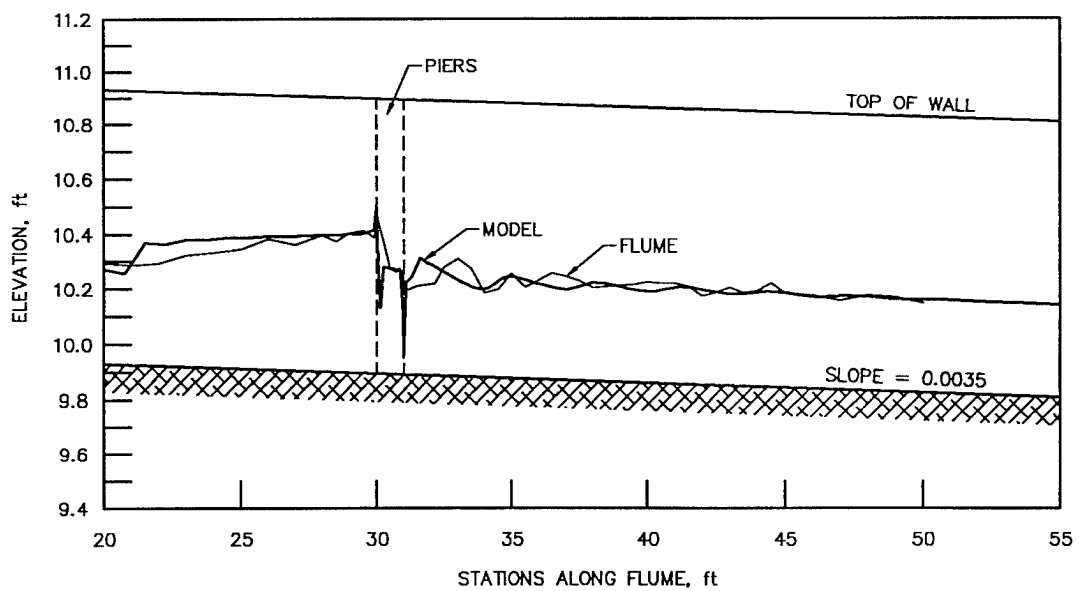
flume data are interpolations of a set of measured flow depths at discrete points. The longitudinal spacing between data points varied from as large as 3 ft at the upstream

end of the plotted reach to 0.14 ft immediately downstream of the piers to 0.5 ft at the downstream end of the plotted reach. Spacing of measurements across a station ranged from 0.5 ft in regions of smooth water surface to 0.08 ft in the vicinity of and just downstream of the piers. Downstream of the piers, rapid fluctuations of the water surface at the waterlines presented a problem in measuring the time-averaged water-surface elevations at these boundaries. Although this error is not quantified, it was greater than the measurement error of waterline locations in the previously reported tests. This laboratory error may explain why the discrepancies between the computed and observed boundaries downstream of the piers are larger for this channel configuration than those previously described. The water-surface profiles provided in figure 6.40 illustrate that the model and laboratory results compare quite well along the centerline but that the waterline in the flume test is consistently higher than the model results. This boundary difference is again illustrated in the plots of side boundaries presented in figure 6.41. Figure 6.42 is the computed water-surface mesh.

Overall features of the flow included the fact that although the channel slope was hydraulically steep and would produce supercritical flow in the absence of the flow obstructions, the obstructions choked the flow. The specific energy at normal flow conditions without the piers was less than that required to convey the flow around the obstructions. This resulted in an increase of specific energy upstream of the obstructions. This rise in depth and decrease in velocity resulted in subcritical flow approaching the obstructions. This phenomenon is commonly referred to as Class B bridge flow (Henderson 1966).



a. Profile along left wall



b. Profile along centerline

Figure 6.40. Water-surface profiles for trapezoidal channel with flow obstructions (datum is 10 ft below sta 0 invert elevation).

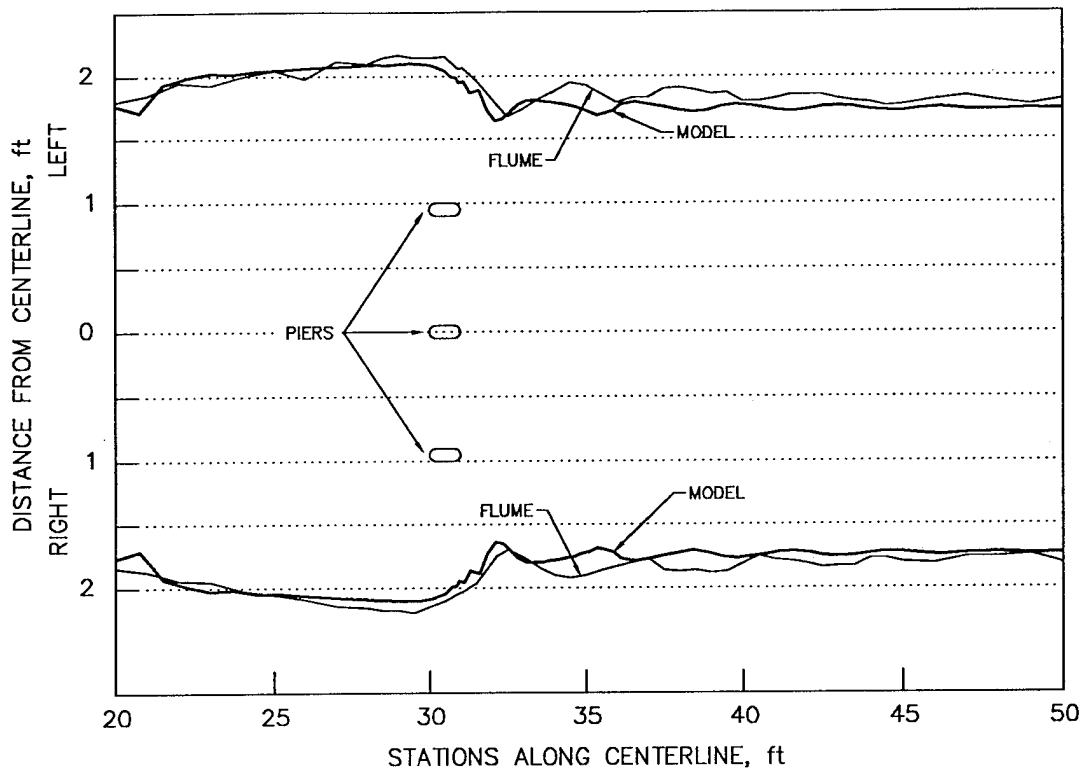


Figure 6.41. Computed and observed side boundaries for trapezoidal channel with flow obstructions.

An undular hydraulic jump formed in the laboratory flume upstream of the obstructions. The flume flow transitioned from supercritical flow near sta 20 to critical flow between sta 23 and sta 24 (critical depth for this configuration and flow rate is 0.42 ft) to subcritical flow at the upstream end of the obstructions. The shallow water equations which do not include vertical accelerations are unable to describe undular jumps. The contour plot in figure 6.39b shows that the numerical model produced a hydraulic jump between sta 21 and sta 22. The contours illustrate a slight

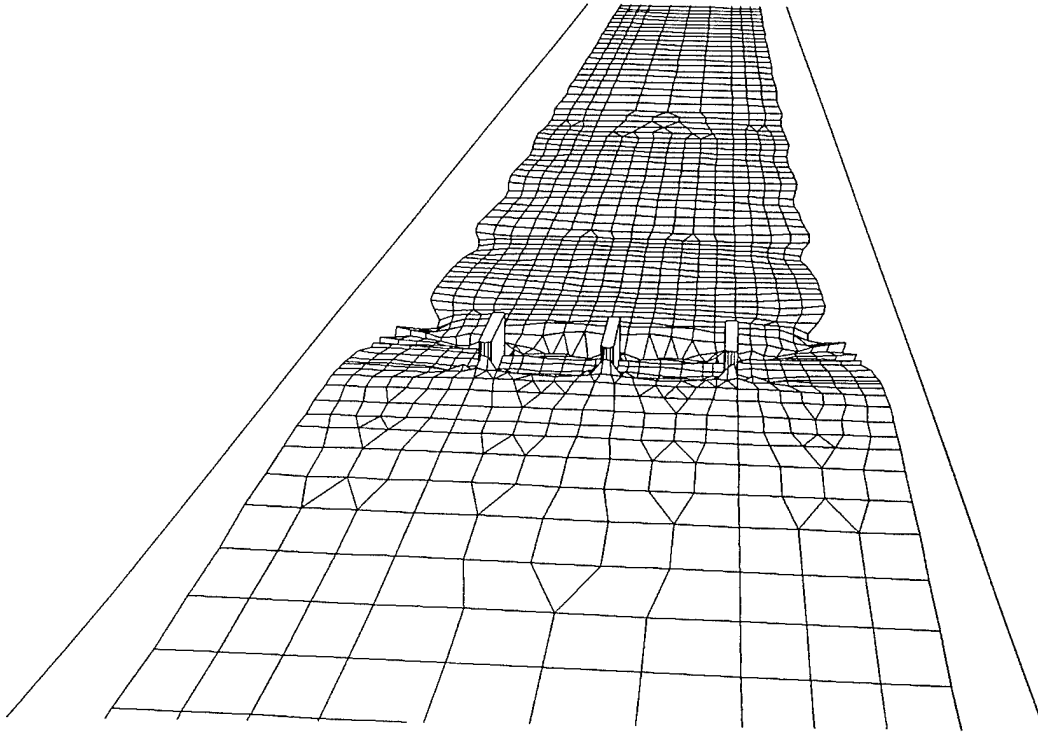


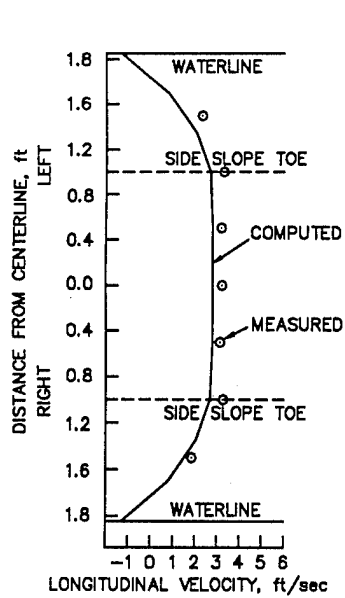
Figure 6.42. Computed water-surface mesh for trapezoidal channel with flow obstructions.

oscillation upstream of the jump. Downstream of the jump, the model reproduced the S_1 longitudinal water-surface profile of the approach flow as was observed in the flume. An S_1 profile is defined as decelerating subcritical flow on a hydraulically steep slope resulting from downstream control (Henderson 1966). Small oscillations of the final grid boundary were noted in the region of rapid flow acceleration just downstream of the piers (figure 6.37b, details around piers). However, these oscillations were confined to this vicinity and did not affect the numerical stability of the simulation. The most important result from an engineering standpoint is that the

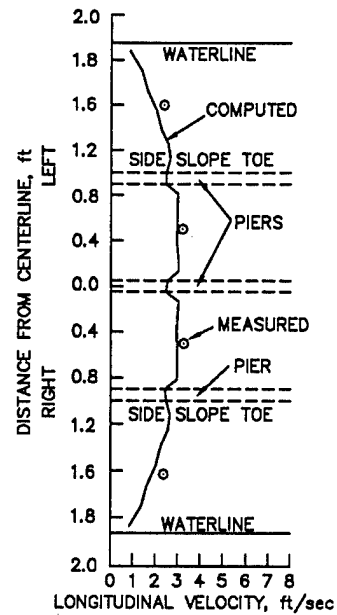
numerical model accurately represented the choked flow condition and the depth of the approaching flow (0.50 ft). Accurate predictions of flow depths are required for sidewall height and minimum bridge soffit elevation determinations.

Computed and observed longitudinal depth-averaged velocities are presented in figure 6.43. Each depth-averaged value plotted for the flume data is an average of three velocity measurements taken at various depths within the flow column except in the shallow regions near the waterlines. Velocities were measured at 17, 50, and 83 percent of the flow depth. Only one velocity at 60 percent of the depth was measured in the areas of shallow flow.

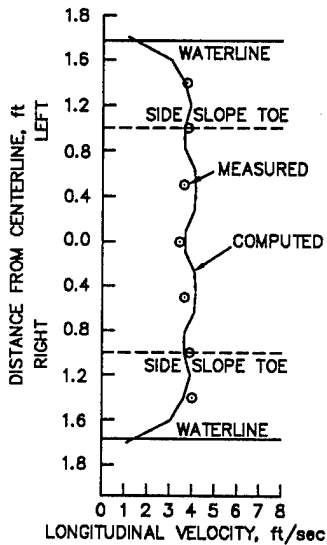
The velocity profiles indicate that the computed flow depth at sta 25.0 is too large and the velocities are too small. This difference is also apparent on the depth contours (figure 6.39). The model results indicate that the flow at the waterline is in the upstream direction. It was observed during laboratory testing that surface currents near the banks of the flume oscillated between the upstream and downstream directions, but the shallow depth at these locations prohibited the measurement of time-averaged velocities. Because the flow is expanding beginning at the hydraulic jump, reverse flow at the water's edge of sta 25.0 is to be expected. Near the end of the pier noses (sta 30.1) and downstream of the piers (sta 33.0) the modeled and measured velocities are in close agreement. In the wake of the piers (sta 33.0) the computed longitudinal velocities vary across the channel, even between the side slope toes. The modeled velocities in the channel center vary between 3.6 ft/sec and 4.2 ft/sec. It is noted that these velocity variations are defined by 5 nodal values and are



a. In the approach flow, sta 25.0



b. Near the pier noses, sta 30.1



c. Downstream of the piers, sta 33.0

Figure 6.43. Computed and observed depth-averaged velocities for trapezoidal channel with flow obstructions (left and right directions are referenced to looking downstream).

not node-to-node oscillations associated with numerical instability.

Discussion of Model Results

The results of the model testing demonstrate that the model can be used as a tool for the evaluation of trapezoidal high-velocity channel designs. The primary design objective of man-made flood control channels is the determination of the lateral and longitudinal variations of the water-surface elevation. The model developed in this dissertation study is sufficiently accurate to serve as a trapezoidal high-velocity channel design and evaluation tool.

The test results also indicate particular flow features of trapezoidal high-velocity channels which the model cannot reproduce. Depth-averaged models (such as the one described in this study) that assume uniform vertical distribution of horizontal velocity are incapable of reproducing the lateral distribution of depth-averaged velocity in channel bends without additional empirical relations (Bernard 1993). The helical flow in the real system results in the maximum depth-averaged velocity at a cross section gradually moving outward beginning with the maximum being located near the inside of the curve at the curve's upstream end. Test results showed that the depth-averaged model's velocity distribution remained constant along the length of the curve; therefore, caution should be used in applying the model results to selection of scour protection material within channel bends. Although the model failed to accurately reproduce the velocity distribution, it did accurately predict the superelevation in the water surface within the channel bend.

Another significant finding of the model testing are the discrepancies between

the computed and observed phases of the standing waves. This was most evident in the two transition cases. In the trapezoidal-to-rectangular transition where the standing waves were confined between the vertical walls of the rectangular reach, the computed oblique angle of the standing waves was too large. This was attributed to the assumed hydrostatic pressure distribution contained in the shallow water equations. However, downstream of the rectangular-to-trapezoidal transition where the standing waves were located within the trapezoidal reach, the peak values of the channel flow width (distance from left waterline to right waterline) trailed those observed in the laboratory flume. This error is probably due to a combination of violations of the geometrically mild slope assumption, the hydrostatic pressure distribution assumption, and the assumption of no vertical variation in velocity. The mild-slope formulation of the shallow water equations over predicts runup and drawdown on the side slopes. This overtravel in the lateral direction also produces standing wave phase errors as the flow is advected in the longitudinal direction.

Hydrostatic models employing the mild slope assumption are not applicable to channels having geometrically steep slopes (greater than about 0.1) such as spillway chutes, crested drop structures, or slope-faced broad-crested weirs. Caution is also given to the determination of sidewall heights in or just downstream of regions containing oblique standing waves. The numerical model results approach uniform flow over a shorter distance than was observed in the laboratory flows. Even with this short coming, the model can be used to identify poor designs. The short transitions tested in this study, which were intentionally designed to produce large standing

waves, are impractical for hydraulic design because the heights of the standing waves were excessive. The model could be used to evaluate refinements of the channel geometry to minimize the disturbance patterns resulting from the transition.

Positive findings of the model testing are that the model accurately computed the maximum flow depths along the sidewalls through the regions of oblique standing waves in the trapezoidal-to-rectangular transition and the rectangular-to-trapezoidal transition. The model also captured the magnitude of the water surface superelevation in the horizontal curve of a trapezoidal channel. The model reproduced the choked flow conditions resulting from the three piers in the trapezoidal channel. Unlike a one-dimensional analysis, the two-dimensional model does not require knowledge of empirical loss coefficients to describe the influence of channel features such as transitions, bends, and bridge piers on the flow regime.

CHAPTER 7

SUMMARY AND CONCLUSIONS

Summary

A two-dimensional numerical flow model for trapezoidal high-velocity channels has been described. The model is designed specifically for simulation of flow in channels having sloping sidewalls in which the depth is an unknown variable in the governing equations and therefore, the plan view of the flow domain is not known a priori. Side boundary locations and initial flow conditions are assumed and solution of the transient shallow water equations is advanced in time until the steady state solution is obtained. As the computed flow field evolves to the steady state, the model adjusts the location of side boundaries with the depth solution.

The shallow water equations modified to account for moving boundary effects are solved numerically using an implicit moving finite element model. The nonlinear equations are solved via a Newton-Raphson iterative technique where the Jacobian consists of derivatives taken not only with respect to the flow variables, as is common in other flow models, but also with respect to displacement of the moving boundary nodes. The test function used which is weighted upstream along characteristics was chosen because of its ability to model both subcritical and supercritical flow and transitions between these regimes.

The numerical model structure and solution scheme were tested against an analytical solution of inviscid shallow water equations applied to flow in a circular V-shaped channel.

The model was then tested by comparing simulation results with measured

laboratory data. The conditions for these tests were supercritical flows in a trapezoidal-to-rectangular transition, in a horizontal bend of a channel having a trapezoidal cross section, in a rectangular-to-trapezoidal transition, and in a trapezoidal channel having flow obstructions geometrically similar to bridge piers.

Conclusions

The proposed numerical model is a viable means of simulating flow conditions in high-velocity channels having sloping sidewalls. This study produced a novel method of determining the flow domain and the flow variables simultaneously. An alternative approach would involve updating the boundary displacement only once at the end of each time step. The boundary displacement in models using this approach is often based on the fluid velocity near the boundary and therefore is not solved simultaneously with the flow depth and velocity. This method may be useful in subcritical flow where the nonlinear terms in the governing equations are small. However, in supercritical flow it is doubtful if this method would remain stable and convergence of the solution of the flow variables and flow domain would be difficult to achieve. To facilitate convergence and to avoid instabilities, the boundary location is included with the flow variables in the Newton-Raphson iteration scheme.

Although the test results indicate the model's inability to reproduce accurately the phases (wave lengths) of oblique standing waves in general and the lateral distribution of depth-averaged velocity in a channel bend, the model was shown to predict accurately the maximum wave heights occurring in supercritical flow within and downstream of transitions, the superelevation of supercritical flow in a horizontal

curve of a trapezoidal channel, and the choked flow condition in the approach to bridge piers located in a trapezoidal channel. These results were obtained without empirical coefficients, such as those used to account for geometric features when analyses are performed using one-dimensional models. The model's ability to accurately reproduce maximum water surface elevations is significant because this is the primary concern to engineers evaluating high-velocity flood control channel designs.

Although the two-dimensional model developed and implemented here is a significant advancement in the numerical modeling of high-velocity channels, it by no means replaces the need for physical models of these hydraulic structures. The model is not capable of reproducing three-dimensional flow phenomena nor does it incorporate an appropriate turbulence model for solution of flow dominated by wall generated turbulence. Such cases are found in channels having a small channel width-to-depth ratio where the wall boundary friction is significantly greater than the bed friction. Though the science of computational fluid dynamics continues rapid advancement, reasons such as these lead hydrodynamicists and aerodynamicists to issue the common cry of "never abandon the laboratory".

Given these limitations, the model developed here can be most effectively used as an engineering tool to screen designs prior to physical laboratory scale modeling, thereby expediting the design optimization process and reducing both the time and cost associated with physical model testing. Also, the model can be beneficial when applied to small projects whose costs do not justify a physical model study.

Recommendations for Additional Research

Development of schemes for including the stress terms in the shallow water equations is an active current area of research. The model described herein could be extended to include a better turbulence closure model. Additionally, the significance of the effective stresses arising from depth averaging of the equations of motion should be investigated, perhaps using two-dimensional momentum correction coefficients. The bed shear stress could be computed using a Darcy-Weisbach formulation for friction rather than the Manning's equation used in this study. The Darcy-Weisbach friction factor, which depends on the Reynolds number and relative roughness of the boundary, could be coded to account for variations throughout the flow field; however, this would require an additional iterative loop since the friction factor and the flow variables are interrelated. Whether these model extensions are warranted for the evaluation of flood control channel designs is unknown.

The standing wave phase error could be reduced using higher order shallow water equations. However, this is not a trivial extension and would necessitate a reformulation of the finite element model. The higher order partial derivatives found in these Boussinesq equations require Hermite polynomial interpolation in which the basis function and its first derivative are continuous rather than Lagrange interpolation used in the present model in which only the basis function is continuous. This would add to the computational effort but computational time is becoming less important.

Because the movement of interior nodes can be specified somewhat arbitrarily, alternative means of moving these nodes could be addressed. Some sort of adaptive

regriidding scheme could be incorporated, resulting in highly refined meshes in areas where large gradients of flow field characteristics, velocities and/or depths, occur.

BIBLIOGRAPHY

- Abbott, M. B. 1979. *Computational Hydraulics, Elements of the Theory of Free Surface Flows*, Pitman Advanced Publishing Limited, London.
- Akanbi, A. A., and Katopodes, N. D. 1988. "Model for Flood Propagation on Initially Dry Land," *Journal of Hydraulic Engineering*, vol. 114, no. 7, pp. 689-706.
- Anderson, D. A., Tannehill, J. C., and Pletcher, R. H. 1984. *Computational Fluid Mechanics and Heat Transfer*, Hemisphere Publishing Corporation, New York, New York.
- Anderson, M. P., and Woessner, W. W. 1992. *Applied Groundwater Modeling, Simulation of Flow and Advective Transport*, Academic Press, San Diego, California, pp. 321-324.
- Baines, M. J. 1994. *Moving Finite Elements*, Oxford University Press, New York, New York.
- Berger, R. C., Jr. 1992. "Free-Surface Flow Over Curved Surfaces," Ph.D. Dissertation, University of Texas at Austin, Austin, Texas.
- Berger, R. C., Jr. 1993. "A Finite Element Scheme for Shock Capturing," Technical Report TR-93-12, US Army Engineer Waterways Experiment Station, Vicksburg, Mississippi.
- Berger, R. C., and Stockstill, R. L. 1993. "A 2-D Numerical Model for High Velocity Channels" *Proceedings of the 1993 National Conference on Hydraulic Engineering*, American Society of Civil Engineers, San Francisco, California, edited by H. W. Shen, S. T. Su, and F. Wen, pp. 1085-1090.
- Berger, R. C., and Stockstill, R. L. 1994. "Considerations in 2-D Modeling of Hydraulically Steep Flow" *Proceedings of the 1994 National Conference on Hydraulic Engineering*, American Society of Civil Engineers, Buffalo, New York, edited by G. V. Cotroneo and R. R. Rumer, pp. 1285-1289.
- Bernard, R. S. 1993. "STREMR: Numerical Model for Depth-Averaged Incompressible Flow," Technical Report REMR-HY-11, US Army Engineer Waterways Experiment Station, Vicksburg, Mississippi.
- Bettess, P., and Bettess, J. A. 1983. "Analysis of Free Surface Flows Using Isoparametric Finite Elements," *International Journal for Numerical Methods in Engineering*, vol. 19, pp. 1675-1689.
- Betts, P. L. 1978. "Computation of Stationary Water Waves Downstream of a Two-Dimensional Contraction," *Finite Elements in Water Resources*, Proceedings of the

Second International Conference on Finite Elements in Water Resources held at Imperial College, London, edited by C. A. Brebbia, W. G. Gray, and G. F. Pinder, Pentech Press Limited, London, pp. 2.177-2.193.

Betts, P. L., and Hall, B. L. 1978. "A Finite Element Study of Large Amplitude Water Waves," *Finite Elements in Water Resources*, Proceedings of the Second International Conference on Finite Elements in Water Resources held at Imperial College, London, edited by C. A. Brebbia, W. G. Gray, and G. F. Pinder, Pentech Press Limited, London, pp. 4.147-4.163.

Bhallamudi, S. M., and Chaudhry, M. H. 1992. "Computation of Flows in Open-Channel Transitions," *Journal of Hydraulic Research*, vol. 30, no. 1, pp. 77-93.

Brater, E. F., and King, H. W. 1976. *Handbook of Hydraulics*, McGraw-Hill Book Company.

Brigham Young University 1993. "FastTABS 2.2 MS-Windows Version," Engineering Computer Graphics Laboratory, Brigham Young University, Provo, Utah.

Chapman, R. S., and Kuo, C. Y. 1985. "Application of the Two-Equation $k-\epsilon$ Turbulence Model to a Two-Dimensional Steady, Free Surface Flow Problem with Separation," *International Journal for Numerical Methods in Fluids*, vol. 5, pp. 257-268.

Chippada, S., Ramaswamy, B., and Wheeler, M. F. 1994. "Numerical Simulation of Hydraulic Jump," *International Journal for Numerical Methods in Engineering*, vol. 37, pp. 1381-1397.

Christodoulou, K. N., and Scriven, L. E. 1989. "The Fluid Mechanics of Slide Coating," *Journal of Fluid Mechanics*, vol. 208, pp. 321-354.

Diersch, H. J., and Martin, H. 1978. "The Numerical Treatment of Free Surface Flows by Finite Elements," *Finite Elements in Water Resources*, Proceedings of the Second International Conference on Finite Elements in Water Resources held at Imperial College, London, edited by C. A. Brebbia, W. G. Gray, and G. F. Pinder, Pentech Press Limited, London, pp. 3.97-3.115.

Drolet, J. and Gray, W. G. 1988. "On the Well Posedness of Some Wave Formulations of the Shallow Water Equations," *Advances in Water Resources*, vol. 11, June, pp. 84-91.

Elliot, R., and Chaudhry, M. H. 1992. "A Wave Propagation Model for Two-Dimensional Dam-Break Flows," *Journal of Hydraulic Research*, vol. 20, no. 4, pp. 467-483.

Fennema, R. J., and Chaudhry, M. H. 1989. "Implicit Methods for Two-Dimensional Unsteady Free-Surface Flows," *Journal of Hydraulic Research*, vol. 27, no. 3, pp. 321-331.

Fennema, R. J., and Chaudhry, M. H. 1990. "Explicit Methods for 2-D Transient Free-Surface Flows," *Journal of the Hydraulics Division, Proceedings of the American Society of Civil Engineers*, vol. 116, no. 8, pp. 1013-1034.

Finn, W. D. Liam, and Varoglu, E. 1976. "Variable Domain Finite Element Analysis of Free Surface Flow Problems," *Finite Elements in Water Resources*, Proceedings of the First International Conference on Finite Elements in Water Resources held at Princeton University, edited by W. G. Gray, G. F. Pinder, and C. A. Brebbia, July, pp. 3.115-3.131.

France, P. W. 1980. "A Simple Technique for the Analysis of Free Surface Flow Problems," *Finite Elements in Water Resources*, Proceedings of the Third International Conference on Finite Elements in Water Resources held at the University of Mississippi, University, Mississippi, edited by S. Y. Wang, C. V. Alonso, C. A. Brebbia, W. G. Gray, and G. F. Pinder, University of Mississippi School of Engineering, University, Mississippi, pp. 5.20-5.27.

Hager, W. H., Schwalt, M., Jimenez, O., and Chaudhry, M. H. 1994. "Supercritical Flow Near an Abrupt Wall Deflection," *Journal of Hydraulic Research*, vol. 32, no. 1, pp. 103-118.

Henderson, F. M. 1966. *Open Channel Flow*, Macmillan Publishing Company, New York, New York.

Holz, K. P., and Nitsche, G. 1980. "Tidal Wave Analysis for Estuaries with Intertidal Flats," *Finite Elements in Water Resources*, Proceedings of the Third International Conference on Finite Elements in Water Resources held at the University of Mississippi, University, Mississippi, edited by S. Y. Wang, C. V. Alonso, C. A. Brebbia, W. G. Gray, and G. F. Pinder, University of Mississippi School of Engineering, University, Mississippi, pp. 5.113-5.126.

Holz, K. P., and Withum, D. 1977. "Finite Element applications for Transient Processes in Estuaries," *Formulations and Computational Algorithms in Finite Element Analysis: U. S. - Germany Symposium*, held at Massachusetts Institute of Technology, edited by K. J. Bathe, J. T. Oden, and W. Wunderlich, Massachusetts Institute of Technology, Cambridge, Massachusetts, pp. 917-957.

Hughes, T. J. R., and Brooks, A. 1982. "A Theoretical Framework for Petrov-Galerkin Methods with Discontinuous Weighting Functions: Application to the Streamline-Upwind Procedure," *Finite Elements in Fluids*, edited by R. H. Gallagher, D. H.

Norrie, J. T. Oden, and O. C. Zienkiewicz, vol. 4, John Wiley and Sons, London, pp. 47-65.

Ikegawa, M., and Washizu, K. 1973. "Finite Element Method Applied to Analysis of Flow Over a Spillway Crest," *International Journal for Numerical Methods in Engineering*, vol. 6, pp. 179-189.

Ippen, A. T. 1951. "Mechanics of Supercritical Flow," *Transactions of the American Society of Civil Engineers*, vol. 116, pp. 268-295.

Ippen, A. T., and Dawson, J. H. 1951. "Design of Channel Contractions," *Transactions of the American Society of Civil Engineers*, vol. 116, pp. 326-346.

Jimenez, O. F., and Chaudhry, M. H. 1988. "Computation of Supercritical Free-Surface Flows," *Journal of the Hydraulic Engineering*, vol. 114, no. 4, pp. 377-395.

Katopodes, N. D. 1984. "A Dissipative Galerkin Scheme for Open-Channel Flow," *Journal of Hydraulic Engineering*, vol. 110, no. 4, pp. 450-466.

Katopodes, N. D. 1984. "Two-Dimensional Surges and Shocks in Open Channels," *Journal of Hydraulic Engineering*, vol. 110, no. 6, pp. 794-812.

Kawahara, M., and Umetsu, T. 1986. "Finite Element Method for Moving Boundary Problems in River Flow," *International Journal for Numerical Methods in Fluids*, vol. 6, pp. 365-386.

Kistler, S. F., and Scriven, L. E. 1984. "Coating Flow Theory by Finite Element and Asymptotic Analysis of the Navier-Stokes System," *International Journal for Numerical Methods in Fluids*, vol. 4, pp. 207-229.

Knapp, R. T. 1951. "Design of Channel Curves for Supercritical Flow," *Transactions of the American Society of Civil Engineers*, vol. 116, pp. 296-325.

Kuipers, J. Vreugdenhil, C. B. 1973. "Calculations of Two-Dimensional Horizontal Flow," Report S163, Part I, Delft Hydraulics Lab, Delft, The Netherlands.

Lamb, H. 1945. *Hydrodynamics*, 6th edition, Dover Publications Incorporated, New York, New York.

Lan, T. H., Huttom, A. G., and Loveless, J. H. 1992. "Finite Element Modelling of Moving Boundary Problems in Estuaries and Coastal Waters," *Computer Modelling of Seas and Coastal Regions*, International Conference on Computer Modelling of Seas and Coastal Regions and Boundary Elements and Fluid Dynamics, Southampton, U. K., edited by P. W. Partridge, Computational Mechanics Publications, Southampton,

U. K., pp. 243-254.

Leclerc, M., Bellemare, J., Dumas, G., and Dhatt, G. 1990. "A Finite Element Model of Estuarine and River Flows with Moving Boundaries," *Advances in Water Resources*, vol. 13, no. 4, pp. 158-168.

Leendertse, J. J. 1970. "A Water-Quality Simulation Model for Well-Mixed Estuaries and Coastal Seas: Volume 1. Principles of Computation," Memorandum RM-6230-RC, The Rand Corporation, Santa Monica, California.

Liggett, J. A. 1975. "Basic Equations of Unsteady Flow," *Unsteady Flow in Open Channels, Volume 1*, edited by K. Mahmood and V. Yevjevich, Water Resources Publications, Fort Collins, Colorado, pp. 29-62.

Lynch, D. R. 1982. "Unified Approach to Simulation on Deforming Elements with Application to Phase Change Problems," *Journal of Computational Physics*, vol. 47, pp. 387-411.

Lynch, D. R., and Gray, W. G. 1980. "Finite Element Simulation of Flow in Deforming Regions," *Journal of Computational Physics*, vol. 36, pp. 135-153.

Lynch, D. R., and Gray, W. G. 1978. "Finite Element Simulation of Shallow Water Problems with Moving Boundaries," *Finite Elements in Water Resources*, Proceedings of the Second International Conference on Finite Elements in Water Resources held at Imperial College, London, edited by C. A. Brebbia, W. G. Gray, and G. F. Pinder, Pentech Press Limited, London, pp. 2.23-2.42.

Lynch, D. R., and O'Neill K. 1981. "Continuously Deforming Finite Elements for the Solution of Parabolic Problems With and Without Phase Change," *International Journal for Numerical Methods in Engineering*, vol. 17, pp. 81-96.

MacKinnon, R. J., and Carey, G. F. 1993. "Moving-Grid Finite Element Modeling of Thermal Ablation and Consolidation in Porous Media," *International Journal for Numerical Methods in Engineering*, vol. 36, pp. 717-744.

McCorquodale, J. A., and Li, C. Y. 1971. "Finite Element Analysis of Sluice Gate Flow," *Transactions of the Engineering Institute of Canada*, vol. 14.

McLay, R. T. 1988. "Finite Element Simulation of Coupled Fluid Flow, Heat Transfer and Magnetic Fields with Applications to Welding," Ph.D. Dissertation, University of Texas at Austin, Austin, Texas.

Miller, K. 1981. "Moving Finite Elements. II," *SIAM Journal of Numerical Analysis*, vol. 18, no. 6, pp. 1033-1057.

- Miller, K., and Miller, R. N. 1981. "Moving Finite Elements. I," *SIAM Journal of Numerical Analysis*, vol. 18, no. 6, pp. 1019-1032.
- Molls, T. R. 1992. "A General Two-Dimensional Free-Surface Flow Model for Solving the Depth-Averaged Equations Using an Implicit ADI Scheme," Ph.D. Dissertation, Washington State University, Pullman, Washington.
- Neuman, S. P., and Witherspoon, P. A. 1971. "Analysis of Nonsteady Flow with a Free Surface Using the Finite Element Method," *Water Resources Research*, vol. 7, no. 3, pp. 611-623.
- Okamoto, T., Kawahara, M., Ioki, N., and Nagaoka, H. 1992. "Two-Dimensional Wave Run-Up Analysis by Selective Lumping Finite Element Method," *International Journal for Numerical Methods in Fluids*, vol. 14, pp. 1219-1243.
- Olsen, M. D. 1974. "Variational-Finite Element Methods for Two-Dimensional and Axisymmetric Navier-Stokes Equations," *Finite Element Methods in Flow Problems*, edited by J.T. Oden, O.C. Zienkiewicz, R.H. Gallagher, and C. Taylor, UAH Press, Huntsville, Alabama, pp. 103-106.
- Peregrine, D. H. 1967. "Long Waves on a Beach," *Journal of Fluid Mechanics*, vol. 27, part 4, pp. 815-827.
- Pinder, G. F. and Gray, W. G. 1977. *Finite Element Simulation in Surface and Subsurface Hydrology*, Academic Press Incorporated, San Diego, California.
- Praagman, N. 1979. *Numerical Solution of the Shallow Water Equations by a Finite Element Method*, EGNER, Den Helder, The Netherlands.
- Ramaswamy, B. and Kawahara, M. 1987. "Arbitrary Lagrangian-Eulerian Finite Element Method for Unsteady, Convective, Incompressible Viscous Free Surface Fluid Flow," *Finite Elements in Fluids*, edited by R. H. Gallagher, R. Glowinski, P. M. Gresho, J. T. Oden, and O. C. Zienkiewicz, vol. 7, John Wiley and Sons Limited, pp. 65-87.
- Reid, R. O. and Bodine, B. R. 1968. "Numerical Model for Storm Surges in Galveston Bay," *Journal of the Waterways and Harbors Division, Proceedings of the American Society of Civil Engineering*, vol. 94, no. WW1, pp. 33-57.
- Rodi, W. 1980. "Turbulence Models and Their Application in Hydraulics - A State of the Art Review," State-of-the-Art Paper, International Association for Hydraulic Research, Delft, The Netherlands.
- Rouse, H. 1961. *Fluid Mechanics for Hydraulic Engineers*, Dover Publications

Incorporated, New York, New York.

Rouse, H., Bhoota, B. V., and Hsu, E. 1951. "Design of Channel Expansions," *Transactions of the American Society of Civil Engineers*, vol. 116, pp. 347-363.

Siden G. L. D., and Lynch D. R. 1988. "Wave Equation Hydrodynamics on Deforming Elements," *International Journal for Numerical Methods in Fluids*, vol. 8, pp. 1071-1093.

Stockstill, R. L., and Berger, R. C. 1994. "HIVEL2D: A Two-Dimensional Flow Model for High-Velocity Channels," Technical Report REMR-HY-12, US Army Engineer Waterways Experiment Station, Vicksburg, Mississippi.

Takizawa, A., Koshizuka, S., and Kondo, S. 1992. "Generalization of Physical Component Boundary Fitted Co-ordinate (PCBFC) Method for the Analysis of Free-Surface Flow," *International Journal for Numerical Methods in Fluids*, vol. 15, pp. 1213-1237.

US Army Engineer District, Los Angeles 1939. "Report on Engineering Aspects, Flood of March, 1938; Appendix I, Theoretical and Observed Bridge Pier Losses," Los Angeles, California.

US Army, Office, Chief of Engineers. 1991. *Hydraulic Design of Flood Control Channels*, Engineer Manual No. 1110-2-1601, Washington, D.C.

US Bureau of Reclamation 1967. "General Design Information for Structures," Chapter 2, *Canals and Related Structures*, Design Standards No. 3, US Department of the Interior, Denver, Colorado.

Verboom, G. K., Stelling, G. S., and Officier, M. J. 1982. "Boundary Conditions for the Shallow Water Equations," *Engineering Applications of Computational Hydraulics*, edited by M. B. Abbott and J. A. Cunge, vol. 1, Chapter 11, Pitman Publishing, Marshfield, Massachusetts, pp. 230-262.

Wang, S. P., and Wang, K. K. 1994. "A Net Inflow Method for Incompressible Viscous Flow with Moving Free Surface," *International Journal for Numerical Methods in Fluids*, vol. 18, pp. 669-694.

Washizu, K., Nakayama, T., and Ikegawa, M. 1976. "Application of the Finite Element Method to Some Free Surface Fluid Problems," *Finite Elements in Water Resources*, Proceedings of the Second International Conference on Finite Elements in Water Resources held at Imperial College, London, edited by C. A. Brebbia, W. G. Gray, and G. F. Pinder, Pentech Press Limited, London, pp. 4.247-4.266.

Woodward, S. M., and Posey, C. J. 1941. *Hydraulics of Steady Flow in Open Channels*, Wiley and Sons, New York, New York, p. 112.

Yoo, J., and Rubinsky, B. 1986. "A Finite Element Method for the Study of Solidification Processes in the Presence of Natural Convection," *International Journal for Numerical Methods in Engineering*, vol. 23, pp. 1785-1805.

Younus, M, and Chaudhry, M. H. 1994. "A Depth-Averaged κ - ϵ Turbulence Model for the Computation of Free-Surface Flow," *Journal of Hydraulic Research*, vol. 32, no. 3, pp. 415-444.

APPENDIX A

NEWTON-RAPHSON JACOBIAN TERMS FOR MOVING FINITE ELEMENTS

The Newton-Raphson iterative procedure consists of solving the linear system of equations

$$\frac{\partial \mathbf{R}_i^k}{\partial \mathbf{L}_j^k} \Delta \mathbf{L}_j^k = -\mathbf{R}_i^k \quad (\text{A.1})$$

for $\Delta \mathbf{L}_j^k$ and then an improved estimate for \mathbf{L}_j^{k+1} is obtained from

$$\mathbf{L}_j^{k+1} = \mathbf{L}_j^k + \Delta \mathbf{L}_j^k. \quad (\text{A.2})$$

Here k is the iteration number, j is the node location, and

$$\mathbf{L}_j = \begin{cases} \begin{Bmatrix} h_j \\ p_j \\ q_j \end{Bmatrix} & \text{if node } j \text{ is an interior node} \\ \begin{Bmatrix} s_j \\ p_j \\ q_j \end{Bmatrix} & \text{if node } j \text{ is a moving boundary node.} \end{cases} \quad (\text{A.3})$$

This procedure is continued until convergence to an acceptable residual error is obtained.

Evaluation of $\partial \mathbf{R}_i^k / \partial \mathbf{L}_j^k$ at a fixed node consists of the evaluation of the derivatives with respect to the flow variables at this node. This is commonly addressed in existing models and will not be discussed here. However, at a moving node, the Jacobian $\partial \mathbf{R}_i^k / \partial \mathbf{L}_j^k$ involves the derivatives $\partial \mathbf{R}_i^k / \partial s_j^k$, $\partial \mathbf{R}_i^k / \partial p_j^k$, and

$\partial \mathbf{R}_i^k / \partial \mathbf{q}_j^k$. An important aspect of the model developed here is the determination of the Jacobian terms $\partial \mathbf{R}_i^k / \partial \mathbf{s}_j^k$ for the finite elements. The following is a description of these derivatives.

Element variables are mapped from the global coordinate system to local coordinates (figure 4.2) using the transformation

$$\begin{Bmatrix} d\xi \\ d\eta \end{Bmatrix} = \begin{bmatrix} \frac{\partial \xi}{\partial x} & \frac{\partial \xi}{\partial y} \\ \frac{\partial \eta}{\partial x} & \frac{\partial \eta}{\partial y} \end{bmatrix} \begin{Bmatrix} dx \\ dy \end{Bmatrix} \quad (\text{A.4})$$

or

$$\begin{Bmatrix} d\xi \\ d\eta \end{Bmatrix} = \frac{1}{J} \begin{bmatrix} \frac{\partial y}{\partial \eta} & -\frac{\partial x}{\partial \eta} \\ -\frac{\partial y}{\partial \xi} & \frac{\partial x}{\partial \xi} \end{bmatrix} \begin{Bmatrix} dx \\ dy \end{Bmatrix} \quad (\text{A.5})$$

where J is the Jacobian of transformation. Since,

$$J = \frac{\partial x}{\partial \xi} \frac{\partial y}{\partial \eta} - \frac{\partial x}{\partial \eta} \frac{\partial y}{\partial \xi} \quad (\text{A.6})$$

then

$$\begin{bmatrix} \frac{\partial \xi}{\partial x} & \frac{\partial \xi}{\partial y} \\ \frac{\partial \eta}{\partial x} & \frac{\partial \eta}{\partial y} \end{bmatrix} = \frac{1}{J} \begin{bmatrix} \frac{\partial y}{\partial \eta} & -\frac{\partial x}{\partial \eta} \\ -\frac{\partial y}{\partial \xi} & \frac{\partial x}{\partial \xi} \end{bmatrix}. \quad (\text{A.7})$$

Using the basis function ϕ_i , the derivatives for the fixed grid case are interpolated as

$$\begin{aligned}
\frac{\partial \xi}{\partial x} &= \frac{1}{J} \frac{\partial y}{\partial \eta} = \frac{1}{J} \sum_{i=1}^N \frac{\partial \phi_i}{\partial \eta} y_i \\
\frac{\partial \xi}{\partial y} &= -\frac{1}{J} \frac{\partial x}{\partial \eta} = -\frac{1}{J} \sum_{i=1}^N \frac{\partial \phi_i}{\partial \eta} x_i \\
\frac{\partial \eta}{\partial x} &= -\frac{1}{J} \frac{\partial y}{\partial \xi} = -\frac{1}{J} \sum_{i=1}^N \frac{\partial \phi_i}{\partial \xi} y_i \\
\frac{\partial \eta}{\partial y} &= \frac{1}{J} \frac{\partial x}{\partial \xi} = \frac{1}{J} \sum_{i=1}^N \frac{\partial \phi_i}{\partial \xi} x_i
\end{aligned} \tag{A.8}$$

where N is the number of nodes on the element.

The displacement of node j is given as $s_j = (\theta_{x_j}, \theta_{y_j})|s_j|$. Then the global coordinates are updated every iteration as

$$\begin{aligned}
x_j^{k+1} &= x_j^k + \theta_{x_j} s_j \\
y_j^{k+1} &= y_j^k + \theta_{y_j} s_j
\end{aligned} \tag{A.9}$$

The fixed grid derivatives are modified to account for nodal displacement.

$$\begin{aligned}
\frac{\partial x}{\partial \xi} &= \sum_{i=1}^N \left(\frac{\partial \phi_i}{\partial \xi} x_i \right) + \frac{\partial \phi_j}{\partial \xi} \theta_{x_j} s_j \\
\frac{\partial y}{\partial \eta} &= \sum_{i=1}^N \left(\frac{\partial \phi_i}{\partial \eta} y_i \right) + \frac{\partial \phi_j}{\partial \eta} \theta_{y_j} s_j \\
\frac{\partial x}{\partial \eta} &= \sum_{i=1}^N \left(\frac{\partial \phi_i}{\partial \eta} x_i \right) + \frac{\partial \phi_j}{\partial \eta} \theta_{x_j} s_j \\
\frac{\partial y}{\partial \xi} &= \sum_{i=1}^N \left(\frac{\partial \phi_i}{\partial \xi} y_i \right) + \frac{\partial \phi_j}{\partial \xi} \theta_{y_j} s_j
\end{aligned} \tag{A.10}$$

The derivatives of the Jacobian of transformation with respect to the displacement of node j is

$$\begin{aligned}
\frac{\partial J}{\partial s_j} &= \frac{\partial x}{\partial \xi} \frac{\partial}{\partial s_j} \left(\frac{\partial y}{\partial \eta} \right) + \frac{\partial}{\partial s_j} \left(\frac{\partial x}{\partial \xi} \right) \frac{\partial y}{\partial \eta} - \frac{\partial x}{\partial \eta} \frac{\partial}{\partial s_j} \left(\frac{\partial y}{\partial \xi} \right) - \frac{\partial}{\partial s_j} \left(\frac{\partial x}{\partial \eta} \right) \frac{\partial y}{\partial \xi} \\
&= \frac{\partial x}{\partial \xi} \left(\frac{\partial \phi_j}{\partial \eta} \theta_{y_j} \right) + \frac{\partial y}{\partial \eta} \left(\frac{\partial \phi_j}{\partial \xi} \theta_{x_j} \right) - \frac{\partial x}{\partial \eta} \left(\frac{\partial \phi_j}{\partial \xi} \theta_{y_j} \right) - \frac{\partial y}{\partial \xi} \left(\frac{\partial \phi_j}{\partial \eta} \theta_{x_j} \right).
\end{aligned} \tag{A.11}$$

Gradients of the basis function, ϕ , are given as

$$\frac{\partial \phi}{\partial x} = \sum_{i=1}^N \left(\frac{\partial \phi_i}{\partial \xi} \frac{\partial \xi}{\partial x} + \frac{\partial \phi_i}{\partial \eta} \frac{\partial \eta}{\partial x} \right) = \frac{1}{J} \sum_{i=1}^N \left(\frac{\partial \phi_i}{\partial \xi} \frac{\partial y}{\partial \eta} - \frac{\partial \phi_i}{\partial \eta} \frac{\partial y}{\partial \xi} \right) \tag{A.12}$$

and

$$\frac{\partial \phi}{\partial y} = \sum_{i=1}^N \left(\frac{\partial \phi_i}{\partial \xi} \frac{\partial \xi}{\partial y} + \frac{\partial \phi_i}{\partial \eta} \frac{\partial \eta}{\partial y} \right) = \frac{1}{J} \sum_{i=1}^N \left(\frac{\partial \phi_i}{\partial \xi} \frac{\partial x}{\partial \eta} - \frac{\partial \phi_i}{\partial \eta} \frac{\partial x}{\partial \xi} \right). \tag{A.13}$$

Then since the partial derivative of the element basis with respect to global coordinates is not a function of the displacement of a global coordinate, i.e.

$$\frac{\partial}{\partial s_j} \left(\frac{\partial \phi_i}{\partial \xi} \right) = \frac{\partial}{\partial s_j} \left(\frac{\partial \phi_i}{\partial \eta} \right) = 0, \tag{A.14}$$

then derivatives with respect to nodal displacement are

$$\begin{aligned} \frac{\partial}{\partial s_j} \left(\frac{\partial \phi}{\partial x} \right) = & \frac{1}{J} \left[\sum_{i=1}^N \left(\frac{\partial \phi_i}{\partial \xi} \right) \frac{\partial}{\partial s_j} \left(\frac{\partial y}{\partial \eta} \right) - \sum_{i=1}^N \left(\frac{\partial \phi_i}{\partial \eta} \right) \frac{\partial}{\partial s_j} \left(\frac{\partial y}{\partial \xi} \right) \right] \\ & - \frac{1}{J^2} \frac{\partial J}{\partial s_j} \left[\sum_{i=1}^N \left(\frac{\partial \phi_i}{\partial \xi} \right) \frac{\partial y}{\partial \eta} - \sum_{i=1}^N \left(\frac{\partial \phi_i}{\partial \eta} \right) \frac{\partial y}{\partial \xi} \right] \end{aligned} \quad (A.15)$$

and

$$\begin{aligned} \frac{\partial}{\partial s_j} \left(\frac{\partial \phi}{\partial y} \right) = & \frac{1}{J} \left[- \sum_{i=1}^N \left(\frac{\partial \phi_i}{\partial \xi} \right) \frac{\partial}{\partial s_j} \left(\frac{\partial x}{\partial \eta} \right) + \sum_{i=1}^N \left(\frac{\partial \phi_i}{\partial \eta} \right) \frac{\partial}{\partial s_j} \left(\frac{\partial x}{\partial \xi} \right) \right] \\ & - \frac{1}{J^2} \frac{\partial J}{\partial s_j} \left[- \sum_{i=1}^N \left(\frac{\partial \phi_i}{\partial \xi} \right) \frac{\partial x}{\partial \eta} + \sum_{i=1}^N \left(\frac{\partial \phi_i}{\partial \eta} \right) \frac{\partial x}{\partial \xi} \right]. \end{aligned} \quad (A.16)$$

The line integrals along the boundary are transformed from global coordinates to local coordinates using the one-dimensional Jacobian of transformation, J ,

$$J = \frac{1}{2} \sqrt{(x_2 - x_1)^2 + (y_2 - y_1)^2} \quad (A.17)$$

where x_1 and y_1 are the global coordinates of one node and x_2 and y_2 are the global coordinates for the other node. If node 1 needs to be moved, the new coordinate is

$$\begin{aligned} x_1' &= x_1 + s_1 \theta_{x_1} \\ y_1' &= y_1 + s_1 \theta_{y_1} \end{aligned} \quad (A.18)$$

and the Jacobian is

$$\begin{aligned}
 J &= \frac{1}{2} \sqrt{(x_2 - x_1')^2 + (y_2 - y_1')^2} \\
 &= \frac{1}{2} \sqrt{(\Delta x_1')^2 + (\Delta y_1')^2}
 \end{aligned} \tag{A.19}$$

where $\Delta x_1' = x_2 - x_1 - s_1 \theta_{x_1}$ and $\Delta y_1' = y_2 - y_1 - s_1 \theta_{y_1}$. Then,

$$\frac{\partial J}{\partial s_1} = \frac{1}{2} \left[\Delta x_1' \frac{\partial(\Delta x_1')}{\partial s_1} + \Delta y_1' \frac{\partial(\Delta y_1')}{\partial s_1} \right] \left[(\Delta x_1')^2 + (\Delta y_1')^2 \right]^{-1/2} \tag{A.20}$$

where

$$\frac{\partial(\Delta x_1')}{\partial s_1} = -\theta_{x_1} \tag{A.21}$$

and

$$\frac{\partial(\Delta y_1')}{\partial s_1} = -\theta_{y_1} . \tag{A.22}$$

Similarly, if node 2 is moved,

$$\begin{aligned}
 x_2' &= x_2 + s_2 \theta_{x_2} \\
 y_2' &= y_2 + s_2 \theta_{y_2}
 \end{aligned} \tag{A.23}$$

and

$$\Delta x_2' = x_2 + s_2 \theta_{x_2} - x_1 \tag{A.24}$$

and

$$\Delta y_2' = y_2 + s_2 \theta_{y_2} - y_1 . \quad (\text{A.25})$$

Then,

$$\frac{\partial J}{\partial s_2} = \frac{1}{2} \left[\Delta x_2' \frac{\partial(\Delta x_2')}{\partial s_2} + \Delta y_2' \frac{\partial(\Delta y_2')}{\partial s_2} \right] \left[(\Delta x_2')^2 + (\Delta y_2')^2 \right]^{-1/2} \quad (\text{A.26})$$

where

$$\frac{\partial(\Delta x_2')}{\partial s_2} = \theta_{x_2} \quad (\text{A.27})$$

and

$$\frac{\partial(\Delta y_2')}{\partial s_2} = \theta_{y_2} . \quad (\text{A.28})$$

The grid velocity, (u_g, v_g) , is approximated as

$$u_{g_j}^{m+1} \approx \frac{\alpha}{\Delta \tau} \left[(x_j + \theta_{x_j} s_j)^{m+1} - x_j^m \right] + \frac{(1-\alpha)}{\Delta \tau} \left[x_j^m - x_j^{m-1} \right] \quad (\text{A.29})$$

and

$$v_{g_j}^{m+1} \approx \frac{\alpha}{\Delta \tau} \left[(y_j + \theta_{y_j} s_j)^{m+1} - y_j^m \right] + \frac{(1-\alpha)}{\Delta \tau} \left[y_j^m - y_j^{m-1} \right] \quad (\text{A.30})$$

where the superscripts $m-1$, m , and $m+1$ indicate the particular time step. Then,

$$\frac{\partial u_{\xi_j}^{m+1}}{\partial s_j} = \frac{\alpha}{\Delta \tau} \theta_{x_j} \quad (\text{A.31})$$

and

$$\frac{\partial v_{\xi_j}^{m+1}}{\partial s_j} = \frac{\alpha}{\Delta \tau} \theta_{y_j} . \quad (\text{A.32})$$

The spatial gradients of the variables are given as:

$$\begin{aligned} \frac{\partial Q}{\partial x} &= \sum_{i=1}^N \left[\left(\frac{\partial \phi_i}{\partial \xi} \frac{\partial \xi}{\partial x} + \frac{\partial \phi_i}{\partial \eta} \frac{\partial \eta}{\partial x} \right) Q_i \right] \\ &= \frac{1}{J} \sum_{i=1}^N \left[\left(\frac{\partial \phi_i}{\partial \xi} Q_i \right) \frac{\partial y}{\partial \eta} - \left(\frac{\partial \phi_i}{\partial \eta} Q_i \right) \frac{\partial y}{\partial \xi} \right] \end{aligned} \quad (\text{A.33})$$

and

$$\begin{aligned} \frac{\partial Q}{\partial y} &= \sum_{i=1}^N \left[\left(\frac{\partial \phi_i}{\partial \xi} \frac{\partial \xi}{\partial y} + \frac{\partial \phi_i}{\partial \eta} \frac{\partial \eta}{\partial y} \right) Q_i \right] \\ &= \frac{1}{J} \sum_{i=1}^N \left[\left(\frac{\partial \phi_i}{\partial \xi} Q_i \right) \frac{\partial x}{\partial \eta} - \left(\frac{\partial \phi_i}{\partial \eta} Q_i \right) \frac{\partial x}{\partial \xi} \right] . \end{aligned} \quad (\text{A.34})$$

As noted before, the terms involving local coordinates are not a function of nodal

displacement, then the derivatives of the spatial gradients with respect to node movement are

$$\begin{aligned} \frac{\partial}{\partial s_j} \left(\frac{\partial Q}{\partial x} \right) &= \frac{1}{J} \left[\frac{\partial \phi_i}{\partial \xi} Q_i \frac{\partial}{\partial s_j} \left(\frac{\partial y}{\partial \eta} \right) - \frac{\partial \phi_i}{\partial \eta} Q_i \frac{\partial}{\partial s_j} \left(\frac{\partial y}{\partial \xi} \right) \right] \\ &\quad - \frac{1}{J^2} \frac{\partial J}{\partial s_j} \left[\frac{\partial \phi_i}{\partial \xi} Q_i \frac{\partial y}{\partial \eta} - \frac{\partial \phi_i}{\partial \eta} Q_i \frac{\partial x}{\partial \xi} \right] \end{aligned} \quad (A.35)$$

and

$$\begin{aligned} \frac{\partial}{\partial s_j} \left(\frac{\partial Q}{\partial y} \right) &= \frac{1}{J} \left[\frac{\partial \phi_i}{\partial \xi} Q_i \frac{\partial}{\partial s_j} \left(\frac{\partial x}{\partial \eta} \right) - \frac{\partial \phi_i}{\partial \eta} Q_i \frac{\partial}{\partial s_j} \left(\frac{\partial x}{\partial \xi} \right) \right] \\ &\quad - \frac{1}{J^2} \frac{\partial J}{\partial s_j} \left[\frac{\partial \phi_i}{\partial \xi} Q_i \frac{\partial x}{\partial \eta} - \frac{\partial \phi_i}{\partial \eta} Q_i \frac{\partial x}{\partial \xi} \right]. \end{aligned} \quad (A.36)$$

The gradient of the grid velocity is interpolated as

$$\frac{\partial u_g}{\partial x} = \sum_{i=1}^N \frac{\partial \phi_i}{\partial x} u_{g_i} \quad (A.37)$$

and

$$\frac{\partial v_g}{\partial y} = \sum_{i=1}^N \frac{\partial \phi_i}{\partial y} v_{g_i} . \quad (\text{A.38})$$

Then the derivative with respect to nodal displacement is

$$\begin{aligned} \frac{\partial}{\partial s_j} \left(\frac{\partial u_g}{\partial x} \right) &= \frac{1}{J} \left[\sum_{i=1}^N \left(\frac{\partial \phi_i}{\partial \xi} u_{g_i} \right) \frac{\partial}{\partial s_j} \left(\frac{\partial y}{\partial \eta} \right) + \frac{\partial \phi_i}{\partial \xi} \frac{\partial u_{g_j}}{\partial s_j} \frac{\partial y}{\partial \eta} \right. \\ &\quad \left. + \sum_{i=1}^N \left(\frac{\partial \phi_i}{\partial \eta} u_{g_i} \right) \frac{\partial}{\partial s_j} \left(\frac{\partial y}{\partial \xi} \right) + \frac{\partial \phi_j}{\partial \eta} \frac{\partial u_{g_i}}{\partial s_j} \frac{\partial y}{\partial \xi} \right] \\ &\quad + \frac{1}{J^2} \frac{\partial J}{\partial s_j} \left[\sum_{i=1}^N \left(\frac{\partial \phi_i}{\partial \xi} u_{g_i} \right) \frac{\partial y}{\partial \eta} + \sum_{i=1}^N \left(\frac{\partial \phi_i}{\partial \eta} u_{g_i} \right) \frac{\partial y}{\partial \xi} \right] \end{aligned} \quad (\text{A.39})$$

and similarly

$$\begin{aligned} \frac{\partial}{\partial s_j} \left(\frac{\partial v_g}{\partial y} \right) &= \frac{1}{J} \left[\sum_{i=1}^N \left(\frac{\partial \phi_i}{\partial \xi} v_{g_i} \right) \frac{\partial}{\partial s_j} \left(\frac{\partial x}{\partial \eta} \right) + \frac{\partial \phi_i}{\partial \xi} \frac{\partial v_{g_j}}{\partial s_j} \frac{\partial x}{\partial \eta} \right. \\ &\quad \left. + \sum_{i=1}^N \left(\frac{\partial \phi_i}{\partial \eta} v_{g_i} \right) \frac{\partial}{\partial s_j} \left(\frac{\partial x}{\partial \xi} \right) + \frac{\partial \phi_j}{\partial \eta} \frac{\partial v_{g_i}}{\partial s_j} \frac{\partial x}{\partial \xi} \right] \\ &\quad + \frac{1}{J^2} \frac{\partial J}{\partial s_j} \left[\sum_{i=1}^N \left(\frac{\partial \phi_i}{\partial \xi} v_{g_i} \right) \frac{\partial x}{\partial \eta} + \sum_{i=1}^N \left(\frac{\partial \phi_i}{\partial \eta} v_{g_i} \right) \frac{\partial x}{\partial \xi} \right] . \end{aligned} \quad (\text{A.40})$$

The length scales used in the Petrov-Galerkin test function are

$$\Delta x = 2 \sqrt{\left(\frac{\partial x}{\partial \xi}\right)^2 + \left(\frac{\partial x}{\partial \eta}\right)^2} \quad (\text{A.41})$$

and

$$\Delta y = 2 \sqrt{\left(\frac{\partial y}{\partial \xi}\right)^2 + \left(\frac{\partial y}{\partial \eta}\right)^2} . \quad (\text{A.42})$$

Differentiating with respect to s_j

$$\frac{\partial(\Delta x)}{\partial s_j} = 2 \left[\frac{\partial x}{\partial \xi} \frac{\partial}{\partial s_j} \left(\frac{\partial x}{\partial \xi} \right) + \frac{\partial x}{\partial \eta} \frac{\partial}{\partial s_j} \left(\frac{\partial x}{\partial \eta} \right) \right] \left[\left(\frac{\partial x}{\partial \xi} \right)^2 + \left(\frac{\partial x}{\partial \eta} \right)^2 \right]^{-1/2} \quad (\text{A.43})$$

and

$$\frac{\partial(\Delta y)}{\partial s_j} = 2 \left[\frac{\partial y}{\partial \xi} \frac{\partial}{\partial s_j} \left(\frac{\partial y}{\partial \xi} \right) + \frac{\partial y}{\partial \eta} \frac{\partial}{\partial s_j} \left(\frac{\partial y}{\partial \eta} \right) \right] \left[\left(\frac{\partial y}{\partial \xi} \right)^2 + \left(\frac{\partial y}{\partial \eta} \right)^2 \right]^{-1/2} \quad (\text{A.44})$$

where

$$\frac{\partial}{\partial s_j} \left(\frac{\partial x}{\partial \xi} \right) = \frac{\partial \phi_j}{\partial \xi} \theta_{x_j} \quad (\text{A.45})$$

$$\frac{\partial}{\partial s_j} \left(\frac{\partial x}{\partial \eta} \right) = \frac{\partial \phi_j}{\partial \eta} \theta_{x_j} \quad (\text{A.46})$$

$$\frac{\partial}{\partial s_j} \left(\frac{\partial y}{\partial \xi} \right) = \frac{\partial \phi_j}{\partial \xi} \theta_{y_j} \quad (\text{A.47})$$

and

$$\frac{\partial}{\partial s_j} \left(\frac{\partial y}{\partial \eta} \right) = \frac{\partial \phi_j}{\partial \eta} \theta_{y_j} . \quad (\text{A.48})$$

REPORT DOCUMENTATION PAGE

Form Approved
OMB No. 0704-0188

Public reporting burden for this collection of information is estimated to average 1 hour per response, including the time for reviewing instructions, searching existing data sources, gathering and maintaining the data needed, and completing and reviewing the collection of information. Send comments regarding this burden estimate or any other aspect of this collection of information, including suggestions for reducing this burden, to Washington Headquarters Services, Directorate for Information Operations and Reports, 1215 Jefferson Davis Highway, Suite 1204, Arlington, VA 22202-4302, and to the Office of Management and Budget, Paperwork Reduction Project (0704-0188), Washington, DC 20503.

1.AGENCY USE ONLY (Leave blank)		2.REPORT DATE June 1996	3.REPORT TYPE AND DATES COVERED Final report
4.TITLE AND SUBTITLE A Two-Dimensional Free-Surface Flow Model for Trapezoidal High-Velocity Channels			5.FUNDING NUMBERS
6.AUTHOR(S) Richard L. Stockstill			
7.PERFORMING ORGANIZATION NAME(S) AND ADDRESS(ES) U.S. Army Engineer Waterways Experiment Station 3909 Halls Ferry Road Vicksburg, MS 39180-6199			8.PERFORMING ORGANIZATION REPORT NUMBER Technical Report HL-96-16
9.SPONSORING/MONITORING AGENCY NAME(S) AND ADDRESS(ES) U.S. Army Corps of Engineers Washington, DC 20314-1000			10.SPONSORING/MONITORING AGENCY REPORT NUMBER
11.SUPPLEMENTARY NOTES Available from the National Technical Information Service, 5285 Port Royal Road, Springfield, VA 22161.			
12a.DISTRIBUTION/AVAILABILITY STATEMENT Approved for public release; distribution is unlimited.			12b.DISTRIBUTION CODE
13.ABSTRACT (Maximum 200 words) A two-dimensional free-surface numerical flow model for trapezoidal high-velocity channels is developed. The model addresses common hydraulic features of high-velocity channels including subcritical or supercritical flow, which may undergo transition from one regime to the other and can be further complicated by the presence of oblique standing waves. The model is designed specifically for simulation of flow in trapezoidal high-velocity channels in which the depth is an unknown variable in the governing equations; therefore, the plan view of the flow domain as delineated by the water surface/bank interface is not known a priori. Steady state solutions are obtained by time-stepping from specified initial conditions using an implicit Petrov-Galerkin moving finite element representation of the governing equations. As the computed flow field evolves from the specified initial flow conditions and initial boundary location to the steady state, the moving finite element model adjusts the location of side boundaries with the depth solution. The algorithm includes a novel method for solving the boundary displacement and the flow variables simultaneously. Testing of the computational model consists of comparing model results with analytical solutions and laboratory flume data. These tests demonstrate that the numerical model can be used as a tool for the evaluation of trapezoidal high-velocity channel designs.			
14.SUBJECT TERMS Moving boundaries Moving finite element method Numerical model Petrov-Galerkin Shallow-water equations Subcritical flow Supercritical flow Trapezoidal high-velocity channels			15.NUMBER OF PAGES 198
			16.PRICE CODE
17.SECURITY CLASSIFICATION OF REPORT UNCLASSIFIED	18.SECURITY CLASSIFICATION OF THIS PAGE UNCLASSIFIED	19.SECURITY CLASSIFICATION OF ABSTRACT	20.LIMITATION OF ABSTRACT